MECHANICAL DESIGN AND FAILURE MODE ANALYSIS OF MULTI-STAGE MAGNETIC GEARS

by

Sina Modaresahmadi

A thesis submitted to the faculty of
The University of North Carolina at Charlotte
in partial fulfillment of the requirements
for the degree of Doctor of Philosophy in
Mechanical Engineering

Charlotte

2020

Approved by:

_____
Dr. Wesley Williams

_____
Dr. Alireza Tabarraei

_____
Dr. Joshua Tarbutton

_____
Dr. Yesim Sireli

ABSTRACT

SINA MODARESAHMADI. Mechanical Design and Failure Mode Analysis of Multi-Stage Magnetic Gears. (Under the direction of DR. WESLEY WILLIAMS)

Magnetic gearboxes are a developing technology that is being considered as an alternative to mechanical gearboxes for non-contact transmission of torque in numerous applications. While mechanical gearboxes are commonplace in mechanical designs due to centuries of use and refinement, they have inherent limitations or failure modes that necessitate a) significant safety factors in their specification and/or b) routine maintenance. With non-contact transmission of torque, magnetic gearboxes have inherent overload protection and do not suffer from the wear-based failure mechanisms of mechanical gears meshing. The design of magnetic gears is focused on high torque densities, high efficiencies, high gear ratios, and low torque ripple. The pursuit of these goals comes with inherent contradictions or challenges; for example, high torque densities can lead to large radial loads, causing unacceptable deflections. High gear ratios in turn mean higher speeds which will increase eddy current losses and lower the overall efficiency. Successful magnetic gearing designs are an iterative process that incorporates by magnetic and mechanical considerations.

Over the course of two multi-stage magnetic gearbox designs, this research specifically addressed three areas of the magnetic gear design process; structural, thermal, and manufacturing/assembly. To achieve magnetic performance, laminated steel structures are commonly employed in magnetic gear designs, but these laminated structures offer lower stiffness than the solid steel alternatives and are difficult to model due to the small thickness dimension. Techniques for reducing the computational load and accurately

modeling the bonding stiffness are presented and compared to experimental results. Thermal analysis of magnetic gearboxes has typically followed the lead of electrical machine researchers and used a simple conduction model for heat transfer through air. This approach is compared to a higher fidelity model that incorporates the effect of convection in heat transfer. Both models are compared to experimental results, with the traditional approach being sufficient for most closed systems, while the convection-conduction method is suggested for systems with inlet and outlet airflows. Finally, scaled up design, assembly and testing of magnetic gears has identified several aspects that have to be considered when moving from smaller, benchtop devices. First, long, uninterrupted laminated stacks were found to be unrealistic due to deflections over the length of the span. Second, the much larger forces between the magnets had to be accounted for in the assembly process with special fixturing and detailed assembly processes. Finally, at larger scale the edge effects of the magnetic analysis cannot be ignored. This axial flux means that material choices for mechanical elements axially proximate to the magnetically active region cannot be electrically conductive or there will be significant eddy current losses.

Applications of the lessons learned in this research will lead to magnetic gearbox designs that are higher performing and more economical. Such advances will make magnetic gearboxes increasingly viable as a component in energy systems and robotics, particularly in areas where access for preventative maintenance or repair are cost prohibitive.

ACKNOWLEDGEMENTS

Many thanks to all whose support helped me in my research and my progression through this Doctorate's degree. Firstly, I would like to express my deepest appreciation to my advisor Dr. Wesley Williams, who has the attitude and substance of a leader, a mentor, and a friend. He continually conveyed a spirit of adventure and motivation in regard to the research, and without his guidance and persistent help this dissertation would not have been possible. I owe the success of this thesis and my profession standing to his mentorship and unwavering support. I also owe a debt of gratitude to Dr. Jonathan Bird for his untiring support and guidance throughout this journey.

I would also like to thank the members of my committee, Dr. Alireza Tabarraei, Dr. Joshua Tarbutton, and Dr. Yesim Sireli for their support and membership on my thesis committee. I am very grateful to a number of my friends/coworkers who have been instrumental through my graduate degree, J. Khalesi, K. Li, C. Nichols, D. Barnett, and H. Baninajar. I also place on record, my sense of gratitude to my parents, Behnaz and Basir, and my lovely sisters for their continued support through my life and academic career.

Thank you to the Department of Energy and the UNC Coastal Study Institute for funding the magnetic gearing research and my graduate research assistantship. Thank you to the UNC Charlotte Department of Mechanical Engineering for their financial support. And thank you to SOLIDWORKS, ANSYS, and MATLAB for use of their software.

Finally, I dedicate this work to my loving wife, Golnaz. We stood by each other through thick and thin, shared many stories and spent entire lives together. This work as with all of my works belong to you my dear one.

TABLE OF CONTENTS

LIST OF TABLES

LIST OF FIGURES

CHAPTER 1: INTRODUCTION

Renewable energy systems like many mechanical systems often utilize mechanical gears to achieve a speed change in the generation of electricity. While mechanical gears are a well-established technology, there are some inherent limitations and failure modes that contribute to increases in the levelized cost of energy (LCOE). In remote or difficult installations (wind turbines, offshore wind turbines, and marine hydrokinetic devices) these failure modes can be a significant part of the LCOE, due to the operations and maintenance costs associate with maintaining or replacing the gearboxes.

Magnetic gears have emerged as a possible replacement technology in recent years that offers non-contact transmission of torque. The advantage of non-contact torque transmission via magnetic interaction does not come without new design challenges. Magnetic gearing designs are restricted in material selections and must be designed to maintain air gaps between the rotors, despite the strong forces of magnetic attraction between the rotors. These mechanical considerations as well as concerns of efficiency, fatigue, and heat transfer must be considered to arrive at a successful design.

Chapter 2 provides a literature review on the challenges with the mechanical gearboxes, specifically in the renewable energy harvesting applications. In this chapter, magnetic gears are introduced as an alternative for the traditional mechanical gearboxes, the chronological development of this technology is explained. Lastly, the mechanical challenges for scaling-up the magnetic gears are expanded.

Chapter 3 is dedicated to the methodology of the analysis conducted throughout this thesis, both analytical and numerical solutions. Finite element analysis is the main tool for

the simulations in this thesis; so, a mesh study is performed in three of the main aspects of the analysis, including the force analysis, the deflection analysis and the thermal analysis.

Chapter 4 details the mechanical design of two magnetic gearboxes for two different applications, one for the wind turbine and one for the marine hydrokinetic applications. All the simulations and calculations throughout this thesis are performed in support of design, manufacture, and testing of these two magnetic gears. In his chapter, electrical laminated steels are mentioned as the alternative for the solid steels that increases the magnetic performance of the magnetic gear. But the laminated inherent of these electrical steels are associated with lower stiffness. A test setup is devised to investigate the strength of the bonding agent between the laminations against magnetic forces that cause bending deflections.

Chapter 5 introduces the sub-scale versions of the wind and MHK magnetic gears for the thermal analysis. A test setup is assembled to validate the simulation results of the thermal analysis with the experimental data.

Chapter 6 is dedicated to the presentation of the calculations, simulations and the validation results of the comparison between the experimental data and the simulations. The chapter is divided into two sections, i. e. Wind and MHK. Each section starts with the force calculations and the deflection analysis, followed by the loss calculations and the thermal analysis. In the last part of each section, the final design of the magnetic gear for each application (wind and MHK) is presented.

Chapter 7 provides a summary of the contributions in this thesis and suggests the future works in this context.

CHAPTER 2: LITERATURE REVIEW

2.1 Gearbox History and Application

Very first steps of design and development of gearboxes roots back to the 19th century [1]. The function of gearbox is to transmit rotational motion from a driver unit to a driven one. There are several ways to transmit the torque and rotational velocity from the input shaft to output shaft, including rolling friction, wrapping transmission, etc. [2]. Although, not only the simple structure and the relative small size of the gears and gearboxes are an advantage over the other approaches, but other pros are also defined for this mechanism such as certainty of transmission, accurate angular speed ratio, long life-time, and minimal loss of power [2]. These units might operate in different speeds which requires a speed-increasing or speed-decreasing unit. Are responsible for adjusting the change in speed from the driver to the driven unit. The application of the gearboxes, although, is not limited to this, but they are also used to change the sense of rotation of bridge an angle between driving and driven machinery [3]. The applications of the gears are categorized into four basic fields: motion transmission mechanism, power transmission mechanism, grasping mechanism, and intermittent motion mechanism [2]. Many industries have used the gear drives in their mechanical systems, from small clocks and precision machines to large gears used in turbo-machinery, refinery, process, energy, construction, mining and marine. This wide range of applications demands for deep monitoring, mechanical analysis, behavior prediction, design optimization, and failure mode analysis of the gearbox and the sub-systems on the unit.

There are many types of the gearboxes, but the simplest one comprises two sets of gears located in a defined distance and engaged in the meshing teeth area. The rolling

friction is the way of contact between the two teeth elements to transmit the motion and power. One can say that the rotational motion is transmitted through the rolling contact, without slippage, ideally. Two types of teeth engagements are shown in the Figure 2-1.

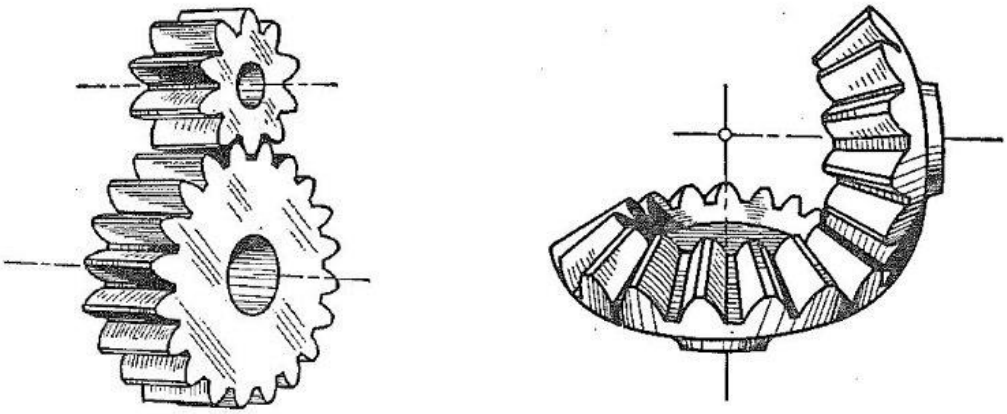

(a) (b)

Figure 2-1: Gears in contact (a) Spur gears, and (b) Bevel gears [2]

2.2 Mechanical Gearboxes

2.2.1 Design

There are many factors, limitations, conditions, and desired specifications that affect the design specification of a gearbox. Reported by P. Lynwander [3], the following are introduced as parameters that affect the gearbox configuration [3]:

- Physical arrangement of the machinery: The relative location of the driven and driven equipment in a mechanical system defines the geometrical relationship of the input and output shafts, including parallel offset, concentric, right angle, or skewed.

- Ratio required between input and output: No limitation for the gear ratio is defined, except the levelized complexity of the system.
- Torque loading: A critical criteria that governs the size of the gearbox and the geometry of the gear teeth is the torque load. Tooth load is defined as the proportion of the applied torque on the gear to the pitch radius. High-speed applications draw special attention to the component geometry discrepancies including spacing error and shifting unbalance, as well as the overheating which is proportional to the speed, lubrication and the bearing design.
- Efficiency: The efficiency is quoted at the design load and speed conditions. An estimation of the efficiency for industrial gearboxes reports the power loss of 1% to 2% per mesh.
- Space and weight limitations: There are applications for the gearboxes in industry in which a set of constructions and limitations are defined for the weight and the geometric specifications of the gearbox. Aerospace industry is an example where the light weight gearboxes are desired.
- Physical environment: When a gearbox is going to be designed, the operational environment must be defined. The environmental condition might have adverse effect on the gears, materials, lubrication, seals, bearings, etc. Of the environmental conditions, one can list the dust, humidity, chemicals, and temperature.

Depending on all these design factors, many types of gears are designed for a variety of applications, including spur gear, helical gear, gear rack, bevel gear, spiral bevel

gear, screw gear, miter gear, worm gear, internal gear, etc. Figure 2-2 shows these gears for graphical illustration of the difference. Note that the gears are also classified in several different ways, including classification based on the orientation of the axis, based on the positional relations of the attached shaft, and precision class [2].

Figure 2-2: Different types of mechanical gears, (a) Spur gear, (b) Helical gear, (c) Gear rack, (d) Bevel gear, (e) Spiral bevel gear, (f) Screw gear, (g) Miter gear, (h), Worm gear, and (i) Internal gear [2].

2.2.2 Failure Modes and Costs

Renewable energy projects are widely distributed across the U.S. in different forms of biogas fuel cell, biomass, geothermal, hydroelectric (<10 MW capacity), landfill gas, passive solar, solar photovoltaic, solar thermal, wind energy, etc. bringing investment to both urban and rural counties [4]. Wind energy and hydroelectric technology are in the center of focus in this research, not only for the utilization of the rotary systems which makes them a good candidate for mechanical assessment, but also because of their considerable generated equivalent energy compared to the other forms. Figure 2-3 shows the cumulative renewable energy generation between the years 2007 to 2018 in the state of North Carolina. The graph provides invaluable information about the relatively low investments on the hydroelectric and wind energy despite their considerable share of renewable energy generation.

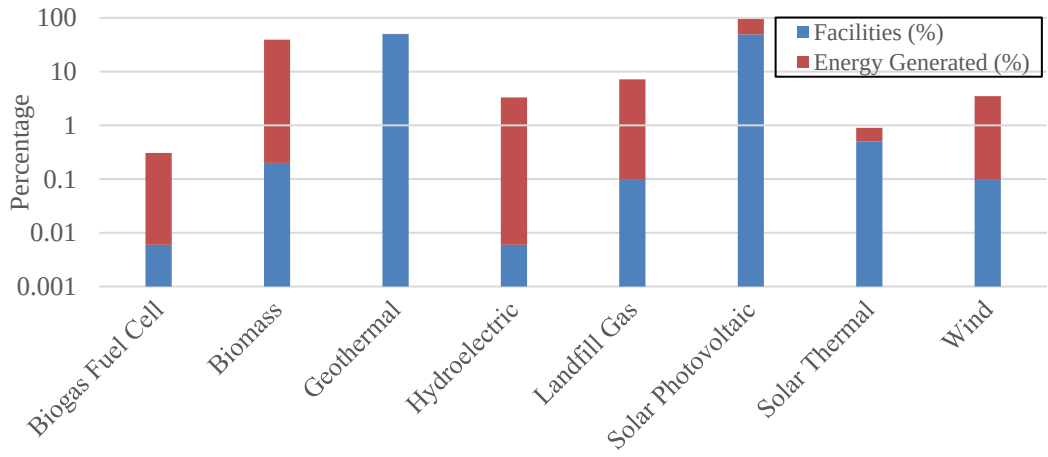

Figure 2-3: Cumulative renewable energy generation between the years 2007 to 2018 in the state of North Carolina [4].

Wind turbines as a growing technology of clean energy harvesting with an advanced technology for failure diagnosis of the sub-assembly features are appropriate

candidate to investigate gearbox applications and failures. Wind turbines are designed to IEC standards for a life of 20 years, although in practice, this life is much shorter [5]. Wind turbines generally operate under extremely harsh environmental conditions such as high temperature, dustiness, humidity, air pressure, and unpredictable loads due to “guest winds” [6]. Due to the severe operational conditions, all components of the wind turbine are prone to damage and failure, including the hub, drive shaft, gearbox, generator, yaw system, electric drive, etc. [7]. A study conducted by B. Hahn, M. Durstewitz and K. Rohrig [8], based on the total number of 34582 reports, compares the share of the main components of total number of failure in a wind turbine. Accordingly, gearbox, generator and drive train have the longest down-time per failure. Figure 2-4 show the annual failure frequency and the Downtime of each component in a wind turbine. A study on the failure rates of nearly 350 offshore wind turbines throughout Europe by J. Carroll, A. McDonald, and D. McMillan [9] shows that the highest rate of material cost for major replacement of the gearbox is the highest among all the sub-components of an offshore wind turbine, as in Figure 2-5. On the other hand, the number of required technicians for replacement of the different sub-components of the wind turbine shows that the gearbox needs the highest number of technicians after the turbine blades, which has much lower downtime and material cost compared to the gearbox, shown in Figure 2-6.

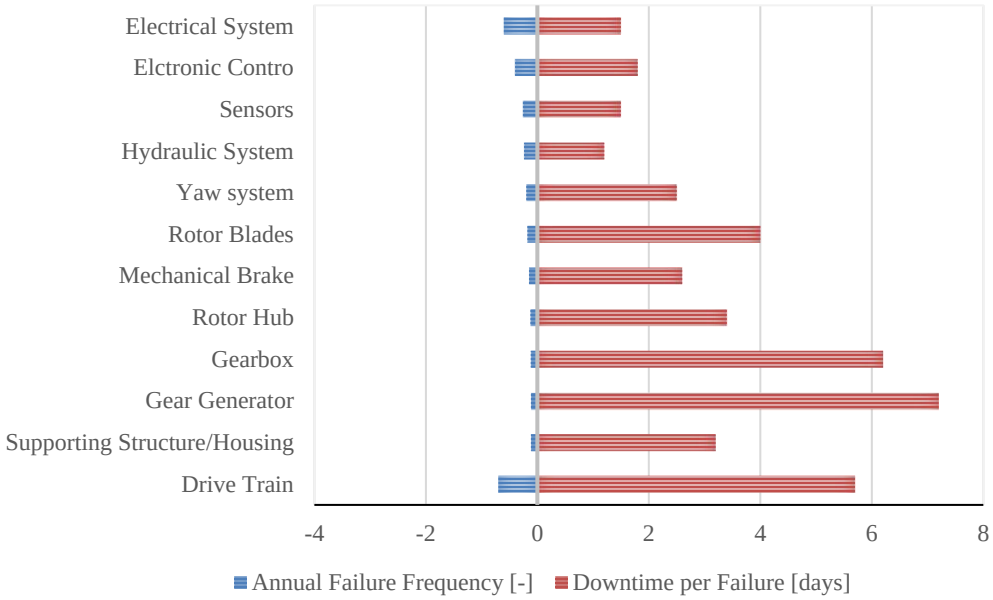

Figure 2-4: Failure Frequency and downtimes of components [8].

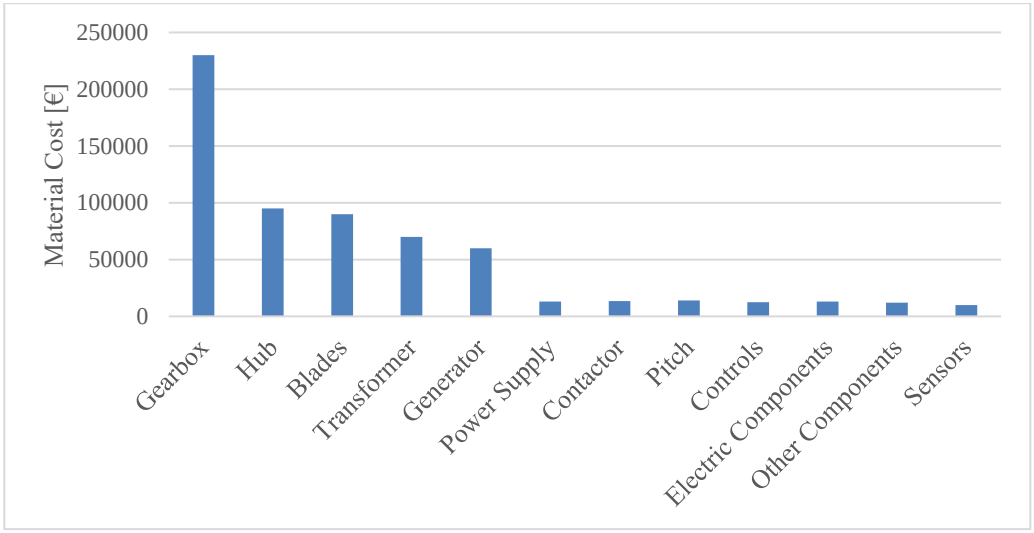

Figure 2-5: Average repair cost for each sub-component of an offshore wind turbine [9].

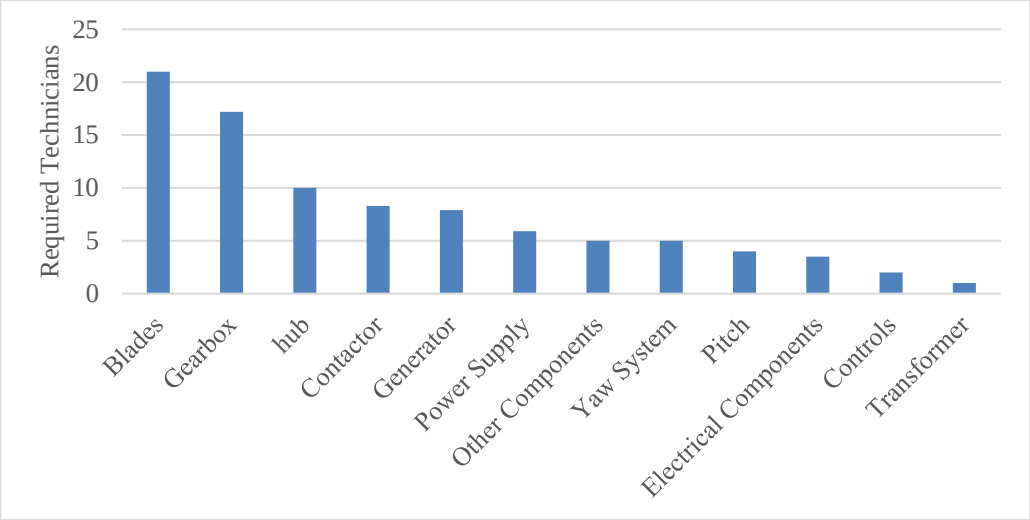

Figure 2-6: Average number of technicians required for repair for each sub-component of an offshore wind turbine [9].

The failure of the mechanical gearbox in a wind turbine application can lead to high costs of maintenance and replacement, as reported in [5]:

- The gearbox cost is about 13% of overall cost of a wind turbine, which makes it an expensive option to replace the gearbox.
- The process of removal and reinstallation of the gearbox has a high cost.

repair procedure is very complex.

- Revenue losses due to the long downtime between failure and repair completion/ reinstallation is very high.

By monitoring the sources of gearbox failure, it turns out that the contact inherent of the mechanical gearboxes for torque transmission are the main source of the failures [6], especially in contact regions which associate with tooth failures. Common failure modes of the mechanical gearboxes can be listed as follows (and in Figure 2-7):

- Pitting and spalling,
- Torque overload and tooth breakage,
- Cyclical loads, structural deflection, vibrations and fatigue problems,
- Tooth wear,
- Lubrication,
- Overheating, thermal effects and spot-weld.

In a closer look into the gear tooth, six (6) failure modes are listed for them as in TABLE 2-1, reported by [10] and [11].

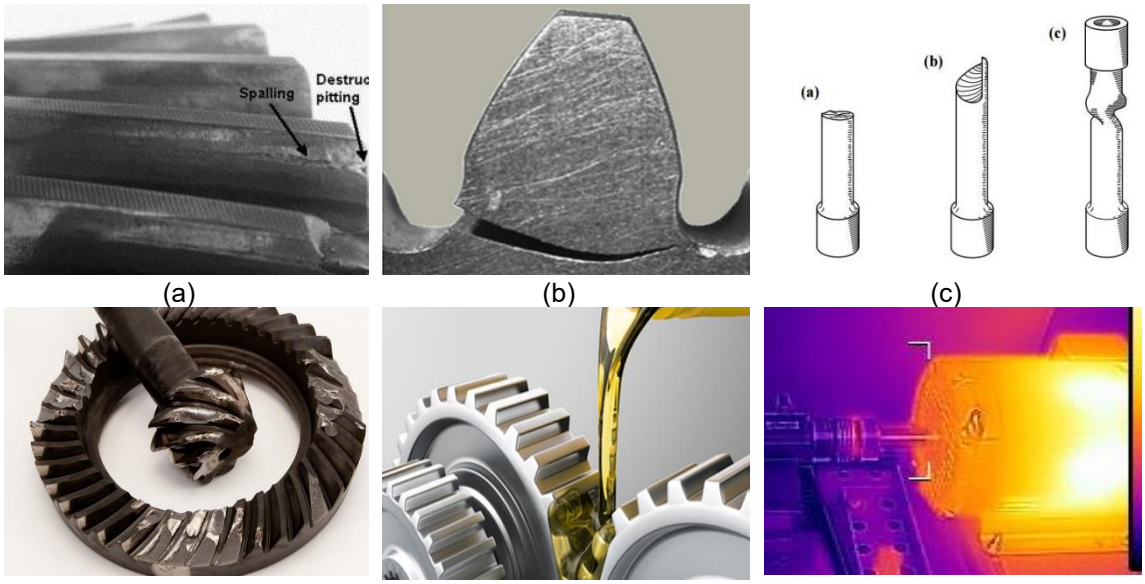

Figure 2-7: Mechanical gearbox failure modes (a) spalling [12], (b) tooth breakage[13], (c) torque overload, (d) tooth wear [14], (e) lubrication [15], (f) overheating.

TABLE 2-1: Gear tooth failure nomenclature [11]

Class	Mode
Bending fatigue	Low-cycle fatigue High-cycle fatigue Tooth end cracks Profile cracks
Contact fatigue	Macro-pitting Micro-pitting Sub-scale fatigue Spalling

Wear	Adhesion Abrasion Corrosion Cavitation Erosion
Scuffing	Scuffing
Overload	Brittle fracture Ductile fracture Mixed-mode fracture Plastic deformation
Cracking	Hardening cracks Grinding cracks Rim and web cracks Case-core separation

These failure modes can lead to costly repairs and downtime or increased operations and maintenance (O&M) costs, which increase the levelized cost of energy (LCOE) for wind and ocean energy applications. Currently, the majority of high-power wind turbines utilize a three-stage gearbox, comprised of a mechanical gearbox coupled to an induction generator or a permanent magnet (PM) generator, as it is low cost. Unfortunately, wind turbine gearboxes have been one of the main causes of wind turbine downtime and the gearbox failure rates increase with power level. This has resulted in the wind-turbine gearboxes not being able to achieve their desired 20-year design life [16]. Therefore, relying on the use of a mechanical gearbox causes significant long-term reliability problems [17] thereby greatly increasing the levelized cost of energy (LCOE). LCOE is a great concern especially in remote-access applications for which a great reliability is required including offshore turbines, marine hydrokinetic application and wind turbines. The main alternative to the use of a gearbox is to use a direct-drive permanent magnet (DD-MP) generator [18]. The use of the DD-PM generator removes the reliability concerns with regard to the mechanical gearbox. However, the torque density of a DD-PM generator is thermally limited (by current) and therefore a PM generator does

not normally achieve torque densities greater than 50Nm/L [19]. For this reason, DD-PM generators become very large when scaled-up in size. This large size makes them difficult to integrate within the Marine Hydro-Kinetic (MHK) structure and it limits the DD-PMs scalability. It also makes the initial cost of the DD-PM uncompetitive when compared with a mechanically geared generator. In order to increase renewable energy use and reduce the LCOE there appears to be a real need for an alternative approach.

2.3 Magnetic Gearboxes

2.3.1 History

Magnetic Gears are an emerging technology for non- contact transmission of torque that replace the meshing teeth of traditional gearboxes with magnetic field. Given the mitigation of numerous contact- based failure modes, magnetic gearboxes are envisioned as an enabling technology for Wind Turbines and Ocean Current Turbines (OCT). Figure 2-8 shows a schematic view of mechanical gearbox vs magnetic gearbox, in which inner and outer rotors are substituted with arrays of permanent magnets of specific orientation, and the middle gearing set is substituted with a modulating conductive element.

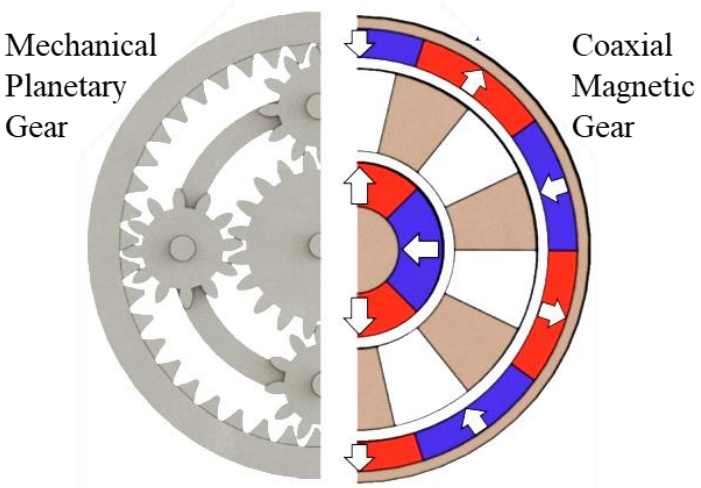

Figure 2-8: Coaxial magnetic gearbox and its analogy to a mechanical planetary gear stage [20].

Reducing the prevalence of failures reduces the need for repairs or preventative maintenance, both of which are significant undertakings for novel, hard to access technologies, including wind and ocean. These failure modes can lead to costly repairs and downtime or increased operations and maintenance (O&M) costs, which increase the LCOE for wind and ocean energy applications. Failure modes associated with teeth contact are addressed in magnetic gears due to the contactless torque transmission, including spalling, overload, tooth wear and lubrication, but cyclical loads and structural deflection, and thermal stresses due to eddy current losses are still of great concern. Design of magnetic gearboxes involves a combination of both magnetics and mechanical analysis.

Magnetic gears are poised to rapidly move up the Technology Readiness Level (TRL) scale, based on the record of accomplishment of successful benchtop and pilot scale testing. With the magnetics well understood and the manufacturing processes becoming more refined with each iteration. Currently, improving the predictability, reliability, and economy of designs, as well as scalability of the system are the main goals. As those metrics continue to improve, numerous markets could benefit from reliable non-contact transmission of torque that is free of the classic failure modes that have plagued traditional gearboxes.

The very first idea of the magnetic gear introduced by C. G. Armstrong [21] in 1901, who designed a power transmitting device with external spur gear configuration. In this design, the teeth were wound by coils and were magnetized when the coils were energized (driver wheel). Using permanent magnets in the design of an MG can be tracked down to a U. S. Patent Application filed in 1913 and patented in 1916 [22] in which two

rotating shafts with steel poles are separated by an array of stationary magnetic poles. In this design, radial positioning of the three parts is utilized. In 1920, Hugh M. Stolier [23] introduced the concept of magnetics in the design of worm gear. In 1941, H. T. Faus [24] patented several magnetic gearing arrangements with various axis orientations. This inventor introduced and patented a magnetic transmission using spiral magnetic gearing and the potential applications, 4 years later [25]. In 1968, Thomas B. Martin, Jr. [26] proposed a magnetic transmission system with coaxial radial configuration of the magnets. Hans P. Schlaeppi [27] proposed the axial arrangement of magnetic gears in 1968. In 1980, D. E. Hesmondhalgh, et. al. [28] a multi-element magnetic gear by arranging three 4-pole radial magnetic gears, axially in series. The series connection of the magnetic gears is a novel concept proposed in this paper, but the positioning of the magnetic poles between two modulating pieces doesn't seem to be an efficient configuration.

Later, in 1987, a double array pinion and gear with axial air gap is proposed as the first magnetic pinion-gear design, with no steel pieces as modulating parts [29]. In this paper, magnetic gears are located with a 3mm distance relative to each other. K. Ikuta, S. Makita and S. Arimoto [30] are of the first few researchers to compare radially positioned magnetic gears with two sets of permanent magnets. Torque density is investigated on this design for gap sizes of 1mm to 5mm. In this paper, robustness against large input-torque fluctuations as well as miss-arrangement of the gears is counted as a unique feature due to magnetic transmission. S. Kikuchi and K. Tsurumoto later investigated different topologies of magnetic worm gears using permanent magnets [31], [32]. Cycloidal and lead screw/tubular linear magnetic gears are the designs that introduced and investigated much

later [33], [32]. Figure 2-9 shows the chronological development of the various magnetic gearing designs.

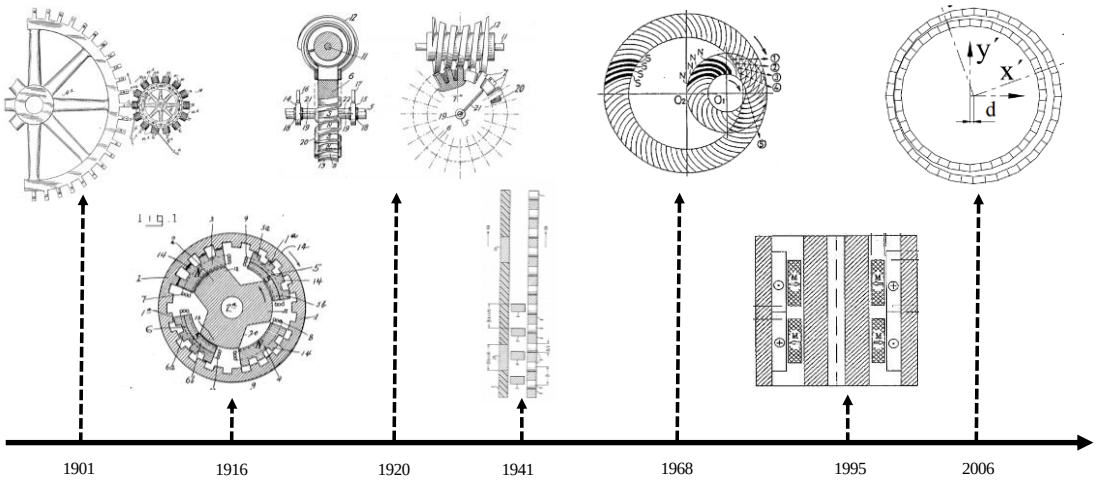

Figure 2-9: Chronological order of the invention of the magnetic gearing designs[21], [21]–[23], [26], [32], [34].

K. Atallah and D. Howe are of the leading researchers in magnetic gearing designs, implementing steel pole pieces in the presence of two arrays of permanent magnets [36]. As stated in this article, magnetic gears were previously recognized as an inappropriate option for electrical power generation application due to their inherent low power factor and high volt-ampere converter rate, as well as poor torque density. With this new topology of magnetic gears, significant improvement in torque density is achieved, which exceeded 100 kNm/m^3, reportedly, compared to a range of 40-80 KNm/m^3 for previous designs. Another design of magnetic gears is called linear magnetic gear design, proposed by K. Atallah, J. Wang and D. Howe [37] in which a set of steel rings are mounted between two cylindrical arrays of magnetic pole pairs, with a separating distance of 1mm. Another topology of the magnetic gearing is called Axial- Field, proposed by S. Mezani, K. Atallah and D. Howe [38], in which a set of ferromagnetic pole- pieces are fixed with a 2mm gap

between the two sets of permanent magnets. The magnetic spur gear was first proposed by S. Kikuchi and K. Tsurumoto [39], with two sets of magnetic pole pairs, called worm and worm wheel, although due to complexity of this design, it is not pursued as much.

2.3.2 Designs

Similar to the mechanical gears, magnetic gears are developed into a broad range of topologies and designs. According to literature review, magnetic gears are generally categorized into two main classes, namely (1) Conventional Non-Modulated MG's, and (2) Modulated MG's [40].

Class-one of MG's are influenced by the mechanical gearbox designs, and the designers' goal was to mimic the mechanical counterpart. These MG's only consist of two or more sets of permanent magnets (PM's) on different arrangements interacting magnetically. Examples of these MG's are shown in Figure 2-10, in which all of them are named after their mechanical counterpart, including spur gear, worm gear, perpendicular gear, magnetic screw, planetary MG, and cycloidal MG. [40]. One advantage of these types of MG's is the simple topology of them, but the very low torque density of these designs makes it an unattractive choice for industrial application. The reason is that in these configurations, only a small portion of the magnetic field created by the PM's sets was utilized for torque production at any operating instant [41]. However, great efforts have been put to increase the torque density of the class-one MG's which led to the theoretical relative achievements, especially in the planetary and cycloidal MG's, but the complexity of the mechanical construction and the assembly process considerably obstructed their commercialization opportunities [40].

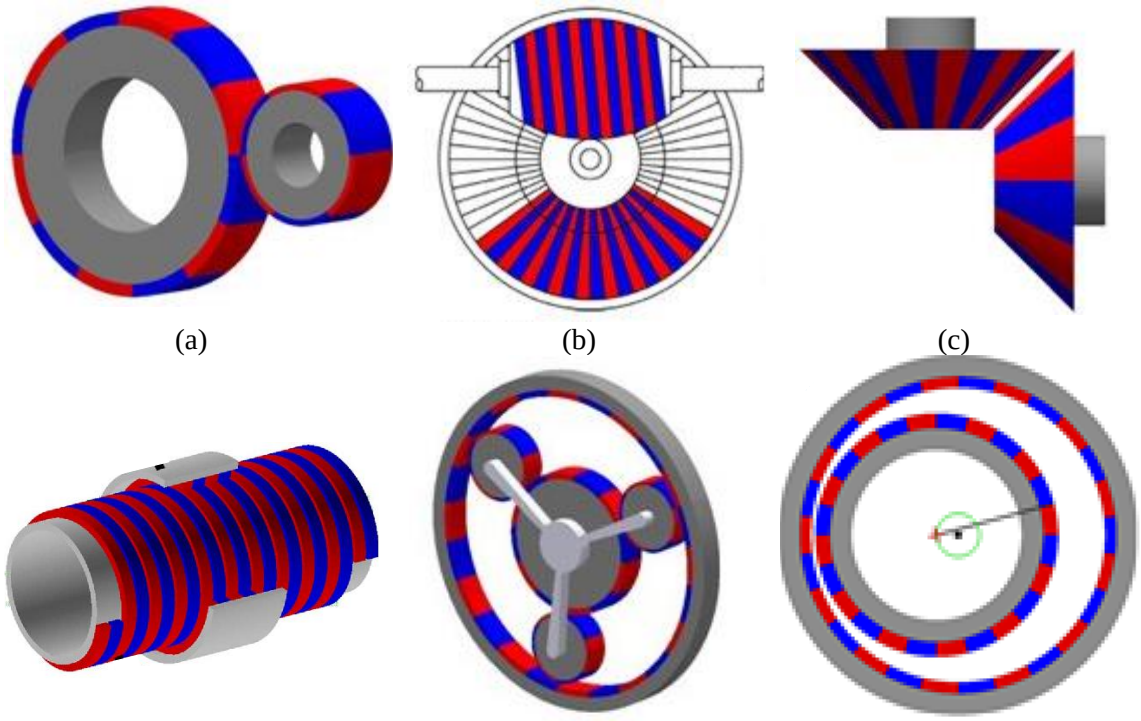

(a) (b) (c)

(d) (e) (f)

Figure 2-10: Schemes of different class-one MG's, (a) Spur MG [42], (b) Worm MG [39], (c) Perpendicular MG [42], (d) Magnetic Screw [43], (e) Planetary MG [42], and (f) Cycloidal MG [44].

Second class of the MG's belongs to the configurations in which modulating pieces are introduced into the design. Reported by [45], the class-one MG's create a short circuit of the magnetic flux. This problem which lead to the low performance of the system was solved by implementing an array of steel in the MG. This concept was later developed by employing modulating pieces in the design of a magnetic gear. Modulating pieces are in fact ferromagnetic pole-pieces located between two sets of PM arrangement/ rotor [46], [47], [48]. These MG's show much higher efficiency and torque density compared to the class-one MG's. Using the modulating pieces, the contribution of the PM's in the torque transmission maximizes at any instant, which led to higher torque density. Figure 2-11

shows main types of the class-two MG's, including coaxial radial MG, flux concentration Halbach MG, linear MG, Axial MG, L-type Axial MG, T-type axial MG, axial-Field Flux Modulated MG, intersecting axis MG, hybrid-flux MG, and transverse flux MG.

(a) (b) (c)

(d) (e) (f)

(g) (h) (i)

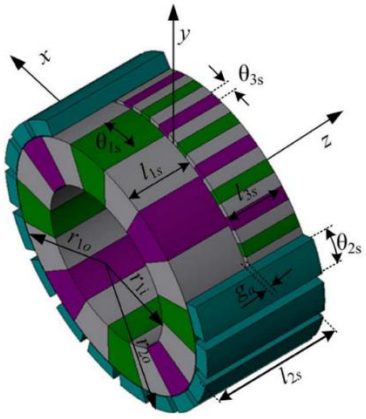

(j)

Figure 2-11: Schemes of different class-two MG's, (a) Coaxial radial MG [49], (b) Flux concentration Halbach MG [50], (c) Linear MG [51], (d) Axial MG [52], (e) L-type axial MG [53], (f) T-type axial MG [54], (g) Axial-field flux modulated MG [55], (h) Intersecting axis MG [56], (i) Hybrid-flux MG [57], (j) Transverse flux MG [58].

2.3.3 Design Goals

The design of magnetic gearboxes involves a combination of both magnetic and mechanical analysis. On the magnetic end of the design process, four main criteria are being sought.

- High Torque Density: Torque density is defined as a measure of torque-carrying capacity of a mechanical component to the unit of volume (torque/volume). This criterion is of great importance as it challenges the magnetic and mechanical design of the system at the same time. Mechanical gears have shown a promising rate of torque densities, but the magnetic gear technology is still struggling with this criterion, initially due to the very low performance of the magnets. Although, the development of the high-energy rare-earth magnets addressed this barrier considerably, finding the best design for collecting the highest rate of the potential energy of the PMs is

another issue that has been investigated highly in the past two decades [40]. A comparison of the torque density between different types of MG's and mechanical gears are provided in TABLE 1-2, showing the relatively high gap between the torque density capacity of MG's and mechanical gears despite the recent developments.

- High Gear Ratio: Gear ratio is defined as the ratio of the rotational velocity of the final gear to the first gear. Gear ratio is the criterion defined by the gearbox operational condition and the user. The vast application of the gearboxes demands a very large span of gear ratios. MG's show very low gear ratio capacities and the main reason is the complexity of the design for the higher hear ratio; although, multi-stage designs are introduced as an approach for increasing the gear ratio of the MG's. A comparison of the gear ratio for various types of MG's vs mechanical gears is presented in TABLE 2-2.

TABLE 2-2: Comparison of the gear ratio and torque density for various types of MG's vs mechanical gears [40], [59].

Gear type	Gear ratio	Torque density [kN.m/m3]
Mechanical Gearbox	1-28000	47-607
Planetary MG	3:1	97.3
Cycloidal MG	21:1	142
Harmonic MG	360:1	75
Magnetic Worm Gear	33:1	0.74
Magnetic Skew Gear	1.7:1	0.15
SPM MG	5.75:1	117
Optimized SPM MG	10.5:1	117
Spoke MG	5.5:1	92
IPM MG	5.5:1	64
Homopolar IPM MG	7.33:1	53
Halbach MG	4.25:1	124
Reluctance MG	8:1	29

Axial MG	5.75:1	70
L-shaped Axial MG	3.17:1	280
T-shaped Axial MG	3.17:1	74
Hybrid-Flux MG	5.5:1	181
Multi-stage MG	59:1	118

- High Efficiency: The efficiency of a magnetic gear is defined as the ratio of the output power to the input power, which directly relates to the input and output torque and rotational velocity. The selected materials, design, magnetic configuration, assembly, inherent limitations, operational conditions, etc. all affect the efficiency of the MG's. MG's have the capacity to achieve high performance rates [60]. Magnetic performance of MG's elevates in three fashions including (I) modifying the arrangement and topology of magnets and modulating parts, (II) minimizing the air gap between the rotors, and (III) material selection. Proposing new magnetic arrangements such as Halbach design [61], and changing the topology of the modulating pieces [62] are common efforts to enhance the performance. Regarding the study on air gap size, K. M. Bahrami, et al. [63] designed an axial magnetic gearbox with 0.5mm air gap and increased the gap to 0.8mm due to bending issues and assembly barriers. In an effort by D. Som, et al. [50], a 0.5mm air gap was achieved through optimized mechanical design. This was extended by K. Li, et al. [62] on a multi-stage magnetic gearbox in which a 0.5mm of air gap was targeted at the design stage, then increased to 1mm during the manufacturing process. Figure 2-12 shows a schematic representation of the air gap between rotors in a magnetic gear. For material selection for the components in active region, using laminations as the

modulating pieces in order to increase magnetic performance of the magnetic gears is a breakthrough. K. Atallah and D. Howe [36] are of the first researchers to propose utilization of laminations to improve performance of an MG. Substituting conductive supporting elements in active region with non-conductive materials is another effort to further improve a MG performance [18].

- Low Torque Ripple: Torque ripple is referred to the periodic increase/ decrease in the output torque as the mechanical system (MG in this case) operates. The different between the max and min values of the torque over one completion of revolution is the way to measure the torque ripple. The presence of different pole-pairs is the origin of the torque ripple. The difference in the air gap between the pole pieces and the PM's causes a torque ripple in an MG [64]. The torque ripple is the origin of the noise, vibration and in long term, fatigue in the system. This factor needs to be decrease in the magnetic design process of an MG through the adjustment of the combination of poles in the MG design, whether the magnetic pole-pairs or modulating pieces [65]. Torque ripple is also studied based on the air gap length and the thickness of the iron yoke in [66].

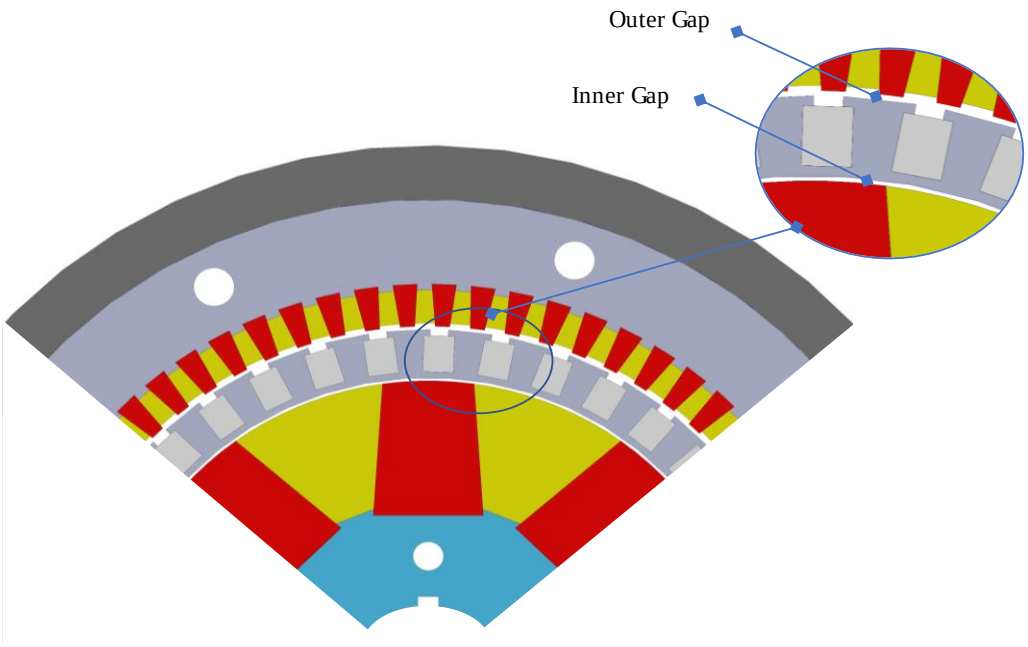

Figure 2-12: Schematic representation of the air gap between rotors in a magnetic gear.

The process of an MG design comprises several back and forth steps of mechanical and magnetic designs. It starts with a magnetic design, beginning with a desired gear ratio and input torque. This gear ratio governs the combination of magnetic pole-pairs, which are required on the inner and outer rotors, as well as the number of flux-focusing pieces for an intermediate 'cage' rotor. The required torque used to determine the size (axial length) of the magnets. The preliminary design is then simulated using finite element analysis software (FEA) to calculate the torque and efficiency. The mechanical team then analyzes the conceptual magnetic design. The researches perform structural analyses on the model using FEA given the predicted loads and material properties. In addition, the team refines the design to improve the manufacturability of the prototype. Eddy current loss analysis and edge effect calculations are the requirements for thermal analysis of the system.

Finally, the team manages the fabrication and assembly of the prototype. Figure 2-13 shows the flow chart for design, analysis and manufacturing of a magnetic gear.

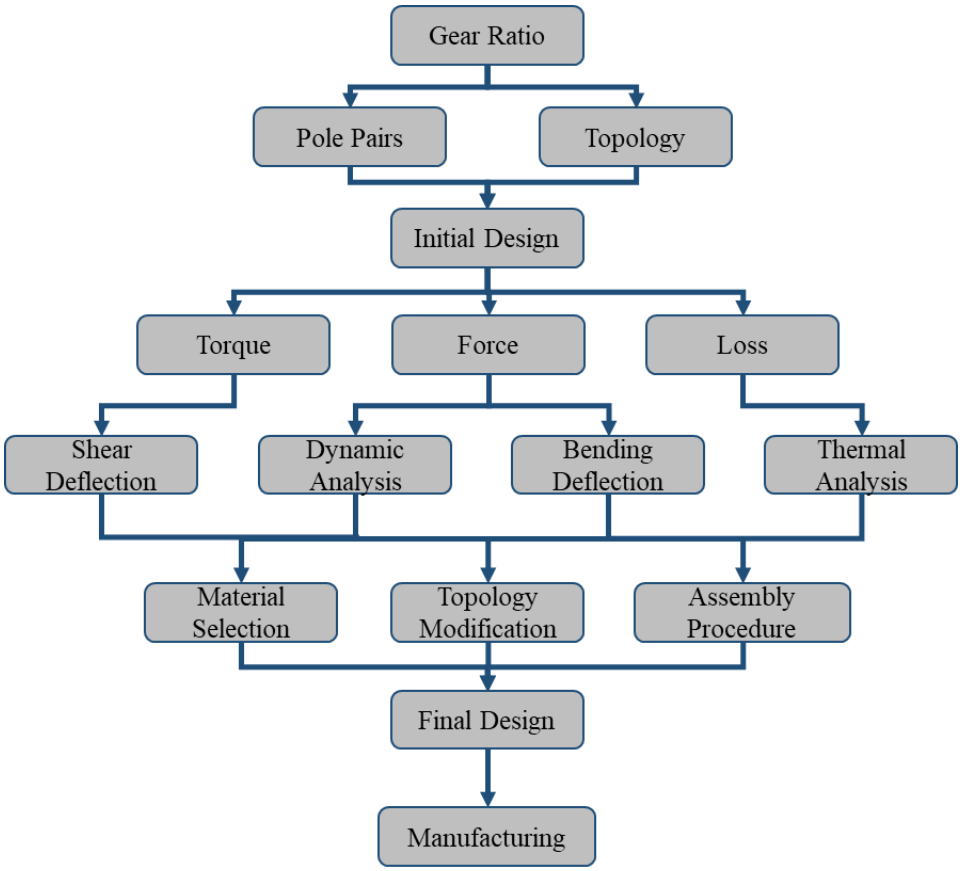

Figure 2-13: Flow chart for design, analysis and manufacturing of a magnetic gear [67].

2.3.4 Design Contradictions

In addition to the four indexes of torque density, gear ratio, efficiency and torque ripple that govern the design procedure of an MG, there are several factors of contradiction associated with the magnetic inherent of the MG's which need to be considered by designers. These factors are as follows.

- Deflections: The concept of deflection in MG's stand for the deformation of the components mainly in two directions, radial and tangential. The tangential deformation is caused by the shear forces and the torques applied to the system and sub-components [68]. These forces are carried by the supporting components including the rods, crews, bars, keys, and pins. Not only the strength of such components should be monitored based on the applied forces and torques, but the mating parts should also be simulated and verified under the operational conditions. On the other hand, in the design of an MG, all the components in the active region are supported only at the two ends. Active region is the area of an MG with magnetic poles and ferromagnetic components. In the active region, not only the tangential forces are of great importance, but the forces in radial direction are more critical because the rotors are only separated by a very small air gap, as small as 0.5mm [50] or 1mm [69], and the forces are too high that bend the laminations and the support structures easily in the large-scale MG's [69].
- Eddy Currents: In general, iron losses originate from two sources in an electrical machine, namely eddy current losses and hysteresis losses [70]. The flux in the air gap of the magnetic gear includes harmonic components since the inner and outer rotors have the different pole–pairs and the rotational speeds. Thus, eddy currents are induced in the rare-earth magnets on the inner and outer rotors [71]. The eddy current in the material produces a flux density that opposes the impinging flux density of the system. In a magnetic gearbox, since there are at least three magnetic field with different

rotational speeds, the presence of a conductive material in the magnetic-field area with different speed results in the creation of eddy currents in the system, which not only decrease the flux density of the system, but it will result in the heat generation and temperature rise in the system [72]. This phenomenon demands special attention to the material selection and design of the MG's to ultimately avoid these currents and losses.

- Number of Pole Pairs: Number of pole pairs in an MG governs not only the gear ratio of an MG, but it also directly affects the torque ripple generated in the system. According to [65], the magnetic poles of the inner and outer rotors of an MG with modulating pieces are modulated through the modulation magnet ring to generate the harmonics in the air gap. The first harmonic transmits torque and the harmonics produce the torque ripple. Based on [65], torque ripple is calculated as follows.

$$T_{ripple\_i} = \sum_{n=1}^{\infty} S_{n\_i} \sin\left(nU_i\left(\omega_i t - \theta_{i0}\right)\right) \tag{2.1}$$

in which n is any natural number; when $i = 1$, T_{ripple_i} is the torque ripple of the inner rotor; S_{n_i} is the Fourier coefficient; U_i is the minimum common multiple of the number of pole pairs of the inner rotor P_i and the number of cores of modulation magnet ring ns; ω_i is the speed of inner rotor; θ_{i0} is the angle of the initial stage of the inner rotor. This shows that the torque ripple is related to the pole pair numbers, whether for the rotors with magnets or the modulating pieces. The higher torque ripple results in the higher vibration and noise in the system which is not desired, so the pole pair combination is a governing criterion in the design of an MG.

- Levelized Cost of Manufacturing (LCM): Magnetic gearing technology is a relatively new and growing technology compared to the traditional mechanical gearboxes. There are several factors in the manufacturing of an MG that makes it costly, such as the rare-earth magnet price, the cost of non-magnetic strong materials used in the active region, the high precision manufacturing due to the small gaps and small area of error, and the costly assembly jigs and equipment [68].

2.3.5 Failure Modes

2.3.5.1 Structural Considerations

In order to initiate the mechanical design of the magnetic gearing system, following primary structural concerns and considerations need to be addressed.

- Shear stresses on the supporting components, in/out of active region.
- Minimum reliable air gap in active region based on bending analysis.
- Lamination stack's mechanical support contribution.
- Manufacturing tolerances and optimizing it based on the effect on performance.
- Magnetic field losses and thermal effects.
- Oscillating forces and resonance.
- Assembly approach of the three so-called rotors based on force calculations.
- Material selection based on mechanical and magnetic simulations.

2.3.5.2 Shear and Bending Failure

As noted previously, the attractive and repulsive forces between magnetic poles are responsible for the transmission of torque in the gearbox. Magnetic flux between the inner and outer rotors modulated through an array of magnetic pieces called the cage rotor. While only the tangential forces contribute to the torque transmission, magnets produce significant radial forces, as well. These forces are calculated based on the material properties of the magnets and the surrounding steel as well as the geometric layout of the magnets and the associated flux focusing and flux modulating components. The supporting plates and rods passing through the active region mostly carry tangential loads. Radial forces have direct influence on bending of the components in active region lead to reduction of air gap, which could be a critical factor in designing large-scale magnetic gearboxes, knowing that the air gap is in the scale of few hundreds of micrometers. Figure 2-14 shows a deflected cage rotor lamination due to strong radial forces.

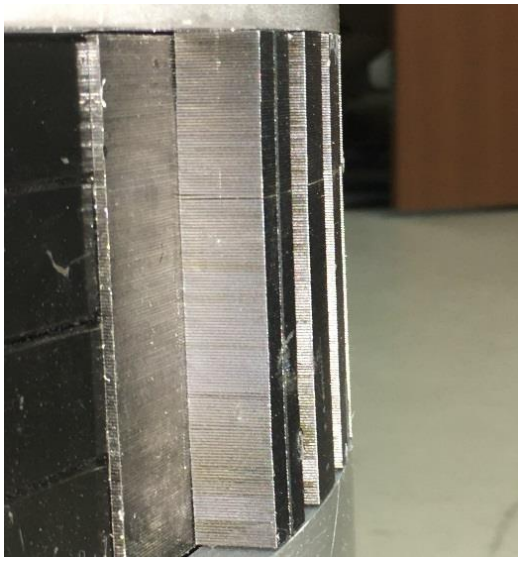

Figure 2-14: Bent cage rotor lamination [73].

D. E. Hesmondhalgh and D. Tipping first introduced inherent problems come with the production of magnetic gears [74]. In their coaxial design, the radial and tangential forces, transmitted torque and air gap reduction due to radial forces were discussed to provide higher efficiency for the system. Force analysis between the magnets of the rotors using a semi-numerical method was presented by J. F. Charpentier and G. Lemarquand [75] which makes it the one of the first attempt for mechanical analysis of magnetic gears.

Torque density is another aspect of magnetic gear design, which previously held back researchers to go through comparing magnetic gears with their mechanical counterparts. A comparative study have been done one the influence of laminated stator core versus solid iron core on system performance in [76], although this paper neglected mechanical considerations of the laminated parts in application. Mechanical Deflection within solid steel bars in a flux focusing magnetic gearbox was studied by Kiran K. Uppalapati and Jonathan Z. Bird [77], in which, an iterative approach had been conducted to evaluate magnetic forces on steel bars whilst air gap between magnets and solid steel bars is reducing. Along with the combination of pole pairs in magnetic gearing, design of the components in active region is of high importance for the system's performance. In [78], D. Z. Abdelhamid and A. M. Knight investigate the influence of cage rotor design on magnetic gear torque, although this study do not cover the manufacturability and mechanical aspect of the design. J. H. Lee et. al. [79] also proposed a study on the topology of modulating components of a radial magnetic gear.

2.3.5.3 Thermal Failure

Despite the non-contact feature of the MG's which prevents frictional losses and temperature rises, there are other sources of power losses originated in magnetic field,

including Hysteresis losses and Eddy current losses [80]. Hysteresis losses are resulted by the exposure of a ferromagnetic material to a varying magnetic field, since a certain amount of power is needed to magnetize and demagnetize the material magnetization path, depending on the position of the B-H curve. On the other hand, eddy current losses are caused by a magnetic field passing through an electrical conductor. Eddy current losses dominate the losses in magnetic gearing systems [81]. There has always been an interaction between thermal and electromagnetic design. Therefore, it is necessary to analyze both at the same time to get the best results. To design an efficient electromagnetic system, a multidisciplinary approach between mechanical and electrical engineering should be followed. Temperature distribution inside the electro-magnetic system due to heat generation should be analyzed because the high temperature inside decreases the system efficiency and laminations and demagnetize the permanent magnets. If the range of temperature inside the system is not high enough to interfere with the system performance, the natural convection outside the system performs the cooling process; otherwise, a cooling passage should be designed. For small sized magnetic systems with small angular velocity input, the range of temperature is not high and does not exceed the limitations for the inside components, so natural convection would be effective enough for the cooling process. Figure 2-15: Figure 2-15 shows a thermal image of a magnetic gearbox connected to an AC motor.

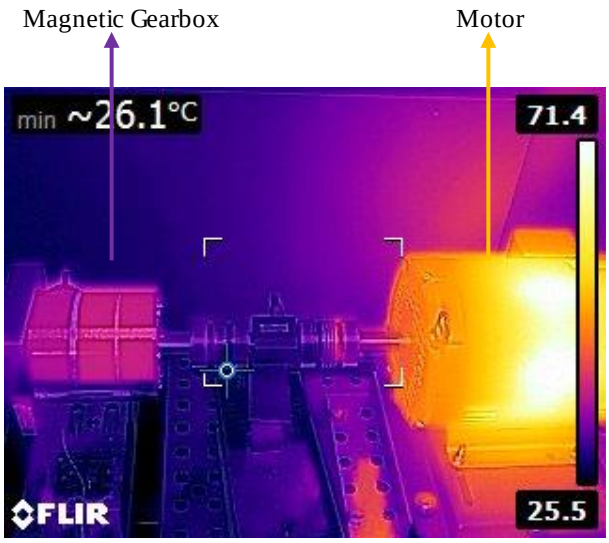

Figure 2-15: Thermal image of a magnetic gearbox connected to an AC motor.

In the last decade, thermal analysis calculations have been a focus of attention due to the important role they play in the design of electromagnetic systems and the use of in-house codes or software has become more popular since the advancement of computer technology. Thus, the optimization and design process have become faster and more precise [82]. Thermal analysis and flow field in the magnetic systems are studied numerically due to the complex geometry. All forms of heat transfer, convection, conduction and radiation are coupled in the system and numerous active thermal exchanges make the analysis too complex. As a result, analysis of all kinds of heat transfer phenomenon should be done simultaneously. Besides, the fluid flow analysis is difficult to study analytically so, scientists are taking advantage of experimental fluid dynamics (EFD) to observe thermal field and fluid flow [83]. The flow and temperature field in the magnetic gearbox are presented; however, a number of researchers have done studies on electromagnetic motors numerically and experimentally. Chang et al. [84] have investigated thermal performance of a large scale electromagnetic motor design through a

numerical approach, using fluent software package to predict the temperature field inside the system and also experimental studies. The calculated data shows a great agreement with the measured data. Thermal gradients, temperature field and thermal flux are reported by Srinivas and Arumugam [85] for a switched reluctance motor (SRM) through a thermal analysis of magnetic motors by Finite element method. Thermal fluid analysis is also studied by Li et al. [86] focusing on air cooling in a permanent magnetic motor numerically and experimentally. They reported that the cooling flow rate is proportional to the rotor speed and is a critical factor in the magnetic motor design. Based on the literature, the importance of the flow and temperature field on the electromagnetic system design is evident, especially for the scaled-up design with higher rates of losses. This suggest a comprehensive analysis and simulation of the MG systems.

2.3.5.4 Dynamic Behavior

During operation of an MG system, magnetic pole pieces serve as the modulator of the magnetic field in the two air gaps [87]. Since permanent magnets are covering specific sections of a full circle for each rotor, based on the gear ratio and arrangement of the pole pairs, there would be cyclical loads between rotors due to the relative motion of the segmented magnets. These oscillating forces applied to the three rotors would result in vibrations within the system, which would be of great importance due to the existence of very small air gap between inner, cage and outer rotors. Figure 2-16 shows the engagement and separation areas of the three rotors relative to each other.

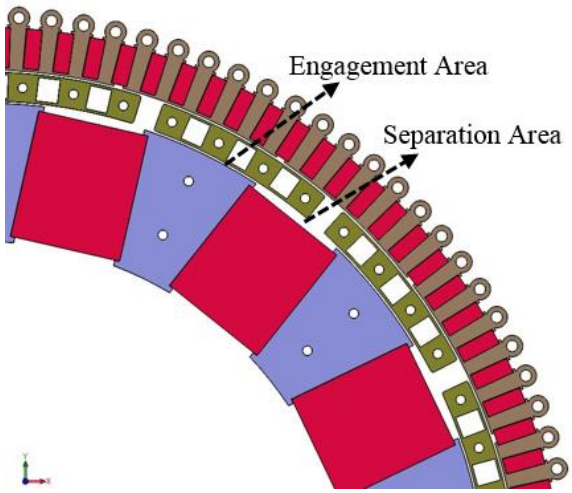

Figure 2-16: Engagement and separation areas in a radial magnetic gearbox [88].

Vibration analysis of magnetic gears has not been studied widely, maybe due to the fact that most of the efforts in this field has been conducted only on magnetic design phase. Entering the manufacturability phase and mechanical design requests further analysis on the components and the whole assembly, including dynamic analysis as well as structural, thermal and maybe fatigue analysis. P. Elies and G. Lemarquand [89] are one of the first researchers studied stability of magnetic structures, on a magnetic couplings. They presented a stable magnetic coupling through analytical force analysis between magnetic arrays. Note that radial position of magnets is fixed, but there is a relative motion in axial direction between the only two arrays of magnets in this coupling. T. H. Fay and L. Mead [90] modelled the motion of permanent magnets relative to each other by an elementary spring model, in a setup in which one magnet is suspended at one end of a vertical spring, holding directly above a second magnet fixed on the floor. Based on this study, interacting force depends on the distance, non-linearly, of the order -4. In 2010, R. G. Montague, C. M. Bingham and K. Atallah [91] studied dynamics of magnetic gear for servo control, which is based on the torque and force analysis of the magnetic gear. L. Xu and X. Zhu

[92] are of the first researchers investigating vibration analysis of the magnetic gears. A planetary gearbox is considered for the analysis for which, interacting forces are modelled as radial and tangential springs, and all the components are considered as rigid bodies. Nonlinear Forced vibration of a nested magnetic gearbox is proposed in [93]. In this study, dynamic model derived through considering interacting forces as springs, whether between permanent magnets and modulating arrays or between ferromagnetic pole pieces and stator. In [94], reluctant network analysis (RNA) is employed to conduct a dynamic analysis on planetary-type magnetic gear. In this method, each component, divided into small pieces, each expressed in a 2-D magnetic circuit. In one of the most recent papers, J. Lee and J. Chang [95] studied vibration characteristics of a coaxial magnetic gear through a 3D finite element analysis.

2.3.6 Additional Challenges

2.3.6.1 Assembly

Besides the challenges and considerations associated with the magnetic inherent of the MG's, as well as the design criteria and operational conditions, the presence of the strong magnetic fields not only affect the structural configuration of the system, but also affect the assembly approach in different ways. Starting from the assembly equipment, using the magnetic tools in the active region and close to the PMs is not possible, so it is necessary to shift to the non- magnetic tools, which either are expensive or weaker than their steel counterpart. Furthermore, inserting each magnet in the active field is a challenge as large forces, whether attraction or repulsion, are applied once a magnetic piece is approaching the magnetic field of another magnet. This dictates the necessity of guide parts

during the assembly process [68], which adds up to the final cost of the manufacturing. The small gap between the rotors is another challenging factor during the assembly, for which some researchers utilize shims to maintain the air gap during the assembly [69]. Larger magnetic gears bring more challenges associated with the geometric size, manufacturing limitations, material selection and the elevated forces. As reported in [68] and [90], for large magnetic gears, the manufacturing limitation for having a single stack modulating pieces is not feasible, which leads to the lack of supportive and force- balancing effect of all modulating pieces on each other. This leads to the requirement of the new assembly approaches, such as segmented and radial approaches besides the traditional axial assembly [68].

2.3.6.2 Differing Process Tolerances

The specific characteristics of the MG's and their need for high precision, especially in active region and for the purpose of radial alignment, results in the restrictions and limitations in selecting the manufacturing process of the magnetic gears' components. In the active region, for instance, highest precision is required for the features which are effective on the radial positioning and alignment of the components. This is inevitably associated with levelized cost of machining. The tightest tolerances/ highest precision in a magnetic gear is asked for the hole position and the manufacturing of the modulating pieces. +/-0.025mm is tightest tolerances for the manufacturing of the parts in [50], [69], [97], [98]. for the laminated modulating pieces, the manufacturing process is laser-cut, and the tightest tolerance possible for this process is +/-0.076mm [99]. For the hole sizes, the reaming process is recommended which has the precision of 0.02 to 0.05 mm. These tolerances compared to the 0.5mm of air gap are considerably small (10%) [100]. The

components and dimensions engaged in the axial positioning of the components are of looser tolerances. +/-0.05mm is recommended for the mating components and geometries, and the other components and geometries are of +/-0.1mm tolerance. For the keyways, high precision is required and the broaching approach with +/-0.02mm to +/-0.05mm of precision is specified [100]. For the holes with loose tolerance required, the drilling process is specified with +/-0.1mm to +/-0.5mm tolerance [100]. Table 2-3 shows the range of tolerances for the various manufacturing process.

TABLE 2-3: Process Tolerances [100], [99].

Process	+/- General Tolerance (mm)	+/- Less Frequent Tolerance (mm)
Turning, Shaping, Milling	0.04 - 0.3	0.015
Drilling	0.05 - 0.3	0.03
Boring	0.03 - 0.15	0.015
Reaming, Broaching	0.015 – 0.05	0.004
Laser-cut	0.076	-

CHAPTER 3: METHODOLOGY

3.1 MAGNETIC DESIGN

While many topologies for magnetic gears have been investigated, this project utilizes a radial flux focusing coaxial arrangement consists of an inner rotor and outer rotor which house arrays of permanent magnets with alternating polarity and an array of magnetic flux modulating pieces called the cage rotor. The three rotors maintained with a small separation relative to each other. The number of modulating pieces on the cage rotor, along with the number of magnetic pole pairs on the inner and outer rotor determine the gear ratio between the low-speed/high-torque input (cage rotor) and the high-speed/low torque output (inner rotor) [62]. The torque transmission capability of the gearbox mainly depends on the magnetic field strength of the permanent magnets and the size of the air gap between various rotors.

The Multi-stage Magnetic gearbox is a radial configuration in which, for each stage, two sets of magnetic pole pairs as flux focusing components separated with an array of flux modulating magnetic steels, called the cage rotor. In this design there is an inner rotor, consisting of p_1 pole-pair permanent magnets (PM) rotating at ω_1, a middle rotor with n_2 individual ferromagnetic steel poles that can rotate at ω_2 and p_3 pole-pair PM outer rotor rotating at ω_3. The inner and outer rotors that contain PMs interact with the middle steel poles to create space harmonics. If the relationship between the steel poles is chosen to be $p_1=|p_3 - n_2|$ then the rotors will interact via a common space harmonic and the angular velocities for each rotor is [101]

$$\omega_1 = \frac{n_2}{n_2 - p_3}\omega_2 - \frac{p_3}{n_2 - p_3}\omega_3 \tag{3.1}$$

If the outer rotor is held stationary ($\omega_3=0$) the speed ratio will be

$$\omega_1=G_{12}\omega_2 \tag{3.2}$$

Where the gear ratio is

$$G_{12}= n_2/p_1 \tag{3.3}$$

Various mechanical aspects of magnetic gear technology in this study are studied on three topologies. The assembly models of the magnetic gearboxes designed, studied and manufactured in this research presented in, called Laminated Magnetic Gearbox (LMG), Multi-stage Magnetic Gearbox (MSMG), and Hermetically Sealed Magnetically Geared Generator (HSMGG), respectively. With outer rotor fixed ($\omega_3=0$) stage 1 gear ratio is $\omega_1=G_{12}\omega_2$ where $G_{12}= n_2/p_1$. For the stage 2 of the gearbox, one has:

$$n_5 = p_4 + p_6 \tag{3.4}$$

With the outer rotor fixed ($\omega_4=0$) the stage 2 gear ratio is $\omega_4=G_{45}\omega_5$, where $G_{45}= n_5/p_4$. Then combining gear ratios, the speed change ratio defines as

$$\omega_1 = G_r G_{45} = \left(\frac{n_2 n_5}{p_1 p_4}\right)\omega_5 \tag{3.5}$$

Therefore, the gear ratio, Gr, is

$$G_r = \left(\frac{n_2 n_5}{p_1 p_4}\right) \tag{3.6}$$

Total gear ratio for LMG, MSMG and HSMGG are 4.25:1, 59.01:1, and 63.33:1, respectively.

3.2 STRUCTURAL DESIGN

3.2.1 Static

Primary application of gearing systems is to transmit torque. Transmitted torque in such systems plays dominant role in creation of shear stresses in the system, which is essential in mechanical design, as well as material selection of the components of the gearbox. Input shaft connects to the cage rotor, so it is tolerating the highest amount of shear stresses in this gearing system, which makes it a great candidate to initiate shear stress analysis. The radial and tangential force densities in the air gap can be calculated using Maxwell's stress tensor [101].

$$f_r = \frac{1}{2\mu_0}\left(B_r^2 - B_\theta^2\right) \tag{3.7}$$

$$f_\theta = \frac{1}{\mu_0}\left(B_r B_\theta\right) \tag{3.8}$$

Where f_r, f_θ, B_r, B_θ, μ_0 are the radial force density, tangential force density, radial flux density, tangential flux density and the permeability in vacuum, respectively.

The magnetic torque can be calculated by using Maxwell's stress tensor [101].

$$T = \frac{dr^2}{\mu_0}\int_0^{2\pi} B_r(r,\theta)B_\theta(r,\theta)d\theta \tag{3.9}$$

Where d and r are the axial length of the magnetic gear and the radius of the integration path in the air gap, respectively. Shear stress calculations affect the selection of

the size and material of threaded rods passing through the modulating components, Key stock sizes, and spline shaft design, as well as end-plates dependable thickness. Shear stresses are calculated analytically using following equation [102].

$$\tau = \frac{QV}{Ib} \tag{3.10}$$

In this formula, Q is the first moment of inertia between the location where the shear stress is being calculated and the location where the shear stress is zero about the centroidal axis, V is the value of the shear force at the section, I is the moment of inertia of the entire cross section about the centroidal axis, and b is the width of the cross-section at the location where the shear is being calculated [103]. Also, since this prototype is meant to be tested and used for experimental purposes, a safety factor of 2.5 is considered as a dependable S.F. value for predictable lab situation to be the first mechanical factor to be evaluated in magnetic gearing design. Regarding material of the components, shear calculations shows that Aluminum 6061 is fairly a good candidate for endplates, but due to the high torque values applied to the low speed rotor, approximately as high as 14 KN.m in full-load situation, as the appropriate material, steel 4041 is selected for manufacturing input and output shafts. In addition, for the rods passing through modulating components of the system, tool steel is the considered material.

The rod's radial deflection, Λ_d, was computed using [104]:

$$\Lambda_d = \frac{F_r}{384E}\frac{l^3}{I_c} \tag{3.11}$$

Where F_r = radial force, l = length of the rod, E = Young's modulus and I_c is the inertial of the circular rod. The circular rod's inertia given by

$$I_c = \frac{\pi d^4}{64} \tag{3.12}$$

Where *d* is rods diameter. Substituting (3.11) into (3.12) gives

$$\Lambda_d = \frac{F_r}{6\pi E}\frac{l^3}{d^4} \tag{3.13}$$

Equation (3.13) shows that as the diameter increases the amount of deflection will increase.

3.2.2 Dynamic

Multi-stage magnetic gear box (stage 1) is designed as a system of masses, springs and dampers. Assumptions for this model are as follows:

- Attraction and repulsion between magnets are modeled as net forces applied to each rotor. These forces are extracted from simulation of the system in JMAG software.
- Bearings are modeled as a set of spring-mass-damper [105], [106], knowing that stiffness is of the order of $x^{3/2}$.
- Input shaft and output shaft are modeled as one shaft, because they are almost equal in their cross-section area, plus they are connected through a ball bearing.
- Shaft is divided into three parts in order to be able to have the effect of bending on the different rotors.

In order to calculate the mass, stiffness and damping values in the MG systems, followings are considered:

- Mass values are calculated using SolidWorks material library, through modeling all the parts and assigning material for them.
- Stiffness for shaft portions and laminations are extracted from bending deflection of the parts, plus related equations in [104].
- Stiffness of the end plates are calculated using equations of displacement under axial load, in addition to a factor of 0.76-1 which is extracted through comparing displacement of a single bar under axial load with simulation results in SolidWorks software.
- Damping constants of the bearings are derived using [105], [106].

Stiffness values of the system is extracted from a superposition approach between the normal modes values formulated for uniform beams with various boundary conditions [107]. The boundary conditions for the active region components are considered as clamped- clamped, while for the endplates, boundaries are clamped- pinned. According to [107], Euler's differential equation for uniform beam is,

$$EI\frac{\partial^4 y}{\partial x^4}+m\frac{\partial^2 y}{\partial t^2}=0 \tag{3.14}$$

In which, E is modulus of elasticity, I is moment of inertial, and m is mass density per unit length of the beam. Verified formula of Euler beam's natural frequencies with Finite Element Analysis is as follows [107]:

$$f_n=\frac{(\beta_n l)^2}{2\pi l^2}\sqrt{\frac{EI}{\rho A}} \tag{3.15}$$

Where, l is length, ρ is density and A is cross section of Euler beam. In addition, β_n stand for mode shapes constant value. Values for $\beta_n l$, for clamped- clamped and clamped-

pinned boundary conditions are calculate according to following formulas, respectively [107].

$$\beta_n l = \frac{(2n+1)\pi}{2} \tag{3.16}$$

$$\beta_n l = \frac{(4n+1)\pi}{4} \tag{3.17}$$

In which, *n* is the normal mode number.

3.3 THERMAL DESIGN

3.3.1 Eddy Current Losses

Non-contact inherent of magnetic gears provides an opportunity to avoid many structural and performance issues originating from mechanical/ contact losses in mechanical gearboxes, although, presence of bearings as the only components with mechanical contact should be considered. Despite absence of mechanical contact in active region, rotary magnetic components and fields result in magnetic, especially with demands for higher torque ratio and efficiency. The total loss and efficiency of the magnetic gear in case $\omega_3=0$ can be calculated by [50]

$$P_{loss} = T_2\omega_2 - T_1\omega_1 \tag{3.18}$$

$$\eta = \frac{T_1\omega_1}{T_2\omega_2} \tag{3.19}$$

Where T_1 and T_2 are the torque on the inner rotor and cage rotor, respectively. P_{loss} can also be separated in three categories, including hysteresis losses (P_h), eddy current losses (P_e), and mechanical losses (P_m) [62].

$$P_{loss} = P_h + P_e + P_m \tag{3.20}$$

Eddy current loss occurs as a result of a travel of a magnetic field passing into an electrical conductor inducing current that flows within the core [108]. As there is no stator in the system and the iron cores are minimal, eddy current losses correspond for the main portion of losses in magnetic gears. Eddy current power loss and its corresponding torque can be calculated as follows [109].

$$P_{eddy} = K_{eddy} B_{\max}^2 \left(\frac{\omega_{re}}{2\pi} \right)^2 \tag{3.21}$$

$$\tau_{eddy} = \frac{K_{eddy} B_{\max}^2 P_b}{8\pi^2} \omega_{re} \tag{3.22}$$

Where K_{eddy} is eddy current loss coefficient (Nm/T^2 rad/s), P_b stands for the number of poles, and ω_{re} is electrical velocity (rad/s), which is in related with mechanical angular velocity (ω_{rm}) by [108]:

$$\omega_{re} = \frac{P_b}{2} \omega_{rm} \tag{3.23}$$

Having large conductive materials close to active region without insulation makes a major contribution in eddy current losses in magnetic gears. Main conductive materials used in this design, which lead to levelized losses in MG, are the steel supporting rods passing through laminated stacks of inner, cage and outer rotors, as well as the aluminum endplates touching active region component. It worth mentioning that aluminum plates will be a great concern for large magnetic gears in which axial length of the active region is fairly small in comparison with aluminum endplate size. Common approaches to avoid eddy current loss issue are (1) applying insulation between conductive support materials

and the laminations, and (2) altering material of support components to non-conductive options. In [70], K_{eddy} is broken down to the following formula:

$$K_{eddy} = \frac{\delta^2}{24\rho} \tag{3.21}$$

In which, δ stands for the thickness of the material and ρ is the resistivity of the material. Researchers used this concept to decrease the eddy current losses in electrical machines by using laminated stacks instead of solid blocks of electrical steels. Laminated stacks consist of thin layers of electrical steel coated with a thin layer of bonding agent, oven cured and fused together. Small thickness of these lamination layers drops down the eddy current loss with the second order ratio. This property is widely used in the electrical machine and magnetic gearboxes for the modulating pieces, but the concept is recently used for generating laminated magnets [110].

3.3.2 Convection Method vs Conduction

Numerical computations were accomplished using commercial CFD software ANSYS which is being widely used for prediction of flow field and heat transfer studies. Due to the complexity of the geometry, the best way to explore the flow field and flow behavior such as the air gap or passages between windings is the numerical method. There are two moving components in the system, which makes it difficult to measure temperature. The flow and thermal analysis were coupled and velocity field and temperature distribution were predicted. The laminar flow and heat transfer in the magnetic gearbox are described by the Navier-stokes (NS) equations, continuity and Laplace equation [111]. To predict the

flow structure, Euler's method in the Cartesian coordinate system is used. Transport properties are considered as temperature independent properties as the operating temperature range is small. Reynolds number is used to determine the flow regime. Because value of Reynolds number does not reach the critical value, which is 2300-2500 in the domain, the flow regime is definitely laminar. For rotating object annular system, Reynolds number is calculated as:

$$\mathrm{Re} = \frac{R\omega D_h}{\upsilon} \tag{3.22}$$

Where ω, υ, and D_h are the angular velocity, kinematic viscosity and the air gap distance, respectively. The velocity field, pressure, and temperature distribution are predicted through CFD analysis. The solid-fluid interface temperature is calculated during the coupled method. The coefficient of heat transfer (CHT) is finally evaluated using the bulk temperature (K), wall temperature (K), and heat flux (W/m2) on the solid-fluid boundaries. Thermos-physical properties of solid components are considered constant. Component's thermal conductivity plays important role in the temperature distribution in the solid domain. Heat flux is calculated and temperature gradients are evaluated based on thermal conductivity. TABLE 3-1 lists the thermos-physical properties of solid components. Two values are listed for laminations thermal conductivity, which stands for in-plane (X and Y) and normal-to-plane (Z) directions. Material of the laminations is Electrical Steel grade NO12, with C-5 surface coating.

TABLE 3-1: Thermo-physical properties of components [112], [113].

Material	Thermal Conductivity (W/m.K)	Specific Heat (kJ/Kg.K)	Density (Kg/m3)	Young's Modulus (GPa)
Magnets (NdFeB)	8.95	450	7600	160
Steel 303	16.3	530	8030	193
Steel 1018	51.9	486	7870	200
Lamination (NO12)	28 & 0.37	504	7650	185

Peripherally average coefficient of heat transfer (CHT) given by:

$$h = -k_f \frac{(\partial T / \partial y)_{y=0}}{T_s - T_b} \tag{3.23}$$

Where T_s (K) and T_b (K) k_f (W/m.K) are area-weighted average wall temperature and the bulk fluid temperature gained by the following formula, and fluid thermal conductivity, respectively.

$$T_s = \frac{1}{L}\int_0^L T ds \tag{3.24}$$

$$T_b = \frac{\int \rho u c_p T dA}{\int \rho u c_p dA} \tag{3.25}$$

The heat losses are first calculated by the Fast Fourier's Transform in MATLAB in a magnetic analysis under operation for a long time. The average value of the heat transfer coefficient on the housing is set based on an empirical correlation extracted from [114]; also the convective boundary condition, Neumann's BC, is applied.

$$-k\frac{dT}{dr} = h(T_s - T_b) \tag{3.26}$$

Where *r* is the radial direction and *k* is the solid thermal conductivity. To estimate the external flow coefficient of heat transfer for the lab environment, Churchill and Chu [114] recommended a single correlation average Nusselt number (*Nu*) laminar steady-state free convection of heat transfer from a horizontal isothermal cylinder for a wide range of Rayleigh number.

$$\overline{Nu} = \left\{ 0.6 + \frac{0.387 Ra^2}{\left[1 + \left(\frac{0.559}{\Pr} \right)^{\frac{9}{16}} \right]^{\frac{8}{27}}} \right\} \quad Ra \le 10^{12} \tag{3.27}$$

In which R_a and P_r are Rayleigh number and Prandtl number, respectively calculated as following:

$$Ra = \frac{g\beta(T_s - T_\infty)D^3}{\upsilon\alpha} \tag{3.28}$$

$$\Pr = \frac{\upsilon}{\alpha} \tag{3.29}$$

Parameters are defined in TABLE 3-2. T_∞ is the ambient temperature and the fluid properties are calculated at a film temperature (average of ambient and surface temperature) of 310 K.

TABLE 3-2: Fluid properties at film temperature of 310 K.

Parameter	Value	Unites
Thermal conductivity, k	0.03	W/m.K
Kinematic viscosity, υ	1.75×10-5	m2/s
Thermal diffusivity, α	2.45×10-5	m2/s
Prandtl number, Pr	0.71	-
Volumetric thermal expansion, β	3.14×10-3	K-1
Rayleigh number, Ra	6.17×106	-

3.4 MESH STUDY

Finite Element Analysis (FEA) is used in all levels of design, testing and validation of the MG's. Calculating the magnetic forces, torque values, eddy current losses on one side, and deflection, thermal and stress analysis on the other side are the examples of the application in which FEA is playing the major role. A critical factor in FEA is to find the optimized mesh size for different parts and sections of the system to achieve the results with minimum error and to keep the number of nodes as low as possible to save the calculation time and required memory for the system. For the sake of mesh study in different modeling processes of the MG analysis, three levels of simulations are studied, including:

- Mesh study for magnetic analysis and force calculations.
- Mesh study for structural analysis and deflection calculations.
- Mesh study for thermal analysis and temperature calculations.

For the magnetic analysis, all the components in active region should be modeled and meshed including all the solid parts like magnets, laminations and rods, in addition to the air gaps between different rotors, and the surrounding air. An adaptive mesh study is conducted on the second stage of the multi-stage HSMGG design to find the optimized

element size and the locations with the highest rate of mesh aggregation. TABLE 3-3 shows the mesh study results for the system. It shows that among 12 adaptive steps of meshing the model, the first 6 steps show more than 1N of force variation (more than 0.01 of error for the 5th step). The final adaptive mesh for the 12th step is shown in the Figure 3-1. It is shown that the highest mesh aggregation is in the area close to the air gaps, and the cage rotor tips and bridges have the smallest mesh size. Note that the surrounding air has the coarsest mesh size.

TABLE 3-3: Adaptive convergence list for magnetic analysis and force calculations (Data by H. Baninajar, PSU).

Refinement Stage	Elements	Force Variation [N]	Max. Error
0	4728		74.13000
1	36682	267.30000	3.93300
2	130564	30.62000	0.20570
3	166296	3.84100	0.05857
4	174552	2.02000	0.01175
5	175912	1.00000	0.00847
6	176106	0.57440	0.00505
7	176342	0.06803	0.00188
8	176382	0.06346	0.00134
9	176414	0.02451	0.00186
10	176430	0.03656	0.00158
11	176452	0.11300	0.00154
12	176462	0.00541	0.00100

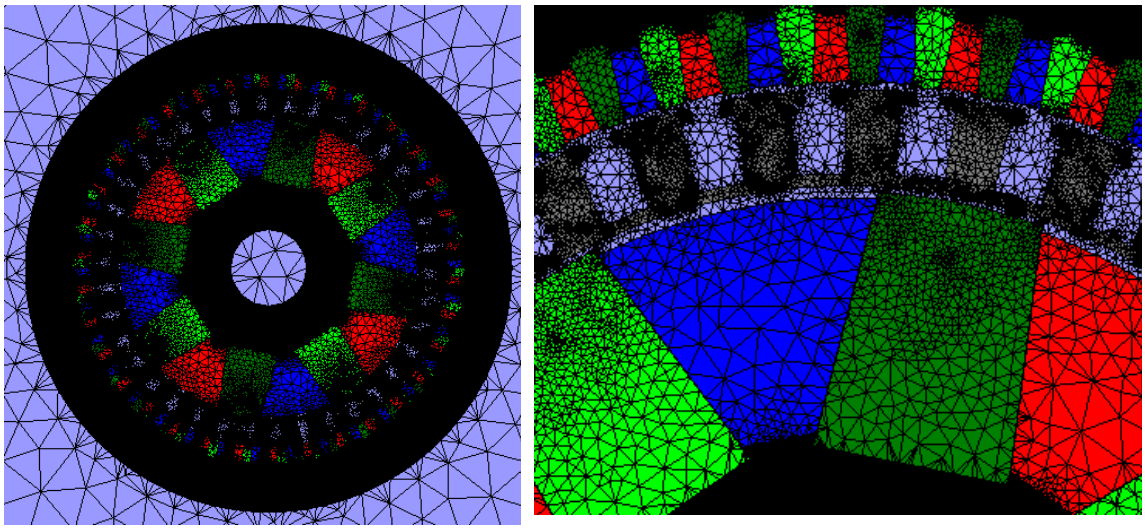

(a) (b)

Figure 3-1: Final adaptive mesh for the 12th step of the adaptive convergence, (a) full view, and (b) close-up view (Figure provided by H. Baninajar, PSU).

For the deflection analysis of the mesh study is conducted on a test setup which is assembled for the evaluation of the lamination bonding simulation under the bending loads. This setup comprises a set of laminations with 160 layers in axial direction connected with a bonding agent. A steel rod passes through the laminations to provide the support and connection to the endplates. For this analysis, only half of the system (in axial direction) is simulated due to symmetry condition. TABLE 3-4 shows the mesh study results for the system. It can be seen that the deflection results quickly, after 5 steps of refinements, converge to the values with less than 0.0004mm of changes in maximum deflection, equal to 0.35% changes compared to the previous step. With this mesh study which is conducted in ANSYS software, most of the refinements are applied automatically to the connection area between the rod and the laminations. So, the finest elements are in the area of these contact surfaces. On the other hand, laminations are divided into two elements in axial direction, although there are a couple of laminations in which 3 elements are observed. So,

For the final mesh sizes, as shown in Figure 3-2, the laminations are divided into 3 elements in axial direction, the general mesh size is 0.75mm and the contact area between the rod and the laminations are divided into 100 segments.

TABLE 3-4: Mesh study results for deflection analysis of the test setup.

Refinement stage	Elements	Max. Deflection [mm]	Error (%)
0	30280	0.117009	-
1	189990	0.115204	1.5426
2	217172	0.114537	0.5789
3	630531	0.113819	0.6268
4	1647210	0.113420	0.3505

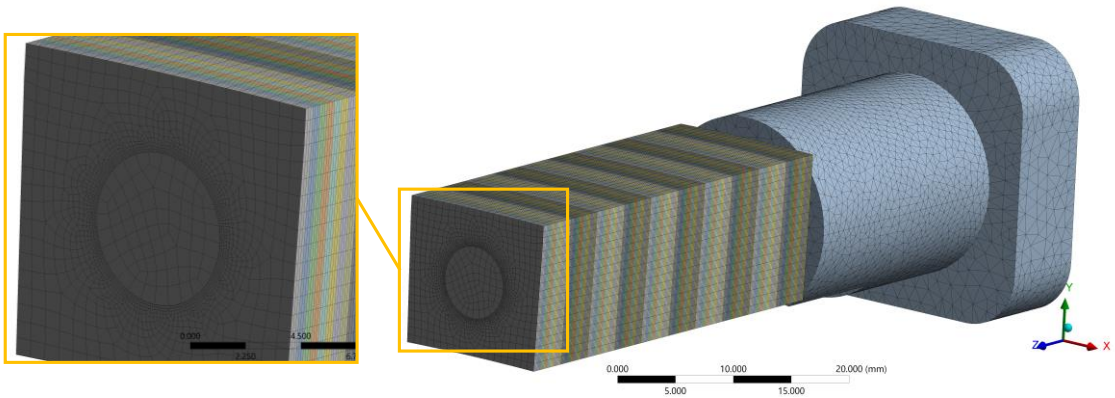

Figure 3-2: Final meshing for the test setup model.

For the thermal analysis, a mesh study is conducted on the XY view of the model. The mesh study is started with the 10390 cells in a quarter model of the system, which causes 3 elements in radial direction of the air gap. Figure 3-3 shows a comparison between the temperature along the outer air gap of the LMG, shows in Figure 3-4. In this comparison, number of elements along the radial direction of is increasing from 3 to 17. The results show a dependable agreement between the results with more than 30000 elements in a quarter model of the cross section, and 17 elements in the air gap. As the

result of the mesh study, a fine mesh in the air gap region and the lamination corners close to the air gaps are considered. The fluid flow and solid domains use fully structured and unstructured meshing, respectively. Mid-span cross section of the full model meshing and close-up of the gearbox boundary layer meshing is shown in Figure 3-5. A stringent grid test was performed to ensure solution independency of mesh size. A mesh with 1.91 million elements provided sufficient resolution. The grid resolution was studied near the solid-fluid interface to ensure the thermal and velocity gradients are captured. A highly dense grid was finally employed near the wall boundaries with the first layer height of 0.01 mm and growth rate of 1.1 over a 10-prism layer meshing structure.

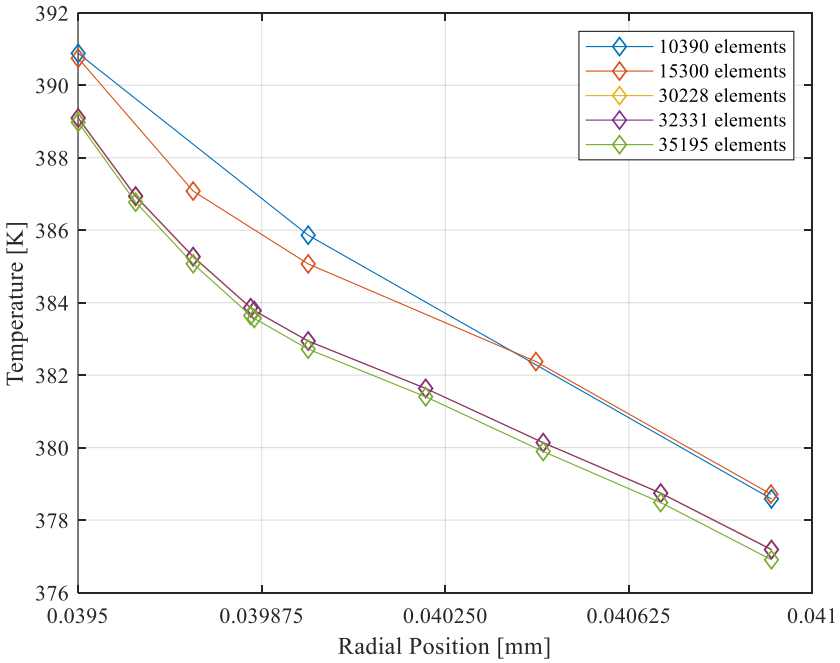

Figure 3-3: Temperature in the outer air gap for different element numbers.

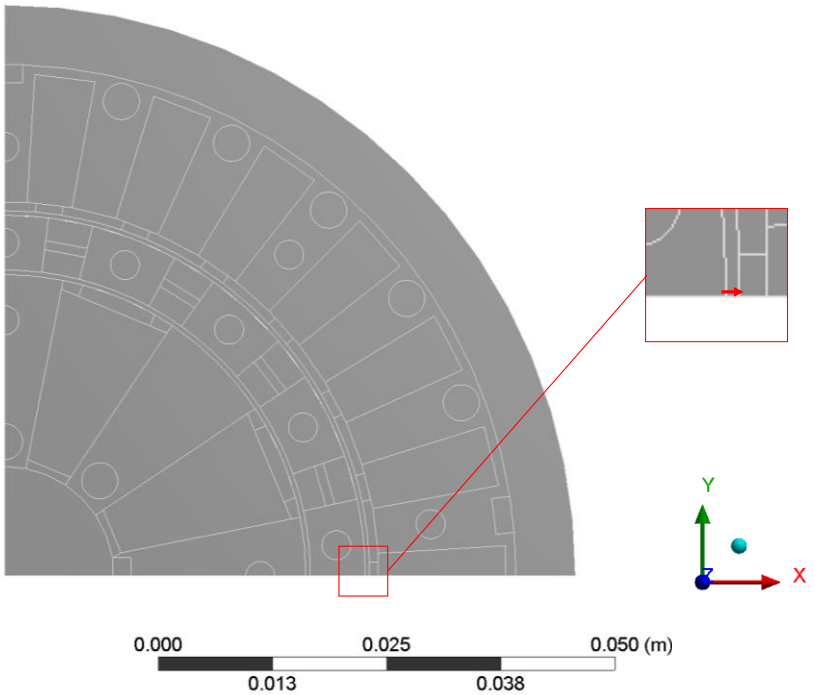

Figure 3-4: Quarter model of the LMG system and the mesh study region.

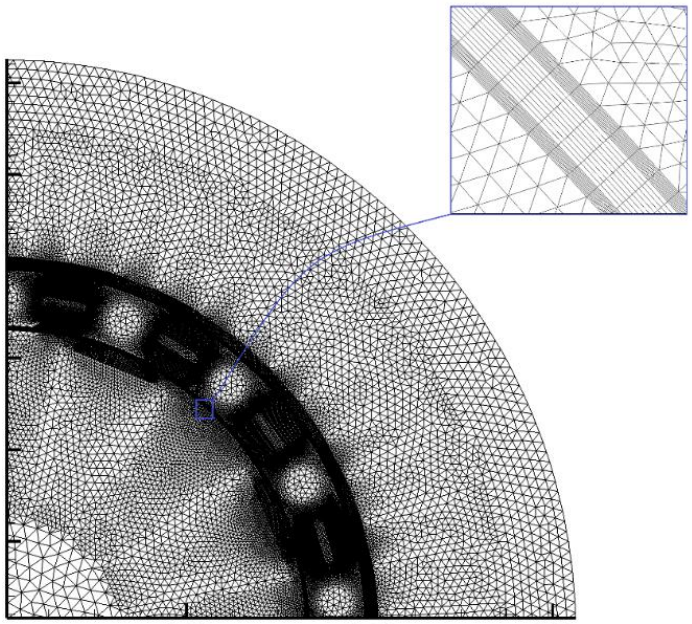

Figure 3-5: Mid-span cross section of Computational grid system [115]

CHAPTER 4: MECHANICAL DESIGN OF TWO MULTI-STAGE MAGNETIC GEARS

4.1 WIND (OBJECTIVES AND DESIGN DETAILS)

Wind turbine manufacturers are seeking for increasing the size of wind turbines to reduce the levelized const of energy (LCOE). Development of the wind turbine technology was integrated with the direct-drive permanent magnet generators' development, but the scale-up process results in a disproportionate increase in the structural size, mass and cost. This led the wind turbine industry investors to support superconducting generators in the wind turbine applications [116]. The objective of this project is to design, analyze, manufacture, and test a 30kW (at 30RPM) magnetic gearbox, with 59:1 gear ratio. For this purpose, a multi-stage magnetic gearbox is proposed. The gear ratio is selected to compare the MSMG design performance with the Sumitomo cycloidal gearbox as shown in Figure 4-1. The Sumitomo gearbox values and operating characteristics are summarized in TABLE 4-1 and TABLE 4-2, respectively.

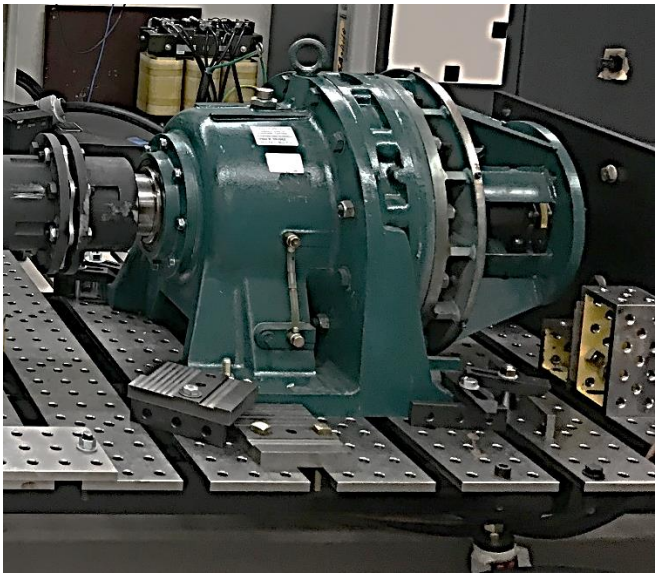

Figure 4-1: Fanuc PM servo motor connected in series with a 59:1 Sumitomo cycloidal gearbox (CHHJ-4225Y-59-320TC) [69].

TABLE 4-1: Sumitomo Cycloidal Gearbox Values [69]

Parameter	Value	Units
Outer radii	275	mm
Active region axial length	210	mm
Total mass	402.3	kg
Gear ratio, Gr	59	-

TABLE 4-2: Sumitomo Cycloidal Gearbox Operating Characteristics [69]

Operation Parameters	Input angular speed		Units
	1750 RPM	580 RPM	
Rated output torque	11.5	13.8	kN·m
Rated output power	35.8	14.2	kW
Efficiency (at rated power)	93	93	%
Volume torque density	230	277	N·m/L
Mass torque density	28.6	34.2	N·m/kg

The very initial design is a radially embedded design in which two magnetic gears with three rotors are combined radially inside each other. Outer rotor of the inner stage is physically connected to the inner rotor of the outer stage. These two rotors, outer rotor of the inner stage and the inner rotor of the outer stage, are Halbach design, while the other rotors are fully laminated designs. Figure 4-2 shows a schematic view of this design. There are benefits with this design, including very high peak toque compared to the previously designed MG's, as reported in TABLE 4-3, and high torque density, 636 kN.m/m3, which is around 200% higher than the best MG designed so far, and as high as the high-performance mechanical gearboxes. Despite the tempting numbers for the performance of such design, the complexity of the structure, the assembly issues with this model and the

deflection modes, radial and tangential, associated with this design are the key factors that drive the designers to shift to the series connected multi-stage magnetic gear.

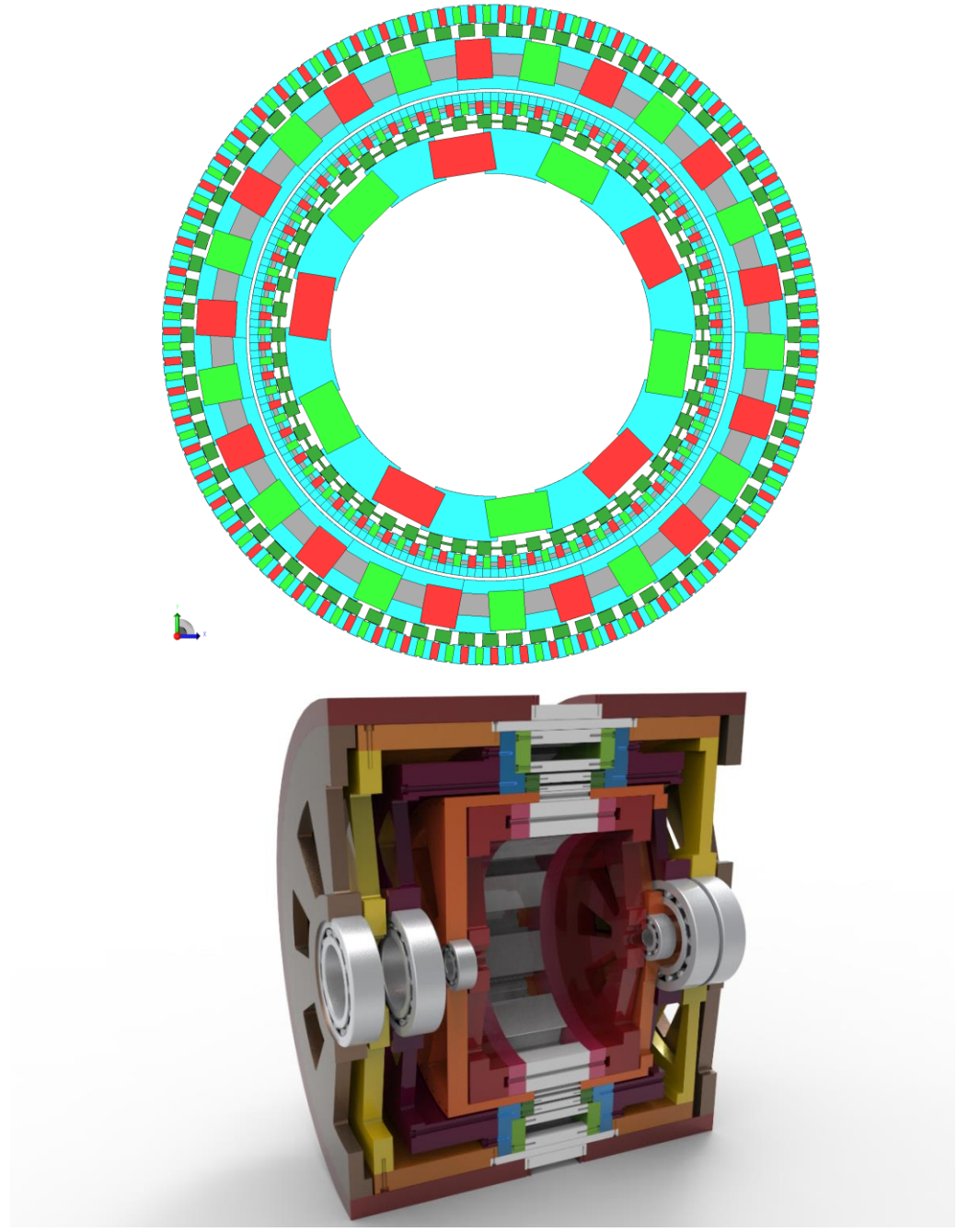

Figure 4-2: Schematic presentation of the radially embedded multi-stage magnetic gearbox, (a) Magnetic Configuration (By Kang Li), and (b) 3D model.

TABLE 4-3: Torque values on the six rotors of the proposed radially embedded multi-stage magnetic gearbox.

Rotor Name	Inner rotor, inner stage	Cage rotor, inner stage	Outer rotor, inner stage	Inner rotor, outer stage	Cage rotor, outer stage	Outer rotor, outer stage
Peak Torque [N.m]	-355	3790	-3401	2226	-13671	11449

For the series connected multi-stage magnetic gear (MSMG), two stages are defined. Stage one which is the high torque, low speed side, consist of three rotors, inner, cage and outer, radially assembled. Inner rotor is connected to the output shaft with high speed and low torque conditions, the cage rotor is connected to the input shaft which is the high torque, low speed side, and the outer rotor is fixed. The initial air gap between the rotors is defined as small as 0.5mm. The number of pole pairs for the inner and outer are 11 and 60, respectively, and there are 71 pole pieces in this design, resulting in the gear ratio of 6.45:1 for this design. Figure 4-3 shows the schematic presentation and 3D models of the magnetic arrangement for the first (a and c) and second (b and d) stages [117]. Second stage of the MSMG design has similar initial configuration as the first stage, but in smaller scale. The inner rotor is connected to the output shaft with high speed and low torque. The cage rotor is connected to the input shaft which is in fact the first stage output. The outer rotor is stationary in this design. This stage comprises 7 and 57 pole pairs in the inner and outer rotors, and 64 modulating pieces in the cage rotor, resulting in the gear ratio of 9.14:1 for the second stage. The total gear ratio of the whole assembly is 58.95:1. Note that the prime numbers for the pole pairs is intentional for the purpose of torque ripple reduction. Details of the geometric properties for the stage 1 and 2 of the MSMG design are listed in TABLE 4-4 and TABLE 4-5, respectively.

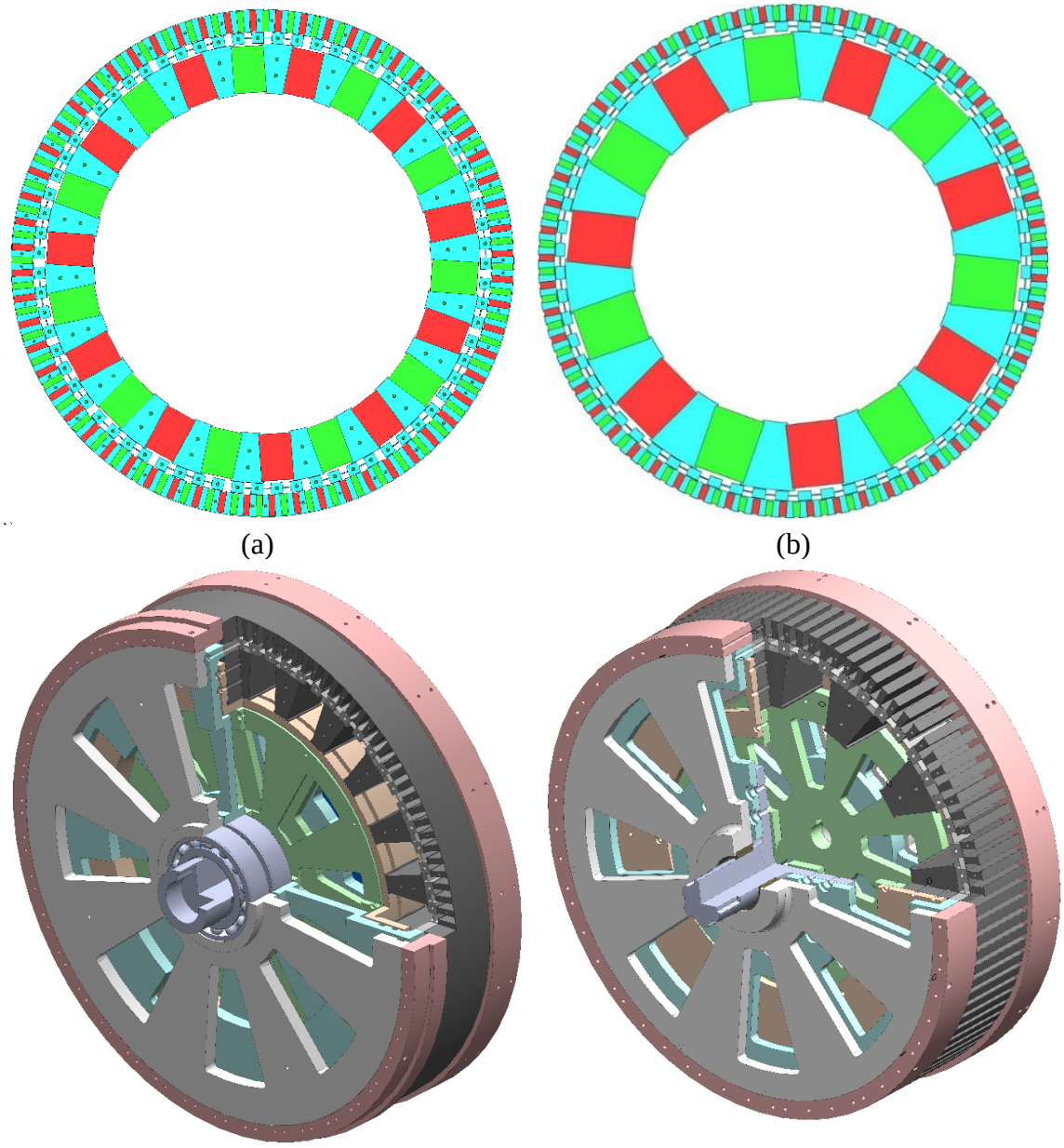

(a) (b)

(c) (d)

Figure 4-3: Schematic presentation (a & b by Kang Li) and 3D model (c & d) of the magnetic arrangement for the first and second stages of MSMG.

TABLE 4-4: Details of the geometric properties for the first of the MSMG design.

Description		Final value	Unit
Inner rotor	Inner radius, ri1	203.5	mm
	Outer radius, ro1	263	mm
	Pole pairs, p1	11	-
	Angular span, θ1	π/(2p1)	radians
Cage rotor	Inner radius, ri2	263.5	mm
	Outer radius, ro2	276.5	mm
	Pole pairs, n2	71	-
	Angular span, θ2	π/p3	radians
Outer rotor	Inner radius, ri3	277	mm
	Outer radius, ro3	304.04	mm
	Pole pairs, p3	60	-
	Angular span, θ3	π/(2p3)	radians
Axial length, d		76.2	mm
Gear ratio, G12		6.45	-

TABLE 4-5: Details of the geometric properties for the second of the MSMG design.

Description		Value	Unit
Inner rotor	Inner radius, ri4	155	mm
	Outer radius, ro4	213	mm
	Pole pairs, p4	7	-
	Angular span, θ4	π/(2p4)	radians
	Magnet length, h4	54	mm
	Magnet width, w4	47.25	mm
Cage rotor	Inner radius, ri5	213.5	mm
	Outer radius, ro5	226.5	mm
	Pole pairs, n5	64	-
	Angular span, θ5	π/p6	radians
Outer rotor	Inner radius, ri6	227	mm
	Outer radius, ro6	246	mm
	Pole pairs, p6	57	-
	Angular span, θ6	π/(2p6)	radians
	Magnet length, h6	17	mm
	Magnet width, w6	6.75	mm
Axial length, d		38.1	mm
Gear ratio, G45		9.14	-

4.2 MHK (OBJECTIVES AND DESIGN DETAILS)

This part of the project is focused on the development of a multi-stage hermetically sealed magnetically geared generator (multi-stage HSMGG) to radically improve the reliability and efficiency of the power-take-off (PTO) for a rotary based marine hydrokinetic (MHK) generator. The full-scale version of this design will be designed, manufactured and tested for a 50kW (at 40RPM) MHK generator. Here a subscale model is going to be designed, manufactured and tested. Water-tank test is going to be conducted on the hermetically sealed version of the design. The subscale version has the rated power of 5kW, gear ratio of 63.36:1, and input torque of more than 1193 N.m. The multi-stage HSMGG is designed to be system agnostic so as to enable it to be integrated into a range of rotary based MHK generators. By using a modular two-stage series connected approach different gear ratios and different peak torque values could then be utilized. Special attention is placed on demonstrating the efficiency of the multi-stage MGG. Volumetric torque density of 300 $kN.m/m^3$ is set as the target for this design with the efficiency of 90%. Manufacturing a multi-stage configuration with new assembly approach, high torque density, addressing the mechanical barriers and failure modes, improved efficiency and a unique hermetically sealed design are of the top goals of this design. The very initial proposed design for this system is shown in Figure 4-4. This particular design comprises two stages of radial MG's, connected in series. For the first stage, the outer rotor is rotary and connected to the input shaft. The cage rotor is stationary and the inner rotor is connected to the output shaft with high speed and low torque. One reason for this topology alteration is the sealing process which is much feasible with the stationary cage rotor. The second stage is configured similar to the MSMG design, i. e. with the fixed outer rotor,

high speed/ low torque inner rotor and low speed/ high torque cage rotor. For this design, outer rotor of the first stage is Halbach design, for which three types of magnets are arranged to achieve maximum flux focusing.

The Hermetically Sealed Magnetic Gear Generator (HSMGG) is designed to pull off submarine tests. This magnetic gear generator is for a Marine Hydro Kinetic Generator. Sealed area of the magnetic gear is indicated in Figure 4-4 by gray color. Cage rotor of the first stage and outer rotor of the second stage are the boundaries of the sealing. Outer rotor magnets of the first stage will also be coated with waterproof material to make sure magnets and laminations will not be damaged. First attempt to seal the designated area is to make sure all the sealing parts are fully connected and no gap is in the design. For this purpose, sealing components for the cage rotor of the stage1 and outer rotor of the stage2 are designed to separate the two regions. A list of components in contact with water are listed in TABLE 4-6. The second attempt to complete the sealing is to cover the magnets, laminated components and Garolite/ Delrin components with a thin layer of waterproof glue, called moist metal grip [118].

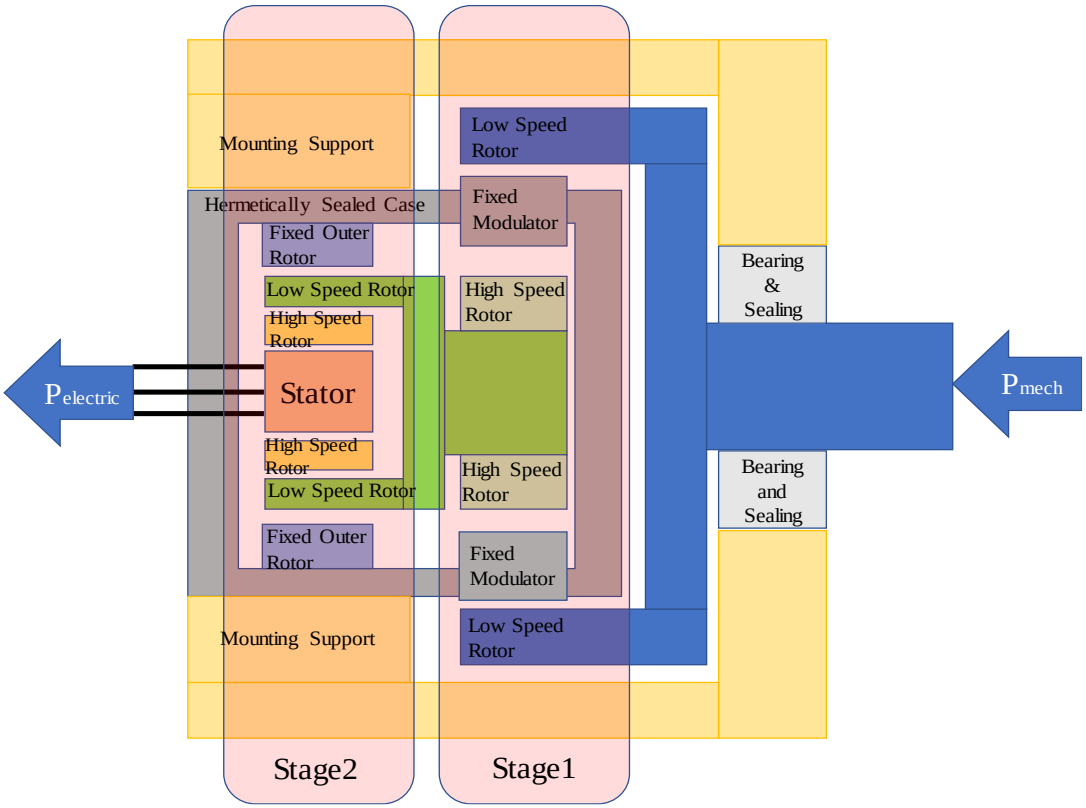

Figure 4-4: Sketch illustrating an approach to designing a hermetically sealed magnetically geared marine hydrokinetic generator (Sizing not to scale) (By Dr. J. Z. Bird).

TABLE 4-6: List of components in contact with water

Component Name	Stage Number
Cage rotor lamination	Stage 1
Cage rotor bars	Stage 1
Cage rotor support rings	Stage 1
Cage rotor endplates	Stage 1
Cage rotor Sealing	Stage 1
Outer rotor rings	Stage 2
Outer rotor endplates	Stage 2
Outer rotor back iron (laminated)	Stage 2
Stator ground-plate	Stator
Stator tube housing	Stator

By using Halbach arrangement, there will no longer be a need for supporting laminations between magnets, although a back iron, preferably laminated for higher performance, is designed to glue the magnets to. Inner gap is 0.5mm and outer gap is 1.5mm, as hermetic sealing will fill a part of the outer gap. For second stage of the HSMGG

design, both inner and outer rotors are Halbach, providing 0.5mm air gap on both sides of the cage rotors. Generator part of this design is a pre-ordered generator which is connected to the MG in series. Schematic 2D view and a 3D model of the first (a and c) and second (b and d) stages of the multi-stage HSMGG are shown in Figure 4-5. The first stage has 6 pole pairs on the inner rotor, 46 modulating pieces on the cage rotor and 40 pole pairs on the outer rotor. These numbers for the second stage are 4, 38 and 34, respectively. More details on the geometric parameters of the multi-stage HSMGG are listed in TABLE 4-7 and TABLE 4-8.

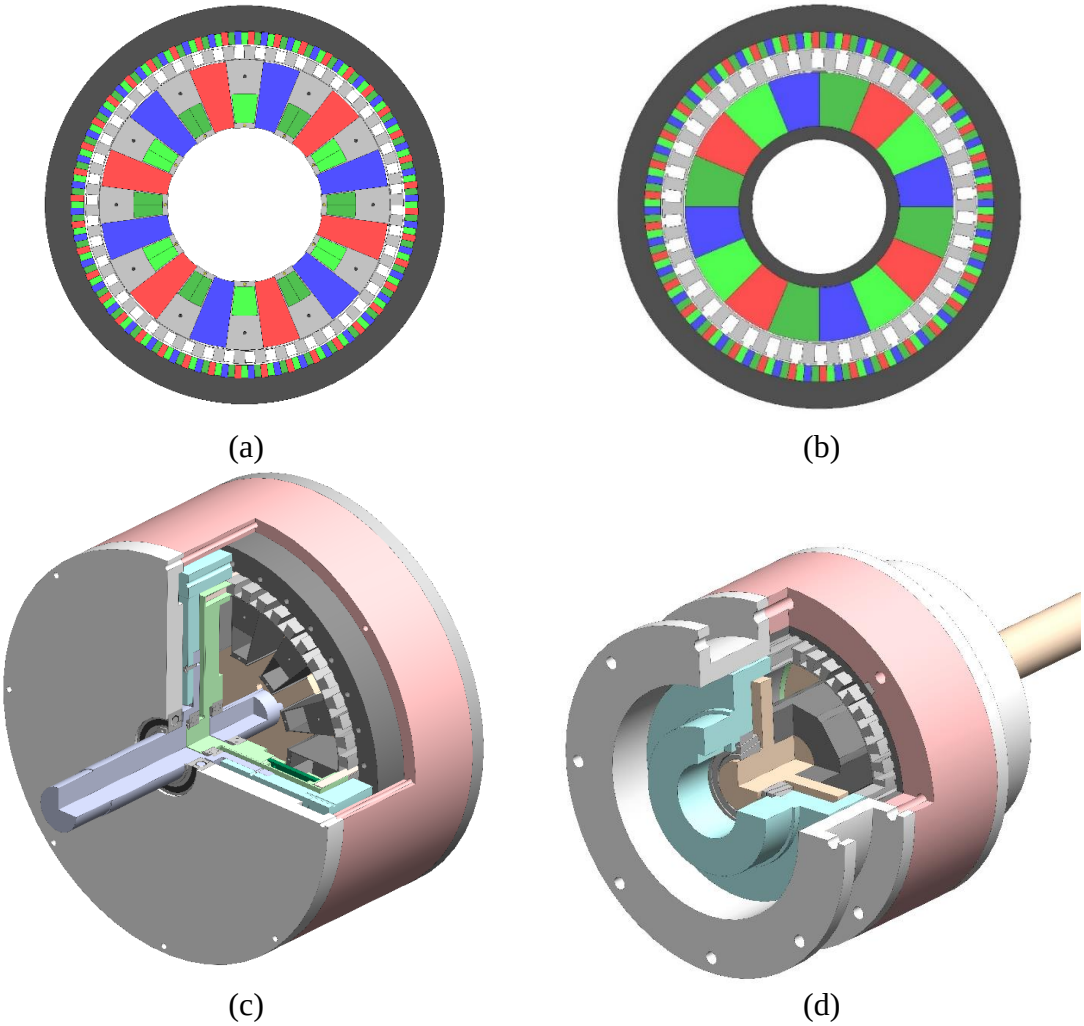

Figure 4-5: Schematic presentation (a & b by Hossein Baninajar) and 3D model (c & d) of the magnetic arrangement for the first and second stages of multi-stage HSMGG.

TABLE 4-7: Details of the geometric properties for the first of the multi-stage HSMGG design.

Description		Final value	Unit
Inner rotor	Inner radius, ri1	73	mm
	Outer radius, ro1	142	mm
	Pole pairs, p1	6	-
	Angular span, θ1	π/(2p1)	radians
Cage rotor	Inner radius, ri2	142.5	mm
	Outer radius, ro2	155.5	mm
	Pole pairs, n2	46	-
	Angular span, θ2	π/p3	radians
Outer rotor	Inner radius, ri3	157	mm
	Outer radius, ro3	195	mm
	Pole pairs, p3	40	-
	Angular span, θ3	π/(2p3)	radians
Axial length, d		50	mm
Gear ratio, G12		6.67	-

TABLE 4-8: Details of the geometric properties for the second of the multi-stage HSMGG design.

Description		Value	Unit
Inner rotor	Inner radius, ri4	27.7	mm
	Outer radius, ro4	50	mm
	Pole pairs, p4	4	-
	Angular span, θ4	π/(2p4)	radians
Cage rotor	Inner radius, ri5	50.5	mm
	Outer radius, ro5	58.5	mm
	Pole pairs, n5	38	-
	Angular span, θ5	π/p6	radians
Outer rotor	Inner radius, ri6	59	mm
	Outer radius, ro6	80	mm
	Pole pairs, p6	34	-
	Angular span, θ6	π/(2p6)	radians
Axial length, d		50	mm
Gear ratio, G45		9.5	-

4.3 LAMINATION STUDY

Laminated structures are commonly employed in magnetic gears based on their ability to focus magnetic flux, while inhibiting eddy currents. Unfortunately, the stiffness of the laminated structure is much lower than a solid piece, which can lead to unacceptable deflections, given the large magnetic forces and small air gaps in magnetic gears. Finite element analysis of laminations to accurately predict these deflections can be computationally expensive due to small elements needed. These analyses also have some uncertainty due to the assignment of bonding stiffness. M. Desvaux, et. al., [119] is one of the few researchers studied the structural behavior of laminated ferromagnetic pieces, analytically. Although, there is no experimental comparison in the mentioned paper. Also, N. Fernando and S. Saha [120] have investigated torsional shear stress on electromagnetic performance of a magnetic gear, in which rotors are laminated and bonded using adhesive. Radial forces and stresses which are the key asset to bending analysis of the components in active region are investigated in [121], although no deflection analysis is reported. Applying the effect of radial forces in an MG, structural optimization of the supporting plates is investigated in [122], [123]. A semi-analytical approach of scaled boundary finite element method is recently used to model the laminated composite plates [124]. The interface layer and the imperfections at the bonding agent is studied in this paper. Searching into the past researches reveals that an accurate computational modeling and validation of the laminated stacks with bonding agents between the layers is missed.

With the aim of investigating the effect of the bonding agent of laminated stacks in an MG on radial stiffness of the system, a small test setup is prepared, as in Figure 4-6. This setup comprises a full set of an inner rotor with 4 pole pairs, free for rotation, and a

single pole of cage rotor laminations, fixed in the position, providing 0.7 mm of air gap before applying the effect of magnetic forces and lamination bending. The axial length of the active region, the region with the magnetic components, is 76.2 mm. A stepper motor, a mechanical gearbox, a coupling, and an electronic level are the other components in this test setup. The laminated stack is also supported circumferentially by a Delrin support. Three various measurement devices are employed to perform a static deflection measurement for the laminated stack, including a TESA height gauge, a CMOS displacement laser measurement sensor, and a coordinate-measuring machine (CMM), as shown in Figure 4-7, with the precision of 0.01 mm, 0.03 mm, and 0.05 mm, respectively.

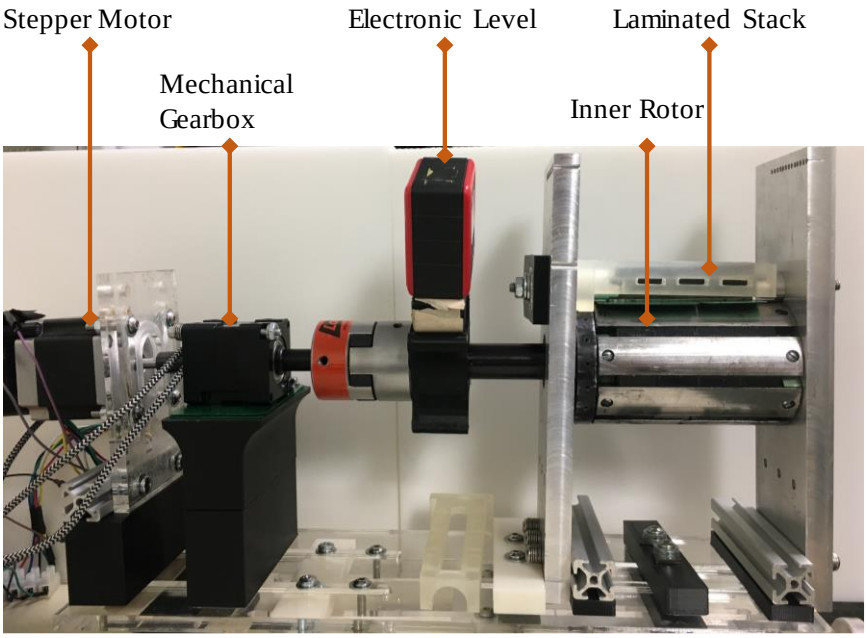

Figure 4-6: Small test setup.

(a) (b) (c)

Figure 4-7: (a) TESA height gauge, (b) CMOS displacement laser measurement sensor, and (c) a coordinate-measuring machine (CMM).

Figure 4-8 shows the schematic 2D and 3D models of the small test setup. Inner rotor magnets are of two different orientations, shown by different colors. Inner rotor metal parts are solid, while the cage stack is laminated. A ¼" rod is passed through the laminated stack to provide radial support. Material properties of the components in the setup are listed in TABLE 4-9. In order to validate the magnetic modeling of the system with the experimental setup, flux density of the inner rotor is measured using a magnetic flux gauge. The sensor of the gauge is 0.1 mm thick, so the flux is experimentally measured with a 0.05mm distance from the surface of the inner rotor. In a 180-degree span, 90 data points are considered, one point very 2 degrees.

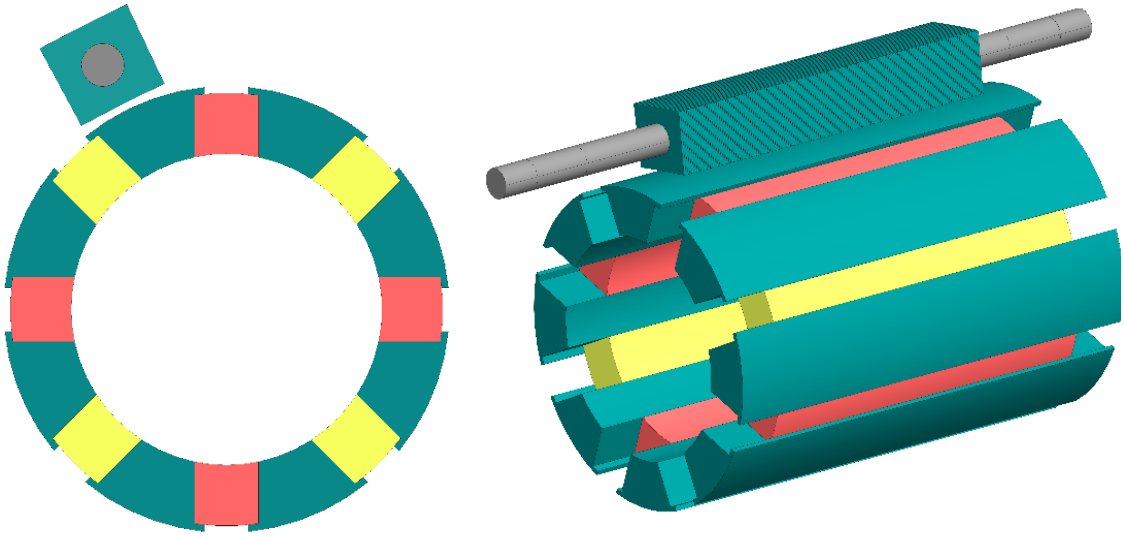

(a) (b)

Figure 4-8: Schematic view of the test setup (a) 2D cross section and (b) 3D isometric view.

TABLE 4-9: Material properties of the components in the setup [125]–[127].

Material	components	Density [kg/m3]	Young's Modulus [GPa]
NdFeB	- Magnets	7600	150
Electrical Steel	- Cage Laminations - Inner Steels	7650	185
Steel	- Rods	7850	200
Aluminum 6061	- Endplates - Supports	2700	68.9

CHAPTER 5: THERMAL DESIGN OF TWO MAGNETIC GEARS

5.1 WIND (OBJECTIVES AND DESIGN DETAILS)

As mentioned before, the presence of a rotary conductive material in a magnetic field leads to the creation of eddy currents which eventually leads to thermal stresses and temperature rise in the system. The high temperature in electro-magnetic systems can result in in geometric thermal distortion, demagnetization of the permanent magnets and negatively affect the bonding agent between the laminations. In order to investigate the temperature-rise in a radial flux focusing magnetic gearbox, a sub-scale version of the radial MG's, fully laminated with 4.25:1 gear ratio is provided. Figure 5-1 shows the schematic view of the magnetic configuration of the system. Similar to the MSMG design, Outer rotor is fixed and cage rotor is the high load/ low speed rotor. 90-degree cut away view of the mechanical design of the system and the assembly steps of the system are shown in Figure 5-2. The geometric specifications of the system are listed in TABLE 5-1.

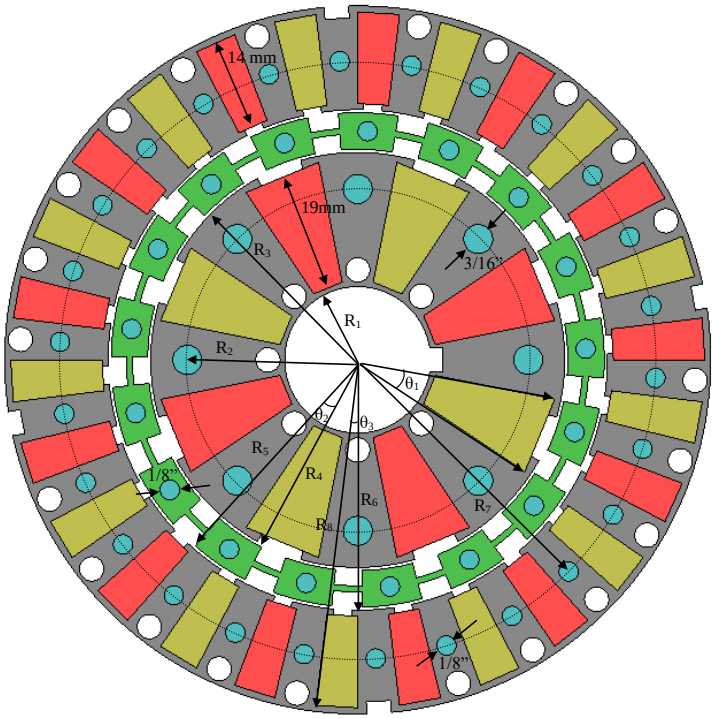

Figure 5-1: Flux focusing fully laminated magnetic gear showing the p1 pole-pairs on the inner rotor, p3 pole-pairs on the outer rotor and n2 ferromagnetic segments on the cage rotor [72].

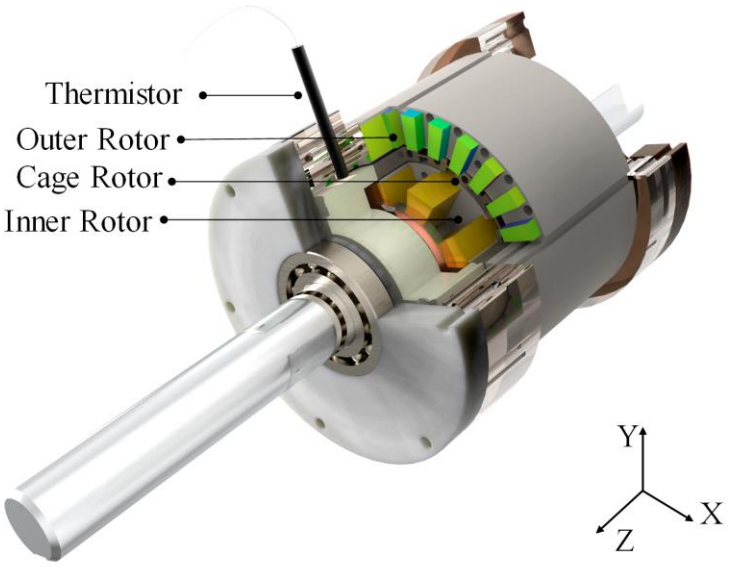

(a)

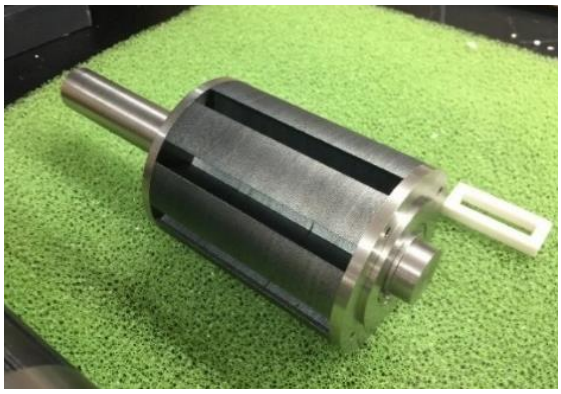

(b)

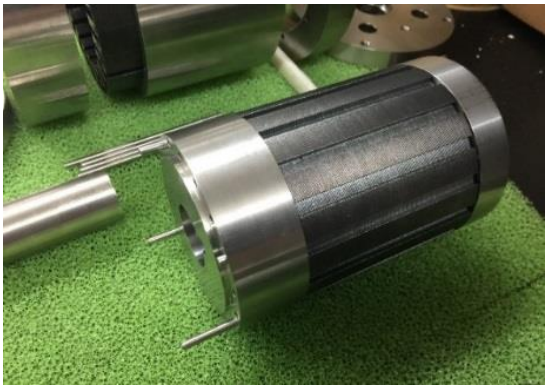

(c)

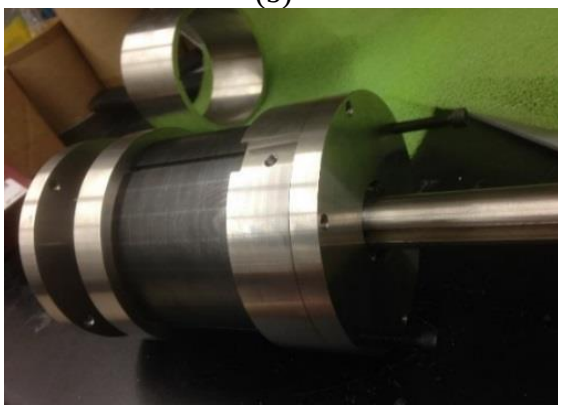

(d)

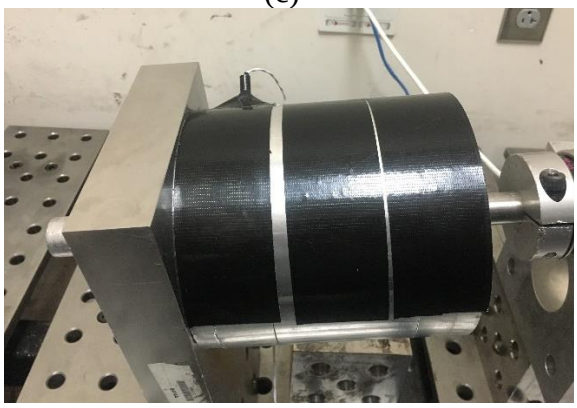

(e)

Figure 5-2: (a) 90-degree cut away of the mechanical design of the subscale laminated magnetic gearbox. Magnetic gear components, including (b) inner rotor, (c) cage rotor, and (d) outer rotor. Fully assembled magnetic gear with thermal probes.

TABLE 5-1: Magnetic gear geometric specification [128].

Rotor	Parameter	Value	Units
Inner rotor	R1	12	mm
	R2	28	mm
	R3	33	mm
	θ1	22.5	degrees
Cage rotor	R4	33.5	mm
	R5	39.5	mm
	θ2	14	degrees
Outer rotor	R6	40	mm
	R7	47	mm
	R8	56	mm
	θ3	π/26	degrees

Provided test setup for testing the thermal behavior of the sub-scale MG is shown in Figure 5-3. Power was supplied by a variable frequency drive, Figure 5-3(c), which is transformed into rotational motion by the AC motor, providing input speed for the magnetic gearbox on the high-speed side of the gearbox. The low speed side of the LMG is disconnected from generator to achieve a no-load situation. A thermistor was used to record the thermal behavior of the magnetic gearbox, every five seconds. A thermal camera is used to measure the surface temperature of the magnetic gearbox. To improve surface measurements, black tape was used to cover the reflective, aluminum surface of the MG, since the thermal camera measures temperature more accurately on non-reflective surfaces.

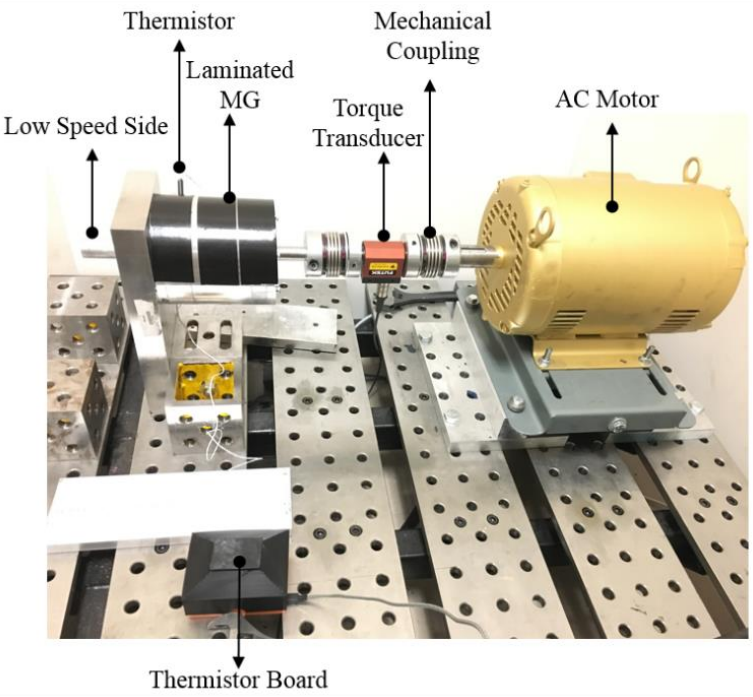

(a)

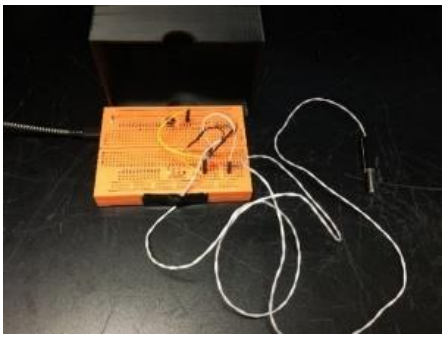

(b)

(c)

Figure 5-3: (a) Experimental setup for thermal analysis of the LFFMG, (b) thermistor circuit board, and (c) variable frequency drive.

The governing equations are solved numerically using finite volume formulation. The computation method employs a second order upwind scheme for convective terms. For the computational domain, there is no inlet or outlet flow, so the solution convergence is greatly dependent on the meshing structure and solution control. The PRESTO algorithm (PREssure Staggering Option) [129] is found suitable for a steep pressure gradient in a rotating flow, so it is applied in ANSYS to handle the pressure-velocity field coupling. The convergence criterion is satisfied when the RMS residuals of the momentum and continuity are less than 1.0 × 10-6 and the energy equation is less than 1.0 × 10-8. The outer rotor surface temperature is also monitored to assure satisfaction of all convergence criteria. There exist two rotating objects in the computational domain with different angular velocities with a ratio of 4.25. As a result, the convergence achieves by defining a gradual speed ratio to the moving objects. If the velocity of moving objects is defined instantaneously on the boundaries, a convergence issue arises because the rotational boundary condition leads to complex forces in the flow, and the calculation becomes unstable. Thus, the simulation initiates with very low angular velocity, and then increases gradually to reach the final desired convergence.

To simplify the CFD model, it is assumed that the sidewalls are thin. Figure 5-4 shows the model used for CFD analysis and the boundary conditions (BC). To reduce the computational time, a symmetric boundary condition applied in the axial (Z) direction is used to divide the system in half. The geometry is intentionally not symmetric in the x and y plane as the number of elements in the three rotors is not divisible into an integer; thus, a full cross section is modeled.

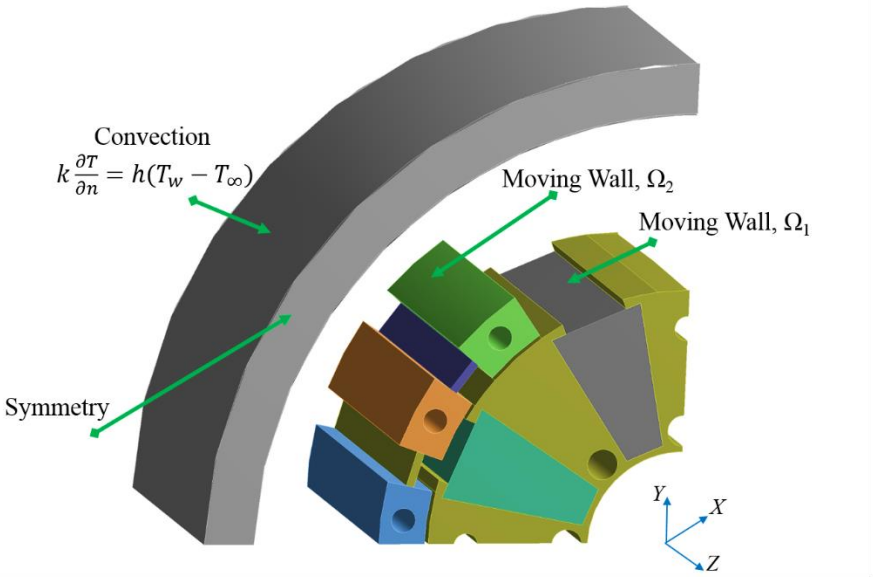

Figure 5-4: The boundary conditions on the CFD model [115]

5.2 MHK (OBJECTIVES AND DESIGN DETAILS)

Analysis of the thermal behavior of the hermetically sealed system is of great importance due to the following reasons:

- The system is a sealed design with no inflow and outflow, which prevents any internal ventilation.
- High temperature may result in demagnetization of the permanent magnets, leading to the lower efficiency and peak torque.

- Thermal stresses may negatively affect the sealing material and defect it.
- This system is also connected to a stator system with winding which also adds up to the losses, and simulating the system thermally helps the designer to decide on the design and material selection.

For this system, the conduction approach is chosen to be used as the system is sealed, with inflow or outflow. Using the conduction approach drops down the load of calculations and the processing time dramatically. Only the active region of the first stage of the HSMGG design is modeled in this simulation. Materials of the sub-components in the system are listed in TABLE 5-2. A geometric model of the first stage is also shown in Figure 5-5. The following conditions are assumed for the system:

- Free convection is considered on all exterior surfaces.
- Conduction approach is used for the air gaps.
- Symmetry condition is considered in axial (Z) direction.
- Parts are supported on one end and other end would have the same boundary conditions due to the symmetry in Z direction.
- Deformation is shown on the symmetry plane, while Stress is shown on the support side.
- Outside temperature is 297.15 [K].

TABLE 5-2: Material Introduction for different components.

Part	Material
Laminations	Electrical Steel
Magnets	NdFeB
Cage Bars	Garolite G10
Inner & Outer Rods	Stainless Steel

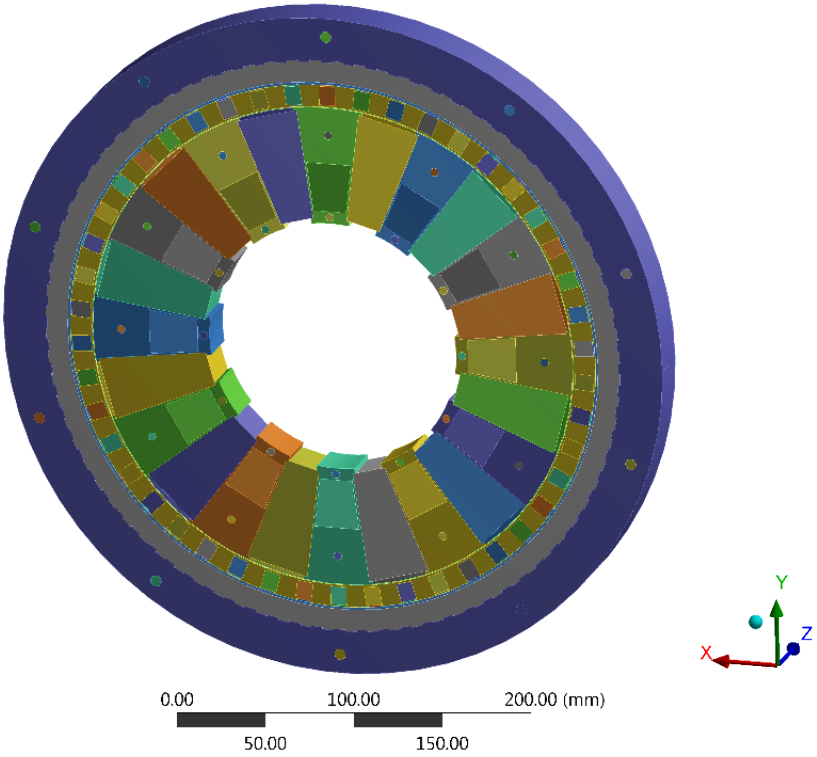

Figure 5-5: Geometric model of the first stage of MHK Subscale design for thermal analysis.

CHAPTER 6: RESULTS

6.1 WIND

6.1.1 Force Calculation

As noted previously, the attractive and repulsive forces between magnetic poles are responsible for the transmission of torque in the gearbox. While only the tangential forces contribute to the torque transmission, the magnets produce significant radial forces as well. These forces calculated based on the material properties of the magnets and the surrounding steel as well as the geometric layout of the magnets and the associated flux focusing and flux modulating components. These details captured in a finite element model, solved using the JMAG software. Plots of the calculated radial and tangential forces on the (a) inner, (b) cage, and (c) outer rotor for the first stage of MSMG shown in Figure 6-1. In this figure, positive values for radial forces indicate outward force and negative values specify inward force. For tangential forces, positive values indicate a counter-clockwise direction of force and negative values specify a clockwise direction of force. Tangential forces are responsible for torque transmission while the radial forces have direct influence on bending of the components in active region lead to reduction of air gap, which could be a critical factor in designing large-scale magnetic gearboxes, knowing that the air gap is in the scale of a few hundreds of micrometers.

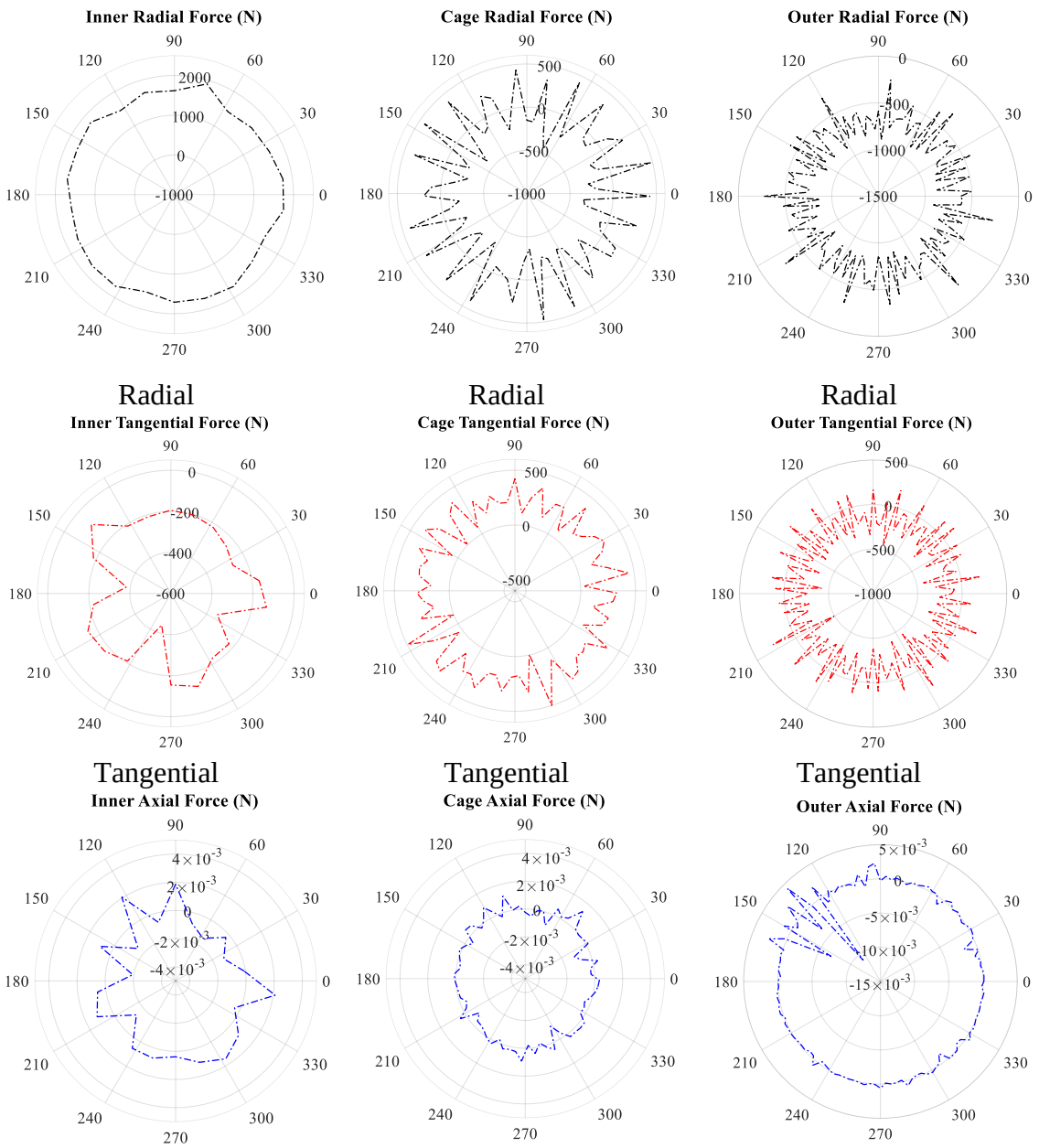

Figure 6-1: Finite element analysis calculated forces applied to the rods passing through (a) the inner rotor, (b) cage rotor, and (c) outer rotor [62].

6.1.2 Structural Analysis

Finite element analysis, using ANSYS software, is the adopted method to predict the deflection of the rods for MSMG stage 1. Inner, cage and outer rotors are separately modeled. In these models, except rods that carry the loads, five rows of laminations and magnets modeled to transfer the interacting forces between the rods. Full modeling of the system is avoided, as the load of calculations is huge. Figure 6-2 shows assembly models of the three rotors of MSMG stage1, cut in half in axial direction due to symmetry. Figure 6-3 shows the maximum deflection of the rods supporting the three rotors in MSMG stage1 design. It represents that maximum deflection of each rotor is slightly less than 0.1mm, which is 20% of the initial air gap, meaning that the air gap will be reduced for double this value. Adding the holes tolerances in endplates, plus axial tilt happens in the endplates; it seems that this design needs serious modifications. Figure 6-4 shows a bent lamination during the assembly process of the initial design of the first stage of the MSMG design.

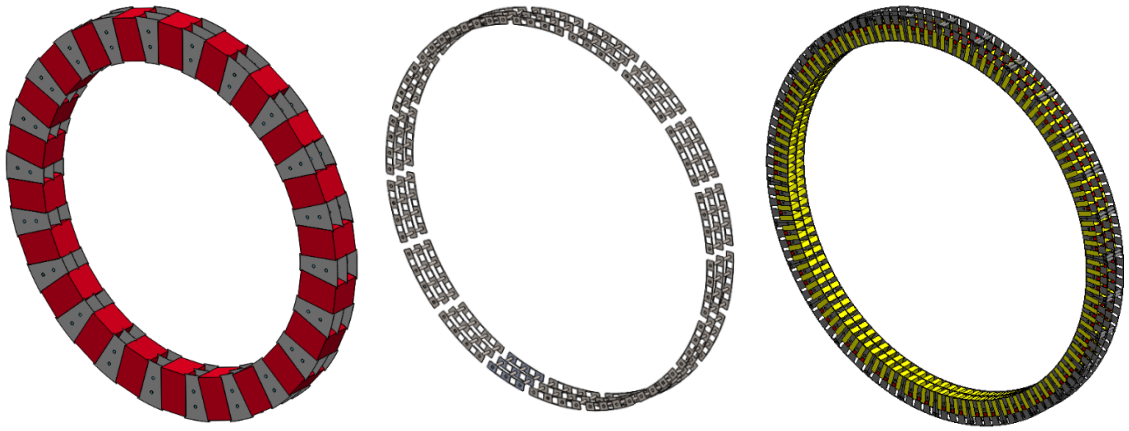

(a) (b) (c)

Figure 6-2: Assembly models of the (a) Inner, (b) cage, and (c) outer rotors of the MSMG stage 1, cut in half in axial direction due to symmetry.

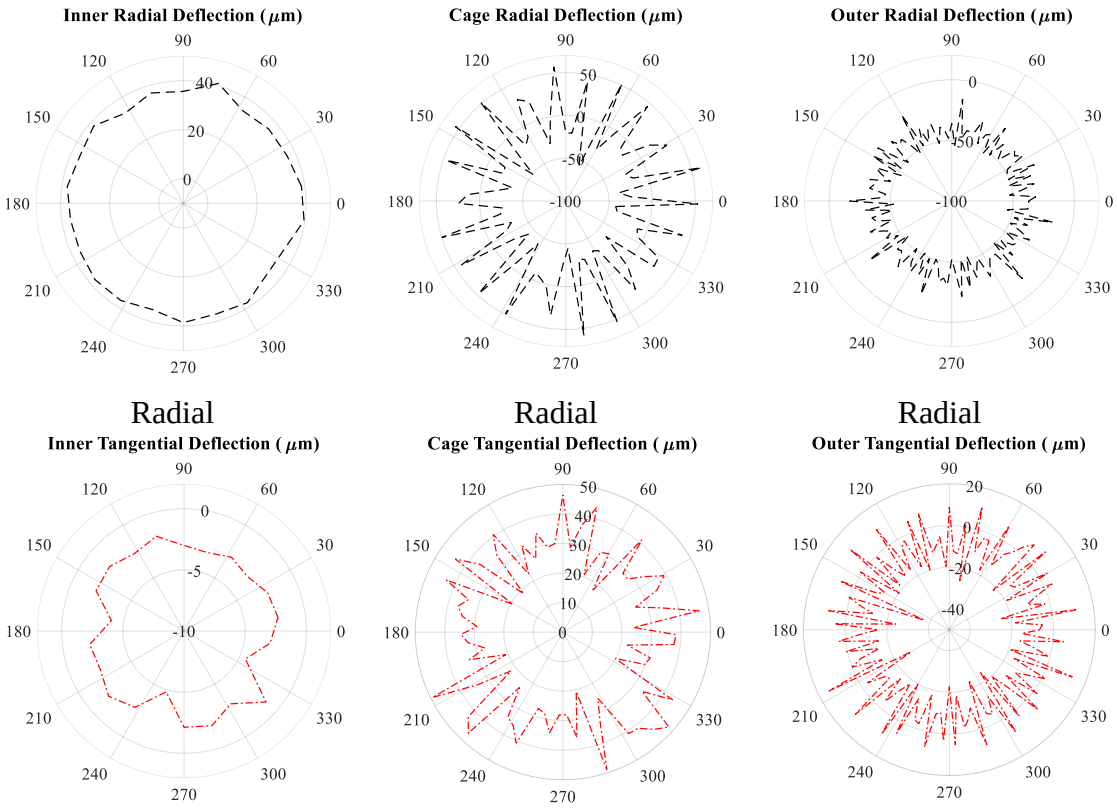

Figure 6-3: Maximum deflection of the rods supporting the (a) inner, (b) cage, and (c) outer rotors in MSMG stage1 design.

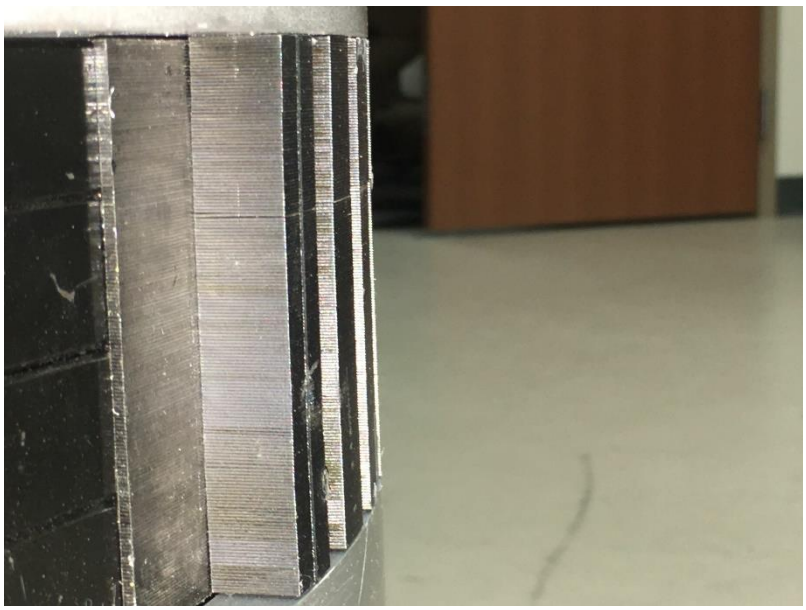

Figure 6-4: A bent lamination during the assembly process of the initial design of the first stage of the MSMG design.

Three options are proposed to address the problem of high- bending deflection in MSMG stage1. First option is to increase the size of rods. Figure 6-5 shows a comparison between losses of cage rotor and rods deflection for the various diameters of the cage rods in MSMG design (stage 1). Based on this graph, it is inferred that increasing the rods diameter results in the lower deflection, but it increases the losses of cage rotor to the high orders. Therefore, a compromise between the supporting elements' geometric and material properties, and magnetic losses should be settled to achieve the highest feasible performance. For this design, 5.7mm is the optimum value for the cage rods diameter. In addition, according to Figure 6-6, torque density of the system is decreased once the size of the rods support iron pieces of the active region is increased. With the same trajectory, efficiency of the system is decreased from 82% to 55% when diameter of the rods increases from 4.2mm to 10mm. According to the interpretation of the two graphs, increasing the size of steel rods passing through iron pieces in active region has considerably negative influence on the performance of the system.

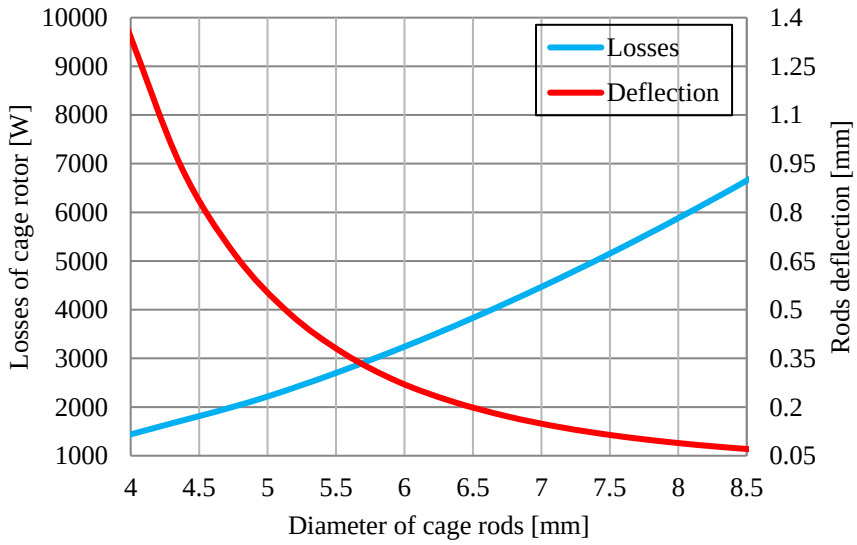

Figure 6-5: Trade-off between losses in the cage rotor and rods deflection for the various diameters of the cage rods. The current cage rotor uses 4.2mm diameter rods

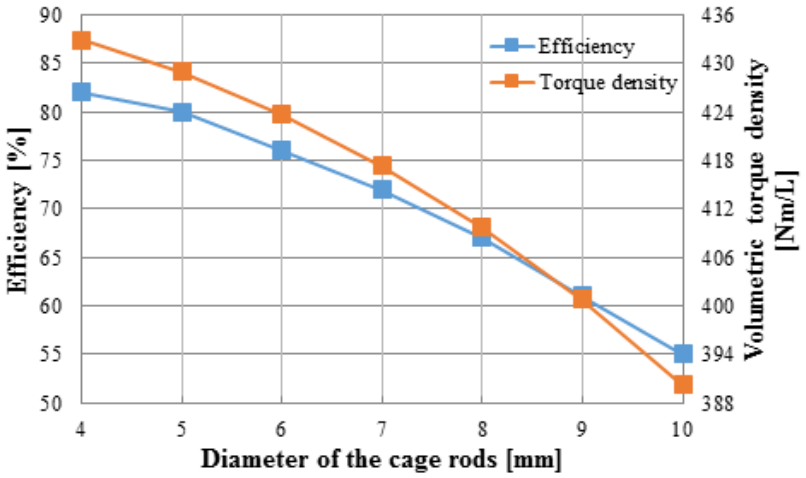

Figure 6-6: Effect of increasing rod size for cage rotor on efficiency and volumetric torque density (By Kang Li, PhD).

Second option is to take advantage of the support rings inside the active region. In order to increase stiffness of the system to prevent bending problems in the central span of the lamination stacks, they are divided into 4 segments to add support rings shown in Figure 6-7. These non-magnetic rings are designed to provide unity and stiffness to the laminated area. In order to investigate the influence of the support rings on the system's stiffness, finite element models of the three rotors with the support rings are provided and the deflection is computed. Figure 6-8 shows a comparison of the rod deflections with and without support rings. As shown in this figure, support rings dramatically decrease the deflection of the supporting rods in the magnetic gears.

Figure 6-7: Inner, cage and outer support rings for MSMG stage1 design [130].

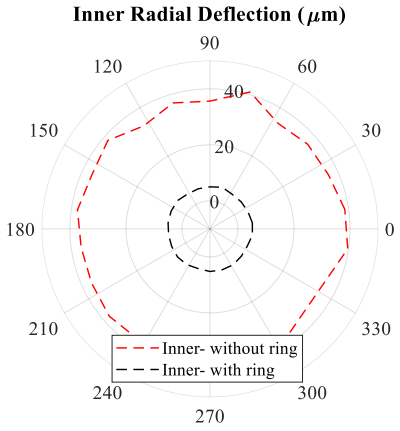

(a)

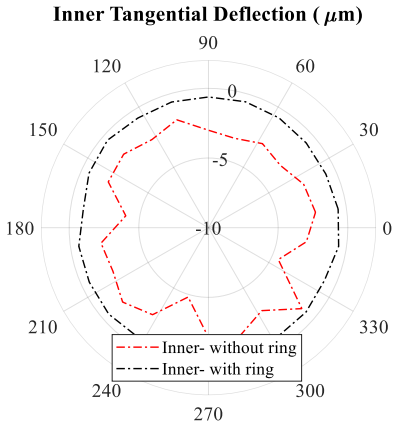

(b)

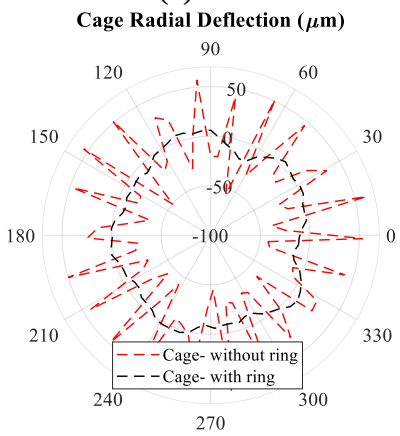

(c)

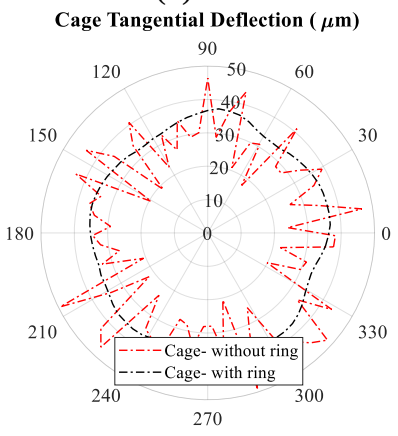

(d)

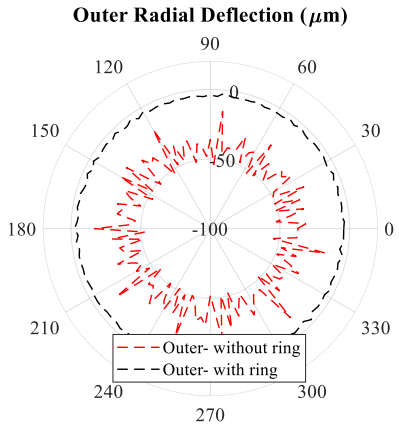

(e)

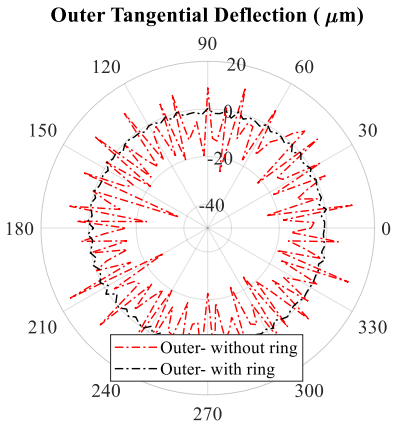

(f)

Figure 6-8: Radial and Tangential deflection comparison for the (a, b) inner, (c, d) cage and (e, f) outer rotors with and without support rings.

Third option for compensating the rods deflection in active region is to increase the radial air gap between the three rotors. Figure 6-9 shows a comparison between the peak torque values for 0.5mm and 1.0mm air gap in MSMG stage1. According to the torque values listed, although using support rings reduces peak torque for about 1.63 kNm, it is still a better approach in comparison with the performance of the system with increased air gap, which is responsible for almost 37% of peak torque reduction.

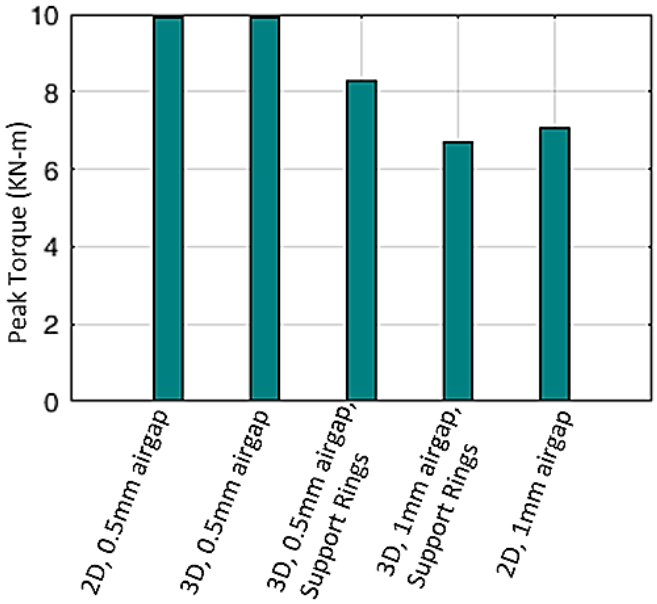

Figure 6-9: Calculated active region torque density [131].

6.1.3 Loss Calculations

Having large conductive materials close to the active region without insulation makes a major contribution in eddy current losses in magnetic gears. The main conductive materials used in this design, which lead to levelized losses in MG, are the steel supporting rods passing through laminated stacks of inner, cage and outer rotors, as well as the aluminum endplates touching active region components. It worth mentioning that aluminum plates will be a great concern for large magnetic gears in which axial length of the active region is fairly small in comparison with aluminum endplate size. Common approaches to avoid eddy current loss issue are (1) applying insulation between conductive support materials and the laminations, and (2) altering material of support components to non-conductive options.

Losses in magnetic gears transform into temperature rise in various positions in the active region. Figure 6-10 shows the loss distribution in various components of the

Laminated MG design, for the five different input speeds on the high torque side of the MG. On each rotor, magnets (for inner and outer rotors) and steel rods are the main sources of eddy current losses. Losses on the rods are much higher than the magnets. Note that cage rotor has the highest rate of eddy current losses in comparison with other components in the active region. The unit for these values is W/L; although inner and outer rotors have much lower volumetric eddy current losses, their larger volume makes them relatively considerable when calculating overall losses. It should be mentioned that lamination stacks have a negligible rate of losses compared to the rods and magnets. Losses from the cage rods are dominant. A curve is fitted with a second-degree polynomial equation to investigate the trend on Eddy Current loss growth, as seen in Figure 6-10(b).

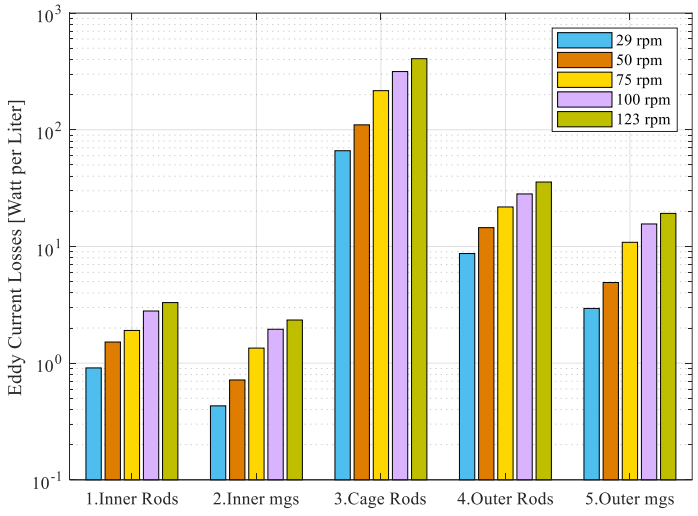

(a)

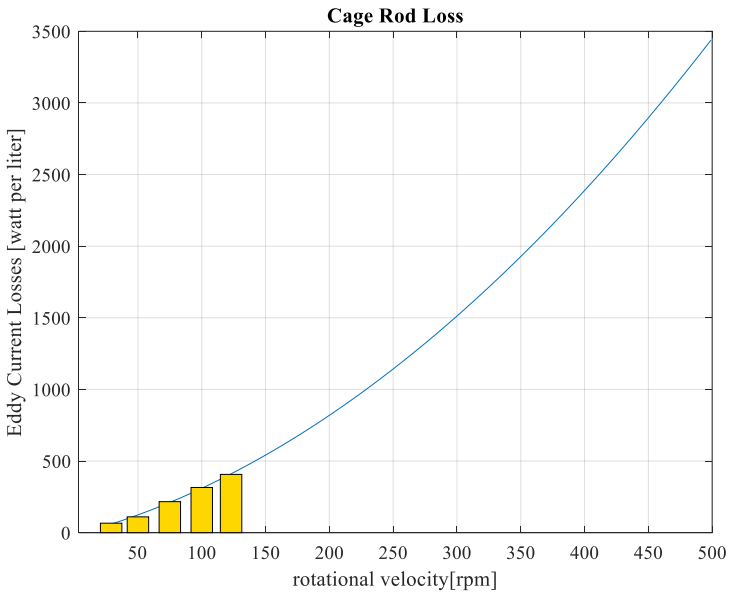

(b)

Figure 6-10: Eddy current losses distributed on (a) inner and outer and (b) cage rotor components of the LMG, and curve fitted trend

6.1.4 Experimental Measurements

A long duration test is performed for five different low speed-side (input) rotational velocities, including 29, 50, 75, 100, and 123 RPM to measure the peak temperature of the system. The average running time for the system was 6 hours. Then, the system turned off to return to the ambient temperature. Figure 6-11 shows the filtered results from the experimental measurements of the temperature rise for the LMG design for three working speeds. The thermistor tolerance is +/-0.1 C. The peak temperature for 29, 50, 75, 100 and 123 RPM input speed is 302.0 [K], 304.2 [K], 309.4 [K], 312.7 [K], and 317.4 [K], respectively. It should be mentioned that the experimental data are low pass filtered. Figure 6-12 also presents a closer look into the experimental result of temperature measurement of the LMG design for 50 RPM input speed, with the thermistor and thermal camera. Changes of the surface temperature are clearly observed as the air gap temperature

increases. Using a non-contact, infrared thermometer with 0.1 C resolution, the surface temperature is also measured to compare with the thermal modeling results. For the aforementioned rotational speeds, temperatures on the surface of where the thermistor is located are 300.6 [K], 302.9 [K], 307.8 [K], 310.9 [K], and 315.5 [K], respectively. Across all the five testing velocities, a temperature difference of ~1.5 C is observed between the surface temperature (by laser infrared thermometer) and outer air gap temperature (by thermistor).

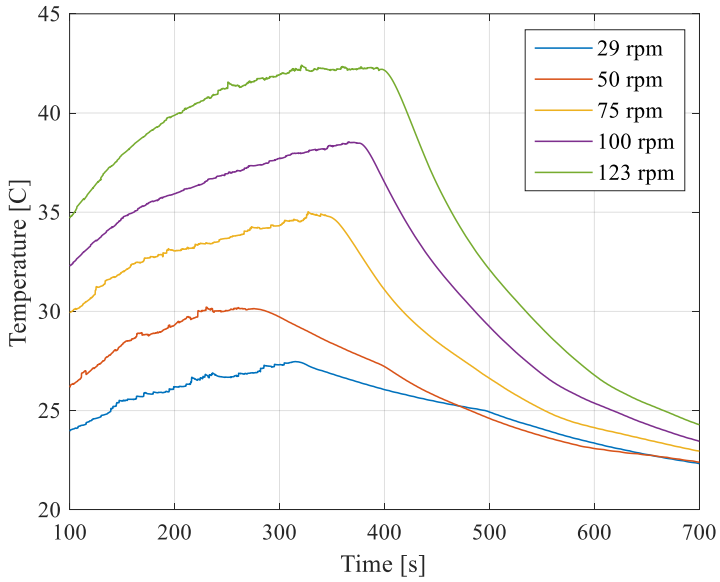

Figure 6-11: Long duration experimental measurement of the temperature changes in the LMG design (+/- 0.1 C).

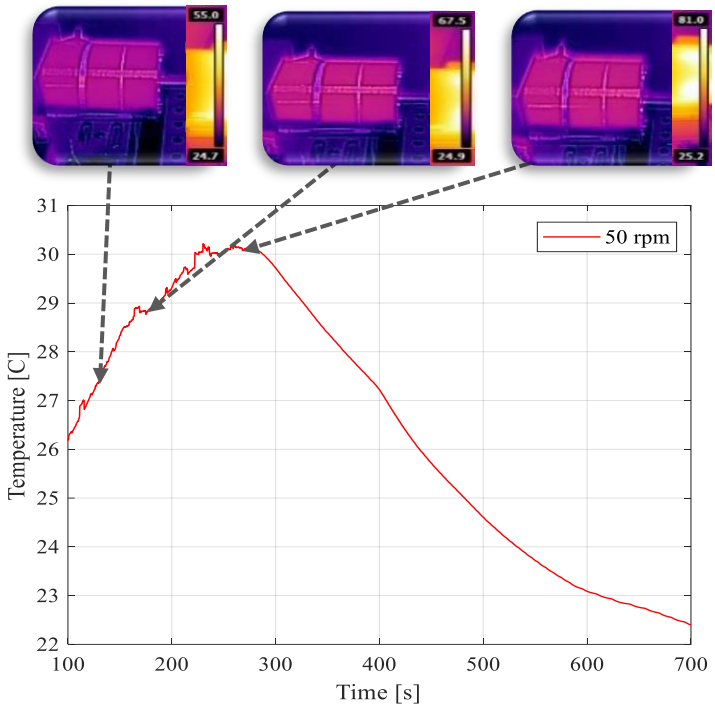

Figure 6-12: Thermistor and thermal camera temperature measurement of LMG design for 50 rpm low speed- side rotational velocity (+/- 0.1 C).

6.1.5 Thermal Analysis and Validation

6.1.5.1 Velocity Validation

The velocity distribution obtained from CFD analysis in the air gap between the inner rotor and the cage is compared with analytical solution. To derive the velocity profile, the Navier-Stokes (NS) equations are solved in the cylindrical coordinate system. The NS equations are simplified based on the problem physics and solved for specific boundary conditions [132]. The gap between the inner rotor and cage is small enough to assume the Couette flow is created. The surface proximity of aforementioned objects creates a viscous flow. The radial velocity component is small compared to the tangential component because the rotational velocity is comparatively small. The effect of the radial velocity on

the resultant velocity is negligible and Allows the NS equation to be simplified. Figure 6-13 shows the schematic of flow in the annulus in a cylindrical system. Because the laminar flow is dominant in the air gap, the rotating Couette flow approach can be used.

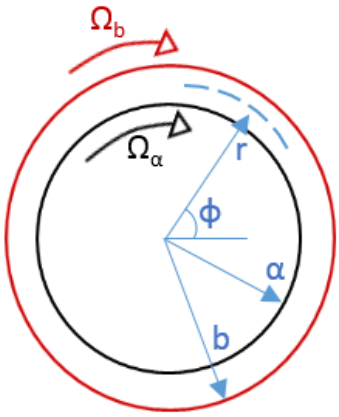

Figure 6-13: Schematic of rotating coquette flow.

For the fluid flow confided between two concentric cylinders with any arbitrary rotational direction and no radial or axial velocity under steady-state condition, continuity and Naiver Stokes' equations are reduced to the equations (6.1) to (6.4) [133].

$$\frac{\partial u_\theta}{\partial \theta} = 0 \tag{6.1}$$

$$-\frac{\rho u_\theta^2}{r} = -\frac{dp}{dr} \tag{6.2}$$

$$-\frac{d^2 u_\theta}{dr^2} + \frac{1}{r}\frac{du_\theta}{dr} - \frac{u_\theta}{r^2} = 0 \tag{6.3}$$

$$\frac{d^2 u_\theta}{dr^2} + \frac{d}{dr}\left(\frac{u_\theta}{r}\right) = 0 \tag{6.4}$$

The equations are solved with appropriate boundary conditions as follows:

$$@\mathrm{r} = a, \mathrm{u}_\theta = a \times \Omega$$
$$@\mathrm{r} = b, \mathrm{u}_\theta = b \times \Omega \qquad \text{(6.5 a\&b)}$$

Equation (6.4) is an ordinary differential equation and is solved in standard form.

$$u_\theta = C_1 r + \frac{C_2}{r} \qquad (6.6)$$

Where C1 and C2 are constant and given by:

$$C_1 = \frac{\Omega_b b^2 - \Omega_a a^2}{b^2 - a^2} \qquad (6.7a)$$

$$C_2 = \frac{(\Omega_a - \Omega_b) a^2 b^2}{b^2 - a^2} \qquad (6.7b)$$

The tangential velocity distribution obtained from equation (6.6) at any radial location. It is shown that the equation (6.7) is independent of fluid transport properties in the steady-state flow. The velocity profile is obtained analytically in the gap between the inner rotor and the outer rotor where the gap size is 0.5 mm (b-a=0.5 mm) over a range of rotational velocities and compared to the predicted values from numerical analysis. Figure 6-14 illustrates the calculated and measured velocity in the gap between the inner rotor and the cage rotor. It is clearly observed that the predicted velocity values are in excellent agreement with the exact solution.

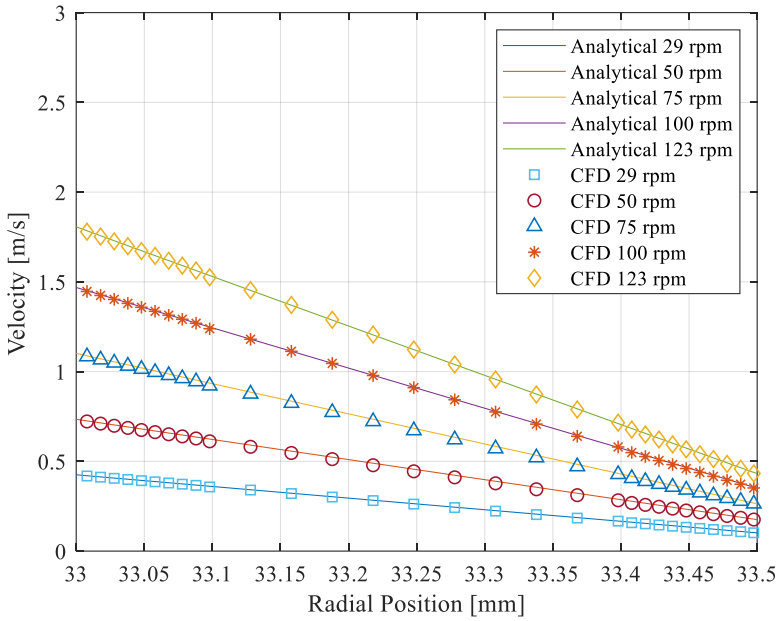

Figure 6-14: CFD and Numerical velocity profiles over the rotational velocities.

6.1.5.2 Temperature Verification of the Numerical Approach

Experimental measurement is used to verify temperatures predicted by the CFD model of the magnetic subscale gearbox. Air gap and surface temperatures measured and compared to the calculated temperatures over a range of rotational velocities. As shown in Figure 6-15, the measured and CFD results are well within agreement. The air gap and Surface temperatures increase linearly with rotational velocity. The measured and calculated surface temperatures are verified with a small error for low rotational velocities. However, for higher values of rotational velocity, a variation between the measured and calculated temperature is observed. For low Reynolds number (low speeds), the predicted results showing an error of 0.5% and for high Reynolds numbers (high speeds), CFD results exhibit around 2% error in general. Parameters used in conduction and coupled conduction-convection approaches for the outer air gap listed in TABLE 6-1.

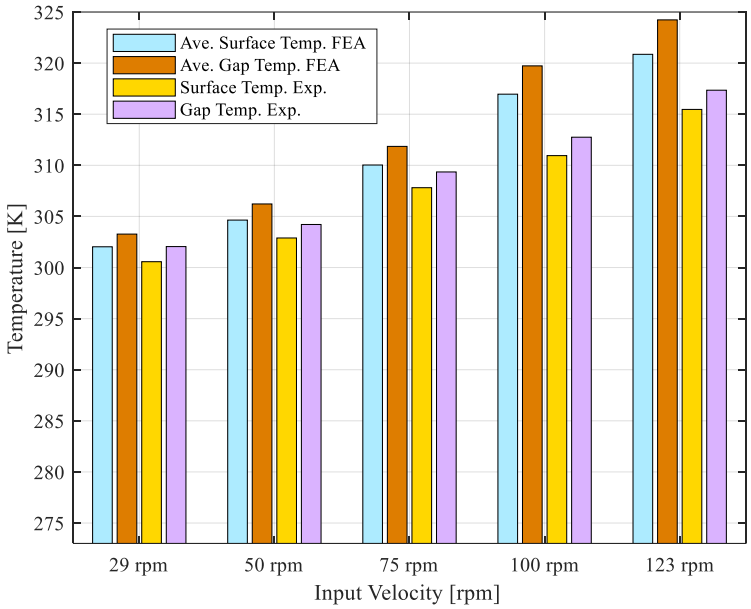

Figure 6-15: Calculated and measured temperature on the outer surface and air gap over a range of rotational velocity [134].

TABLE 6-1: Parameters used for modeling the inner and outer gap

Outer Gap					
	Coupled method				Cond. Method
ω (rad/s)	Re	T (K)	Pr	h (W/m2.K)	K (W/m.K)
29	40	303	0.677	43.12	0.026
50	65	306	0.671	42.73	0.0268
75	100	311	0.662	42.20	0.0273
100	135	319	0.647	40.04	0.0277
123	165	322	0.642	39.79	0.028
Inner Gap					
	Coupled Method				Cond. Method
ω (rad/s)	Re	T (K)	P	h (W/m2.K)	K (W/m.K)
29	40	304	0.693	40.25	0.0260
50	65	307	0.669	45.43	0.0269
75	100	312	0.659	46.77	0.0273
100	135	321	0.645	46.48	0.0279
123	165	326	0.643	46.08	0.0280

TABLE 6-2 and TABLE 6-3 show the simulation results and measured data on the outer surface and in the outer air gap with corresponding error, Over the range of 29-123 RPM, with mere conduction approach and coupled conduction- convection approach, respectively. The difference between the calculated and measured temperature for the air gap and outer surface might be partially due to calibration and measurement errors, considering the thermo-physical properties independent of temperature, and estimated thermal convection coefficient for the lab environment; additionally, the estimation error of the fluid properties with a single value of equivalent thermal conductivity to the aforementioned items.

TABLE 6-2: Calculated and Measured Temperature at Different Angular Speeds when using both Conduction and Convection.

Parameter		Values					Units
Angular speed, ωin		29	50	75	100	123	RPM
Reynolds number, Re		40	65	100	135	165	-
Outer surface temperature	Measured	300.6	302.9	307.8	311.0	315.5	K
	Calculated	302.0	304.6	310.0	317.0	320.9	K
	Error	0.46	0.56	0.71	1.89	1.68	%
Outer air gap temperature	Measured	302.0	304.2	309.3	312.7	317.3	K
	Calculated	303.3	306.2	311.9	319.7	324.2	K
	Error	0.42	0.65	0.80	2.18	2.15	%

TABLE 6-3: Calculated and Measured Temperature at Different Angular Speeds when only using Conduction

Parameter		Values					Units
Angular speed, ωin		29	50	75	100	123	RPM
Reynolds number, Re		40	65	100	135	165	-
Outer surface temperature	Measured	300.6	302.9	307.8	311.0	315.5	K
	Calculated	303.7	305.9	314.0	319.1	321.8	K
	Error	1.02	0.98	1.97	2.54	1.96	%
Outer air gap temperature	Measured	302.0	304.2	309.3	312.7	317.3	K
	Calculated	304.1	306.3	315.1	320.8	324.0	K
	Error	0.69	0.68	1.84	2.52	2.06	%

6.1.5.3 Thermal Stress and Deformation Analysis

Temperature rise in an MG influences the structure of the system through thermal stresses and deformations associated with it. The finite element method is used to formulate and predict structural response to the thermal analysis results, [135]. For this setup, magnets, steel rods and outer rotor sleeve are solid parts, while the laminations are modeled as layers of 0.5mm thickness, connected to each other through "bonded" contact type, with contact stiffness of 1.25×10-4 (unit-less) defined in ANSYS software [55]. The rotors are fixed on the rod area on both ends, but the laminations and magnets are restricted from moving in axial direction using displacement boundary condition.

Figure 6-16 (a) and (b) show the thermal stresses and corresponding deformations resulting from the temperature rise in the MG at ω2=50 rpm rotational velocity. Laminations and magnets are fixed on both ends (in the axial direction). Note the centrifugal effect and bending forces caused by the magnetic fields are not included in the study. In order to investigate the stresses in more detail, the maximum deflection at the six radial passes are shown in Figure 6-17. These paths were selected that are on the sides of the gearbox where the highest stresses are expected.

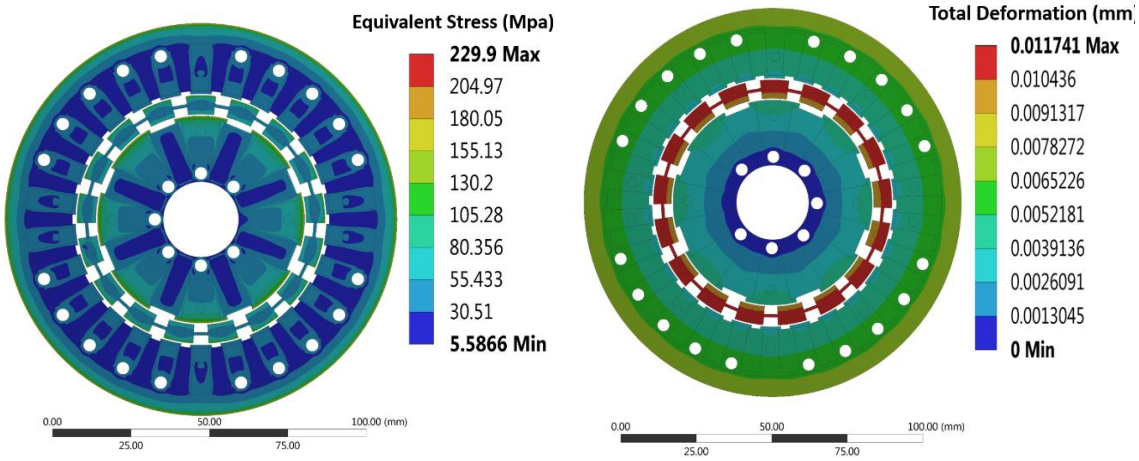

(a) (b)

Figure 6-16: (a) Equivalent thermal stress analysis and (b) total thermal deformation of the LFFMG design at the 50 rpm input rotational velocity

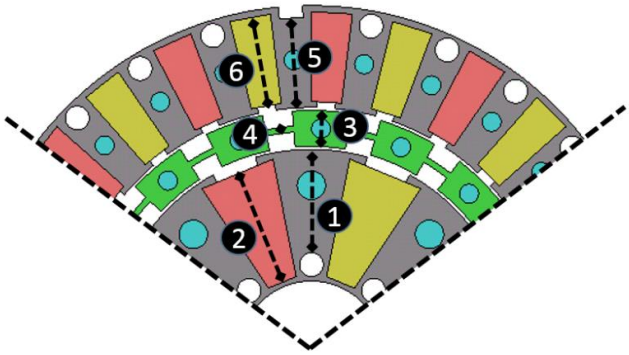

Figure 6-17: Graphical display of the paths selected on the three rotors with the purpose of investigating thermally caused stress and deformation

Deflection analysis results intersected with loss values are presented in Figure 6-18 for the rotational velocities starting from 29 rpm to 500 rpm. The deformation is of a second order relationship with the rotational velocity. As expected, the cage rotor square and bridge sections experience the highest thermally caused deformations, seen in Figure 19. For the inner rotor laminations and magnets, despite the high values of thermal stresses, much lower deformation is resulted due to the greater number of supporting components on the inner rotor compared to the other two rotors. The structural results suggest that for

the scaled-up designs of the MG's or for the systems with higher operational speed, there is a need for changing the material of the support structures, in this case the rods, to non-conductive materials, such as Garolite or Delrin, in order to mitigate the level of eddy current losses in the system in the first place. High temperatures and eventually high deflection in the system not only results in demagnetization of the magnets, but also it might lead to the closed air gap and system failure. In addition, a revision on the cage laminations might be effective to come up with the design with higher stiffness.

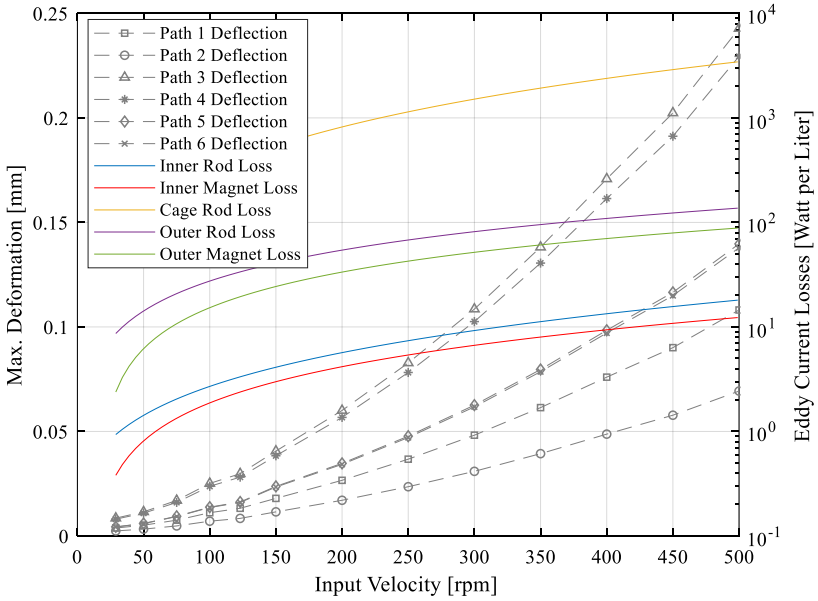

Figure 6-18: Maximum thermally caused deformations for the six paths specified on the three rotors, for low speed shaft rotational velocities starting from 29 rpm to 500 rpm, intersected with loss values in different components [134].

6.1.6 Final Design of the MSMG Model

After performing magnetic field analysis and extracting forces, torques, magnetic flux leakage and eddy current losses, which were used to run performance, structural, thermal, material, and dynamic analysis, final designs are decided. After observing the

deflection results of the first stage of the MSMG design, re-structuring and re-designing the laminations for the rotors may be necessary. For this purpose, several geometries are proposed and compared based on the peak torque and structural supports that they provide. Figure 6-19 shows the initial and final laminations ordered for the design.

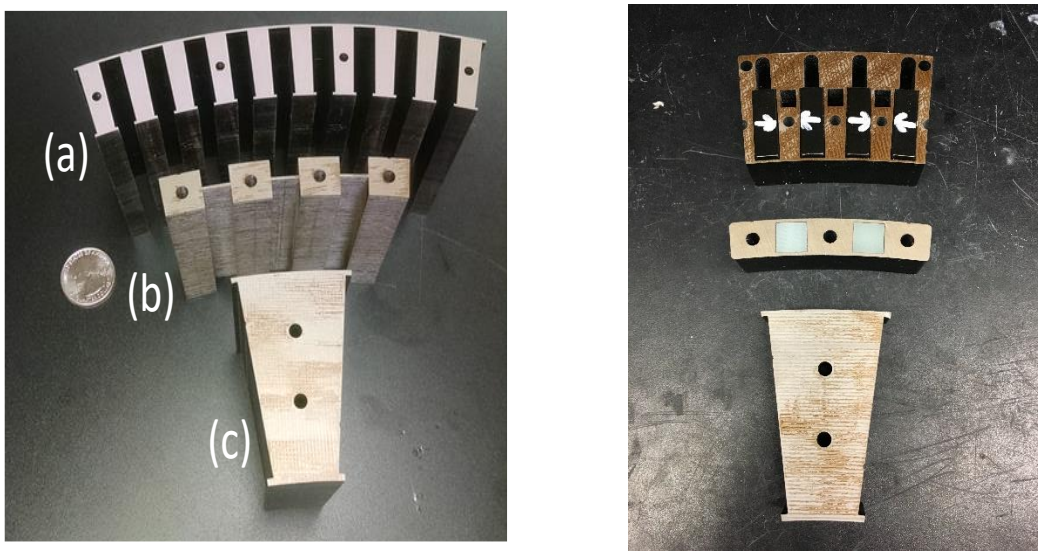

(a) (b)

Figure 6-19: (a) Initial and (b) final lamination designs of the first stage in the MSMG design.

Unlike many of the previous designs, as [136] and [50], the endplates in this design have multiple cutouts as in Figure 6-20. These cutouts are designed so that the overall stiffness of the plates does not degrade. In addition to this, the cutouts not only decrease the weight of the plates, but also help to properly ventilate the system by introducing forced convection, in turn decreasing the average temperature. Figure 6-21 shows the final ordered laminations for the second stage of the MSMG design. The endplates are also with cutouts in the second stage.

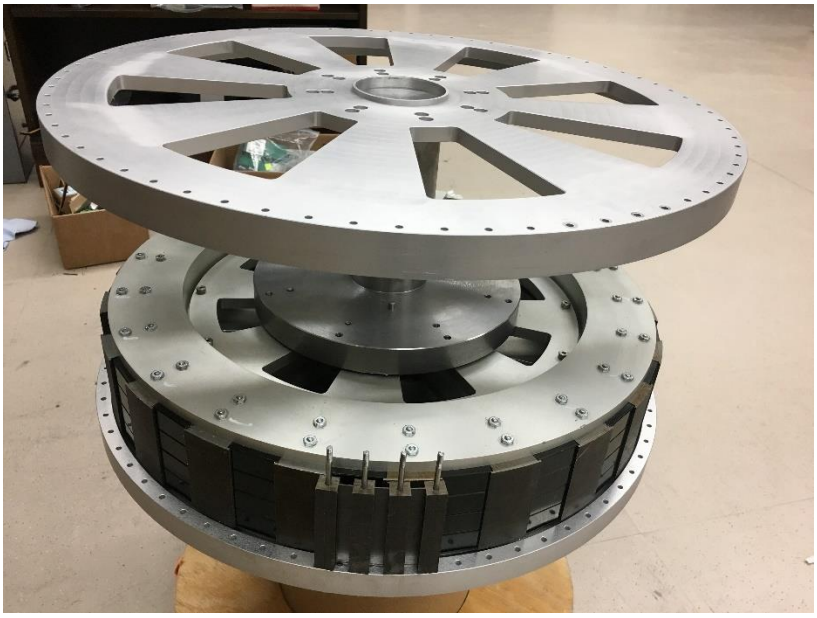

Figure 6-20: Endplates of the first stage of the MSMG design with cutouts (inner and cage endplates are shown).

Figure 6-21: Final ordered laminations for the second stage of the MSMG design.

Figure 6-22 shows the final designs of the magnetic configuration of the MSMG design. In the MSMG stage1, cage lamination design is changed to a “double-bridge”

configuration, air gaps is doubled to 1mm, and steel rods are responsible for providing radial and tangential supports. In MSMG stage2, cage rotor is also double bridge and air gaps are 1mm, supports are steel rods, but for the outer rotor, the design is changed to have the supports on the outer radii. It may be noted that the cage and outer rotors are not single pieces, but are instead split into 4-pole sections. This is due to limitations during the manufacturing process, as the laminations cannot be cut as a singular part due to their large size. The 3D model of the full setup with 90-degree cutaway is shown in Figure 6-23. The installation of the support rings in the first stage can be seen in this figure.

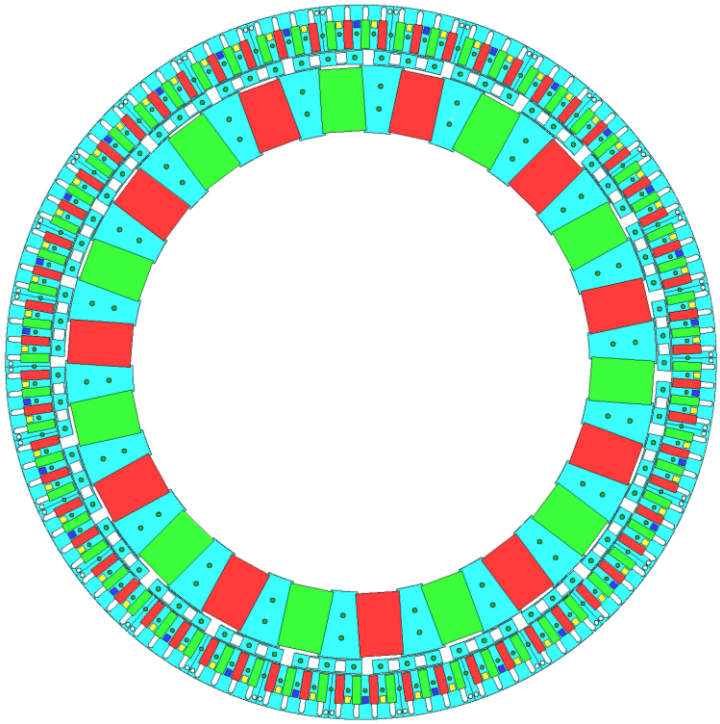

(a)

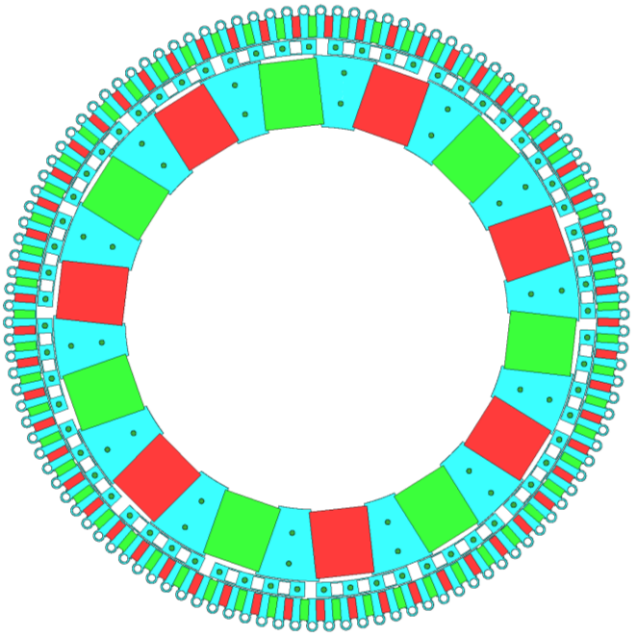

(b)

Figure 6-22: final designs of the magnetic configuration of the MSMG design (a) stage1 and (b) stage2.

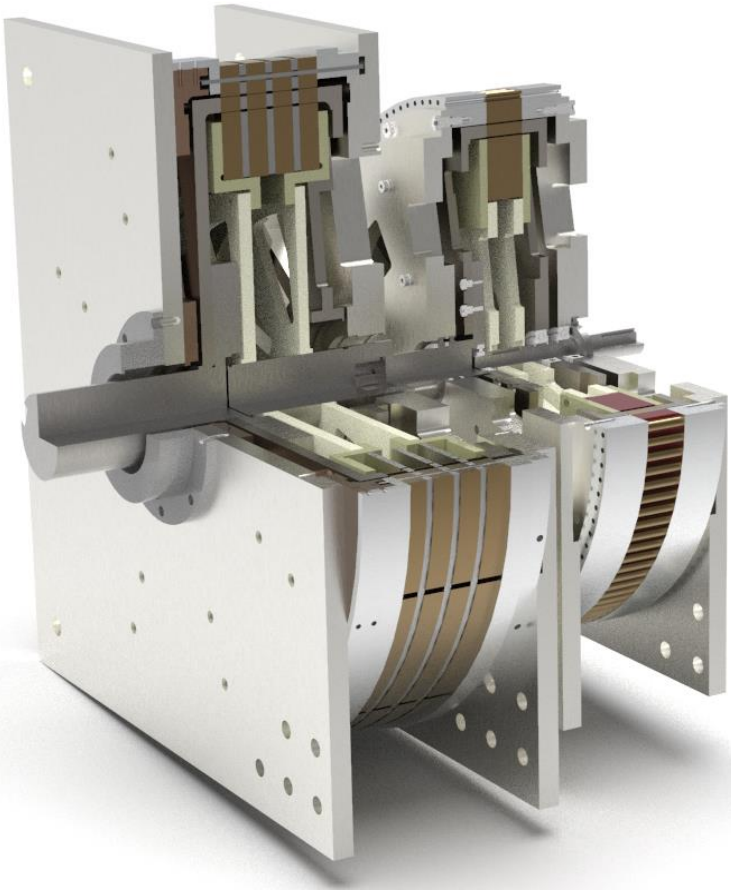

Figure 6-23: 90-degree cutaway view of the final assembly of the MSMG design.

Figure 6-24 shows the full assembly of the of the first stage connected to the torque transducer, a mechanical gearbox (11:1 Sumitomo mechanical gearbox) and an aluminum bar for the static torque measurement. Figure 6-25 shows the torque measurement results versus the 3D FEA calculated values for the first stage of the MSMG design. The measured peak torque is T_{peak}=4.25 kN.m, which is about 11.3% lower than the 3D FEA calculated value. The probable reasons are mentioned as "the lamination stacking factor, tolerance discrepancies in the actual experimental air gap and B-H curve material inaccuracies at the very high saturation levels" [69]. A measurement has been conducted on the efficiency and the percentage of power loss in this design for different load conditions, reported in Figure 6-26. The input speed in these measurements is 5RPM. It is evident that the power loss does not considerably change with the changes of the load, less than 20% of changes, while the efficiency dramatically changes form 40% for the 10% load condition to 90% for the full-load condition. In this design, the peak torque is recorded as 4.79 kN.m, resulting in the active volumetric and mass torque density of 141 N.m/L and 40 N.m/kg, respectively. The considerably low torque density is related to the 3D edge effect and increased losses that were not considered in the design.

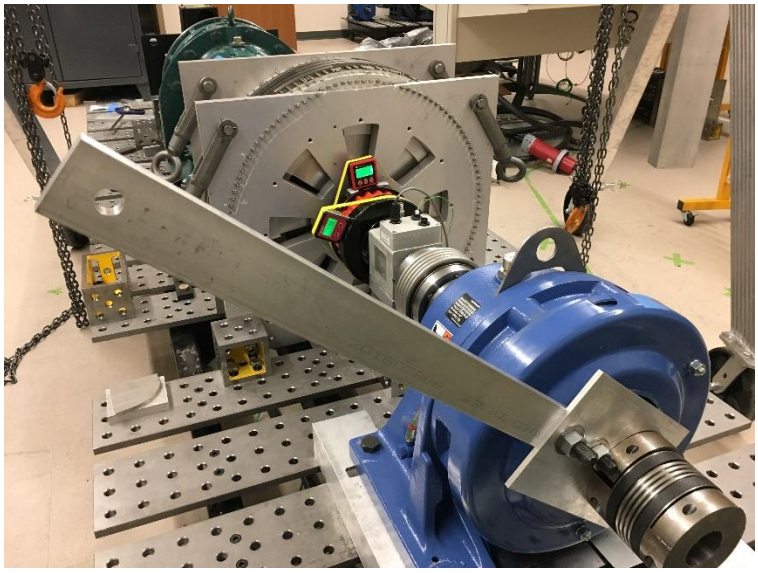

Figure 6-24: Full assembly of the of the stage 1 connected to the torque transducer, a mechanical gearbox (11:1 Sumitomo mechanical gearbox) and an aluminum bar for the static torque measurement.

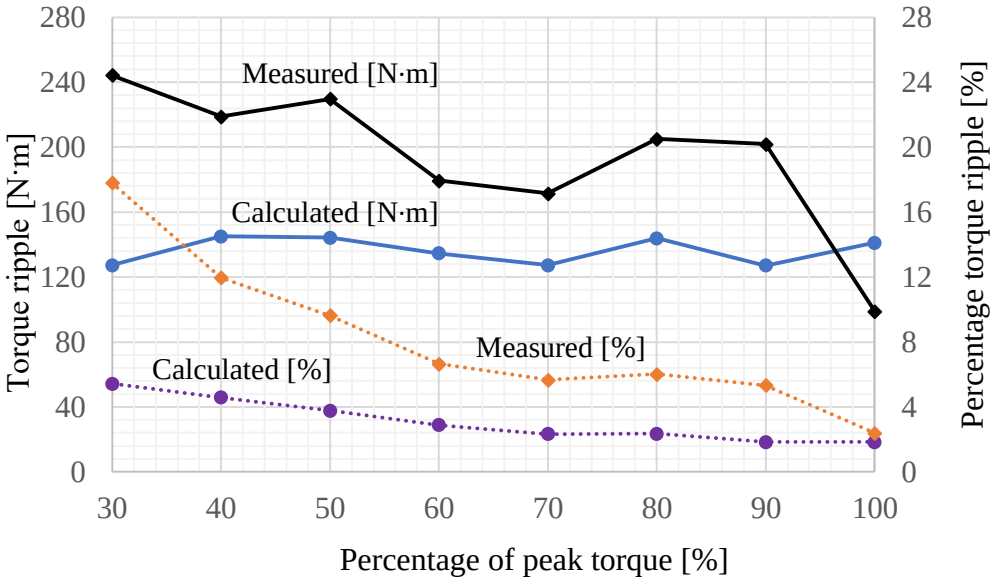

Figure 6-25: Torque measurement results versus the 3D FEA calculated values for the first stage of the MSMG design [69].

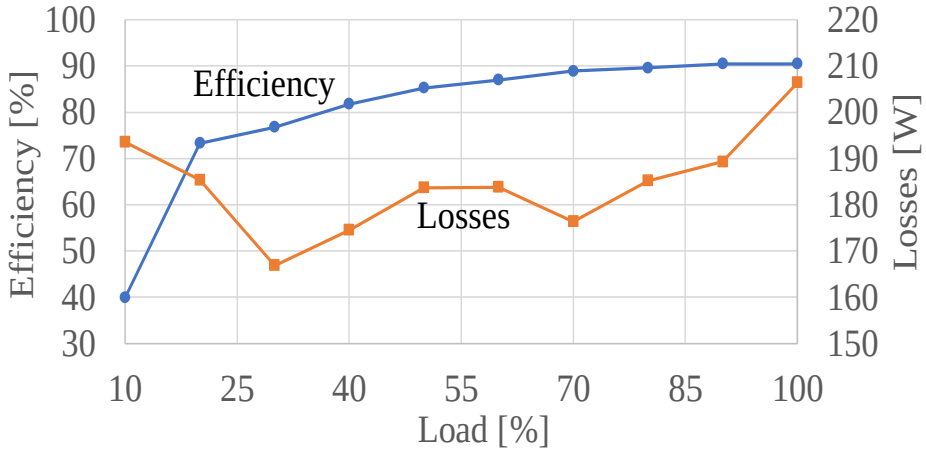

Figure 6-26: Measurement results of the efficiency and the percentage of power loss in the first stage design for different load conditions [69].

Figure 6-27(a) shows the full assembly of the MSMG design including both stages. The installation of the full MSMG design in the test setup is shown in Figure 6-27(b). The test setup includes a generator and a torque transducer on the low torque side of the MSMG, plus a Motor, Sumitomo mechanical gearbox and another torque transducer on the high-torque side of the MSMG. Unlike the first stage, this stage does not need any supporting ring in the axial direction since the lower magnetic forces in applied to the inner, cage and outer rotor of the second stage compared to the first stage, for which the side supports are strong enough to handle the radial forces. Peak torque value for the second stage is measured as 952 N.m. Volumetric torque density for the full MSMG is 118 N.m/L and the structural mass torque density is 14 N.m/kg. Power losses for the full MSMG is shown in Figure 6-28 and is compared with the losses of the first stage for different input speeds. The results show that very large power losses occur within the second stage of the MSMG design. These losses are mainly due to the presence of the large Aluminum plates in the magnetic fields which create very large eddy current losses. This phenomenon shows the importance of the edge effect analysis in the design of the MG's. Thermal images of the

MSMG during the operation also confirm these findings, as shown in Figure 6-29, in which the system is running for only 2 minutes, but the high temperature in the endplates and active region of the second stage is clear. The higher temperature of the inner components is evident in Figure 6-29(b). This issue may be addressed by optimizing the design and changing the material of the support components of the active region in the multi-stage HSMGG design.

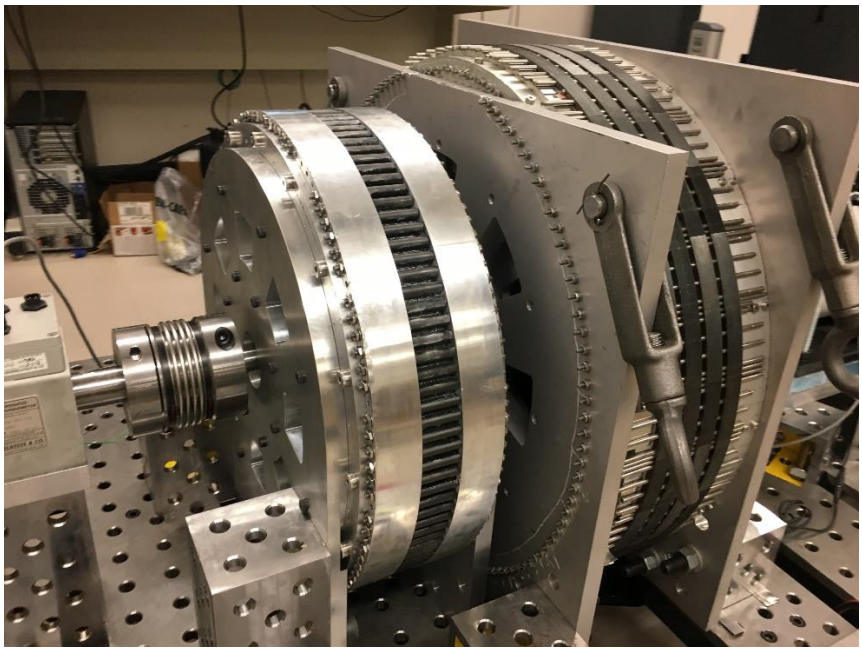

(a)

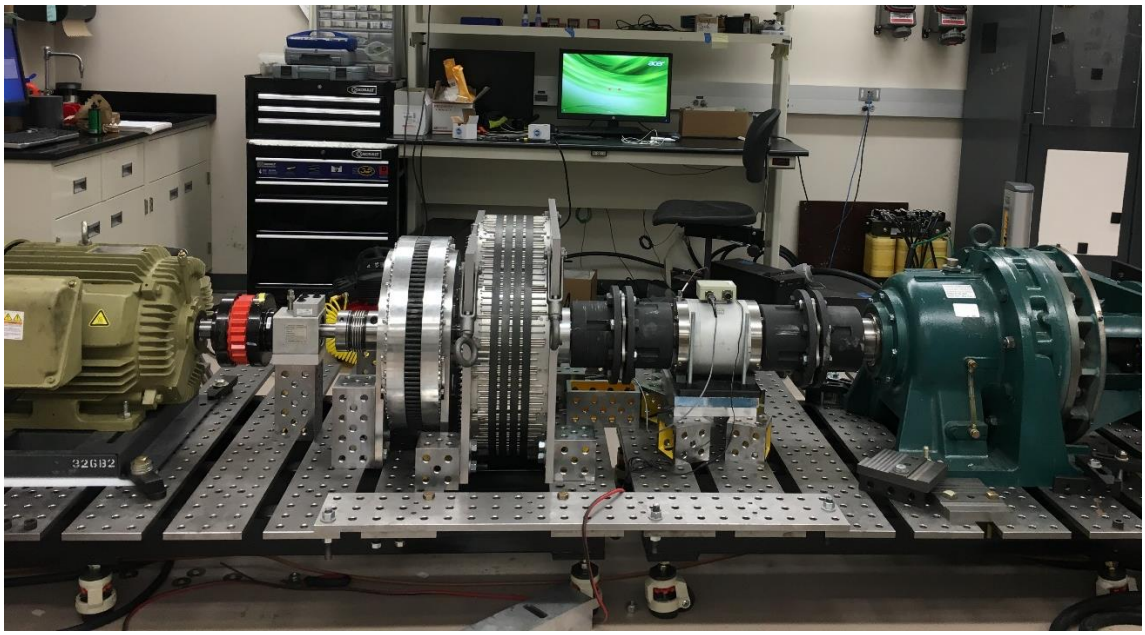

(b)

Figure 6-27: Full assembly of the MSMG design (a) separate, and (b) in the test setup.

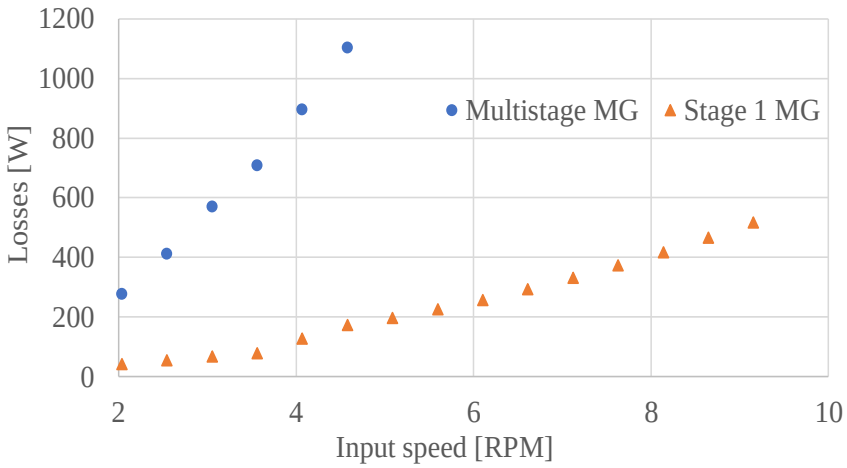

Figure 6-28: Power loss in the full MSMG design vs the first stage of the MSMG for different input speeds.

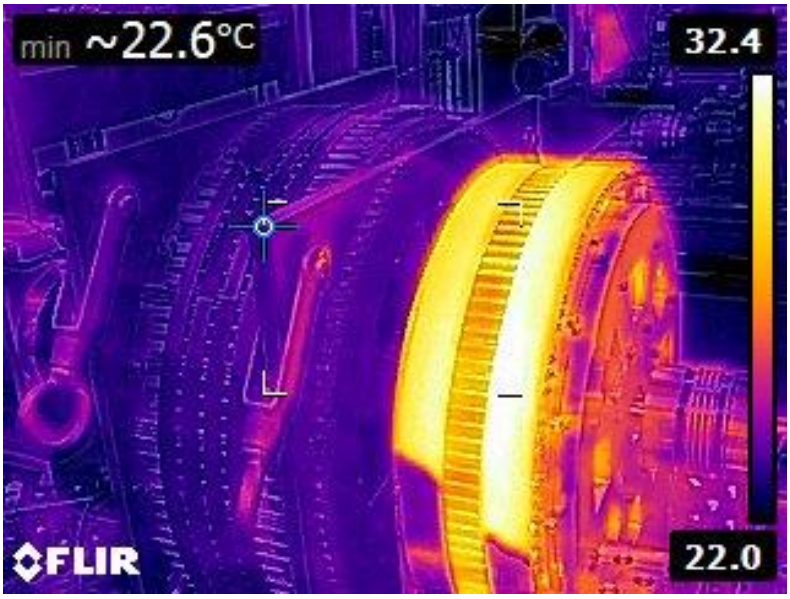

(a)

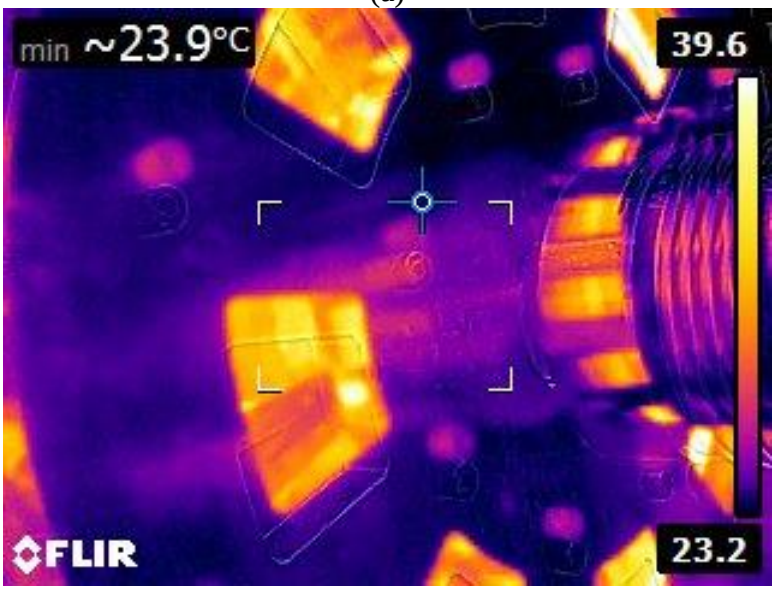

(b)

Figure 6-29: Thermal imaging of the MSMG design during no-load operation. (a) both stages, (b) inner components of the second stage.

6.2 MHK

6.2.1 Force Calculations

Multi-stage HSMGG is a sub-scale version of the multi-stage magnetic gear that is supposed to be designed for a 60KW Hydrokinetic generator. The forces in this design are lower than the MSMG design, so dealing with them is easier, both during the assembly and after the assembly is completed. The maximum radial forces in the MSMG design reaches to the order of 1 to 2 kN, while in this design, the maximum radial forces do not exceed 0.6 kN. This trend for the tangential forces is valid, as well. Figure 6-30 shows the radial and tangential forcers in the three rotors of the first stage of the multi-stage HSMGG design. In this figure, positive values for radial forces indicate outward force and negative values specify inward force. For tangential forces, positive values indicate a counter-clockwise direction of force and negative values specify a clockwise direction of force. These forces for the second stage which is low-torque/ high-speed side of the MG are lower, as shown in Figure 6-31.

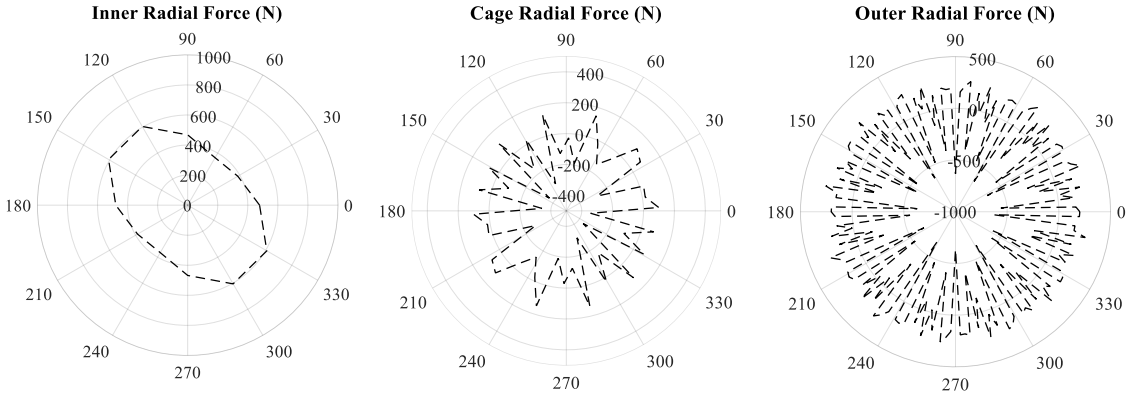

(a) (b) (c)

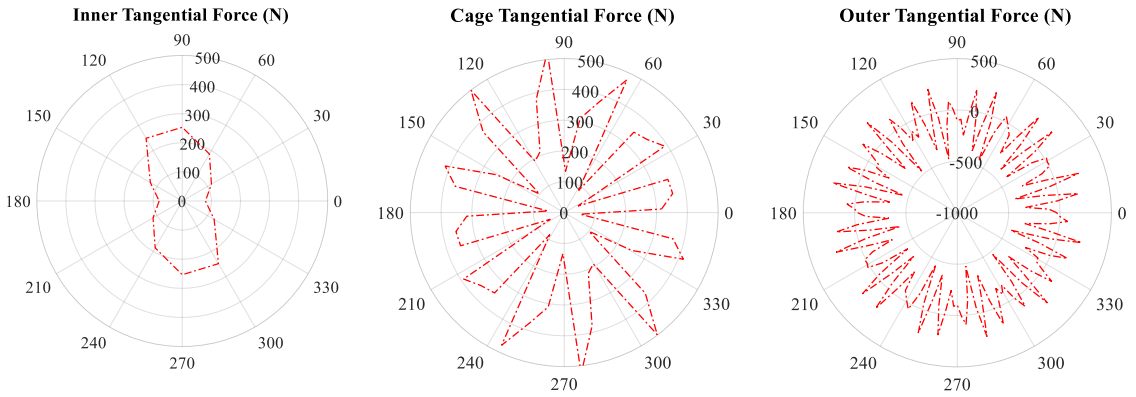

(d) (e) (f)

Figure 6-30: Radial and tangential forcers in the three rotors of the first stage of the multi-stage HSMGG design.

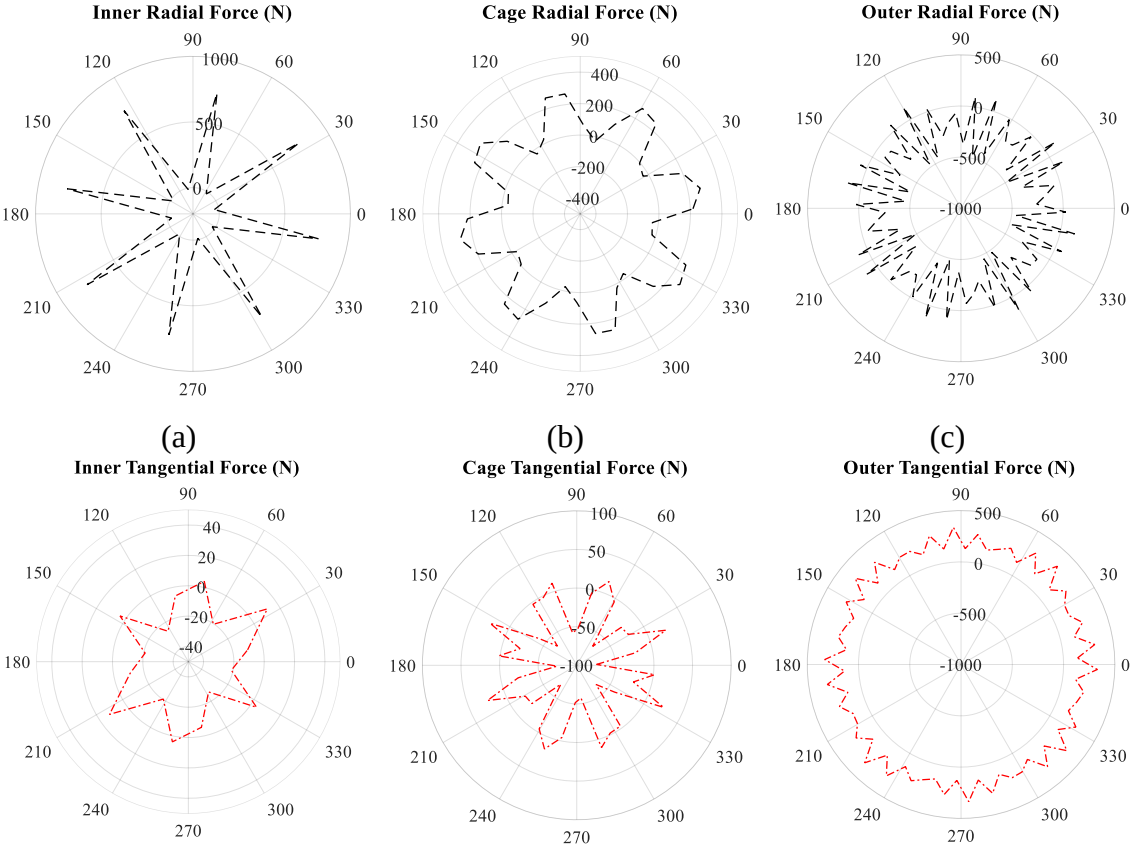

(a) (b) (c)

(d) (e) (f)

Figure 6-31: Radial and tangential forcers in the three rotors of the second stage of the multi-stage HSMGG design.

6.2.2 Structural Analysis

Structural analysis of the multi-stage HSMGG design prioritizes different aspects of the design compared to the MSMG design due to the different magnetic model and configuration, as well as the selected materials for the components in the active region. For the inner rotor, the main concern is still the rods deflection and the lamination bending. Figure 6-32 shows a finite element deflection analysis for the inner rotor of the multi-stage HSMGG design, with and without inclusion of the laminations effect (One lamination in the middle is there for the unity of the two rods passing through inner laminations). Knowing that the air gap between inner and cage rotors is designed to be 0.5mm, inner rotor rods in absence of lamination effects encounter maximum deflection of 0.116mm which is about 23% of the air gap, while lamination stack drops down the inner rotor deflection to about 0.0039mm, or 0.796% of the air gap. This amount of deflection is less than the tolerances of the manufacturing process, and completely acceptable for the purpose of this design.

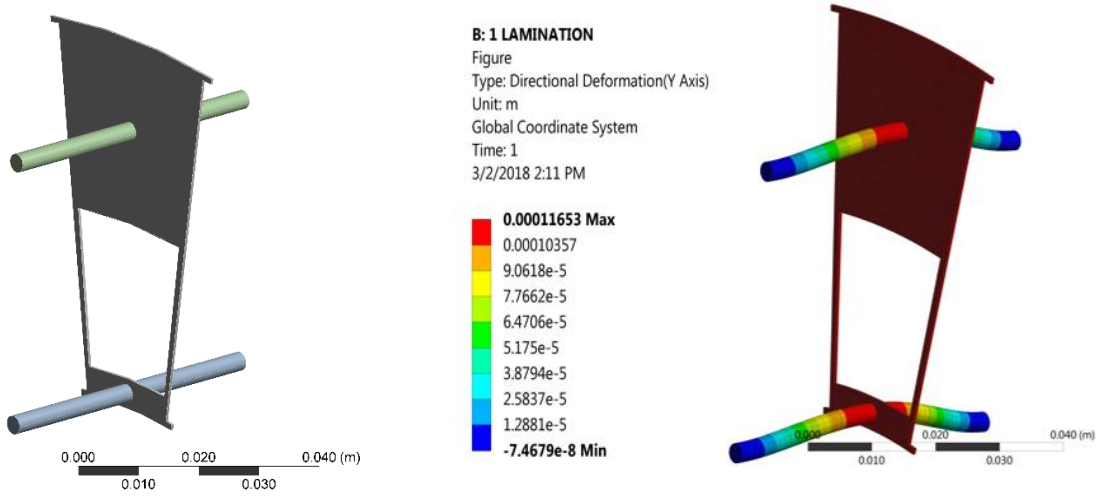

(a)

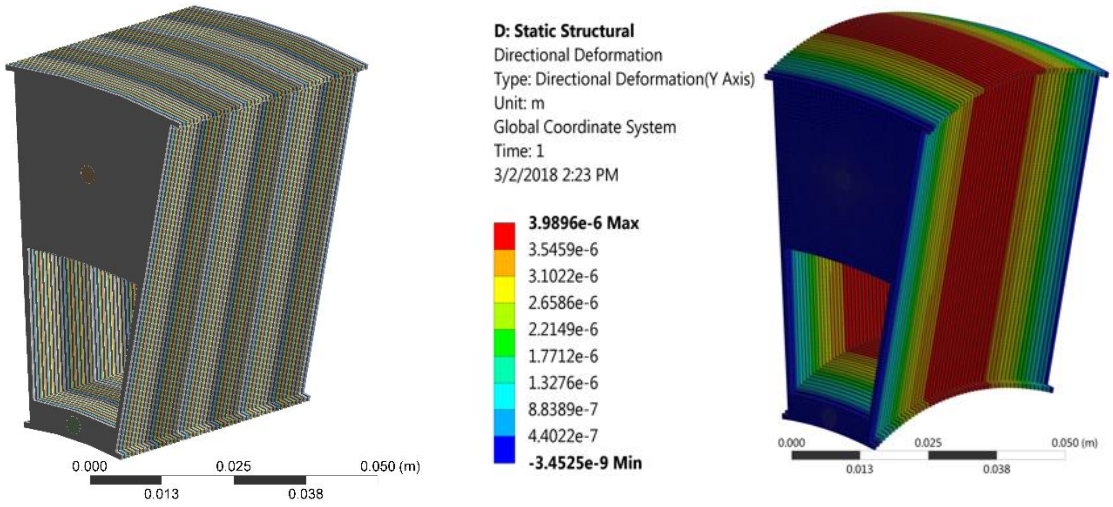

(b)

Figure 6-32: Deflection analysis for the inner rotor of the multi-stage HSMGG design, with and without inclusion of the laminations effect.

For the cage rotor, not only is the deflection of the supporting rods of great importance due to the high forces and relatively weak material (Garolite- due to the non-conductive, non-magnetic characteristics), but also the deflection analysis of the lamination tips is important, as the Garolite bars are in contact with the laminations on two tiny tips which needs to be studied to make sure they will tolerate the forces. Figure 6-33 shows a deflection analysis on the cage rotor Garolite bars and laminations under the radial and tangential forces. In this analysis, only 25 laminations are considered in the analysis for the sake of less computational time and load. The deflection results show a maximum of 0.03mm of radial deflection which is less than 10% of the air gap. Although the tangential deflection exceeds 0.13mm, it does not affect the air gap. The main concern with Garolite is that it is difficult to machine, specifically threading and tapping. So, the connections between the Garolite parts and the rest of the assembly should be either by pins or by glue. An FE is conducted on the cage bars under the operational condition with the focus on the connection area, shown in Figure 6-34. The figure shows a max. deflection of 0.2mm in

the center of the bar and 0.04mm of deflection at the two sides. These values do not take the bar to the plastic deformation. Also, in the full system, there are other components such as laminations and the endplates that carry some portion of these forces and the final deflection is lower than these values. The deflection analysis of the lamination tips shows very small deflection in these areas, eliminating the concerns about the deformation of these small sections under the operational conditions, as shown in Figure 6-35. Note that in this analysis, the equivalent forces are applied only to the lamination tips.

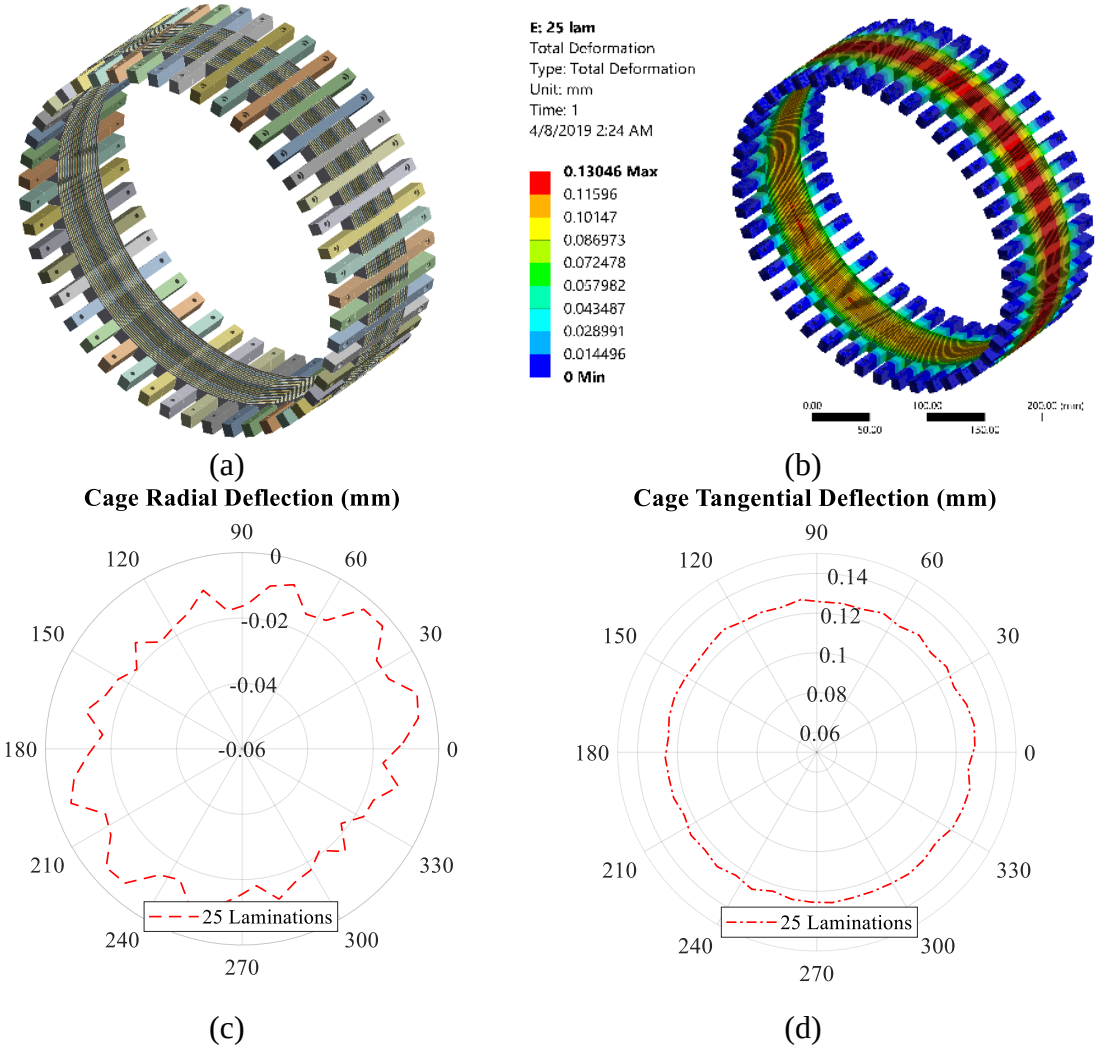

Figure 6-33: deflection analysis on the cage rotor Garolite bars and laminations under the radial and tangential forces

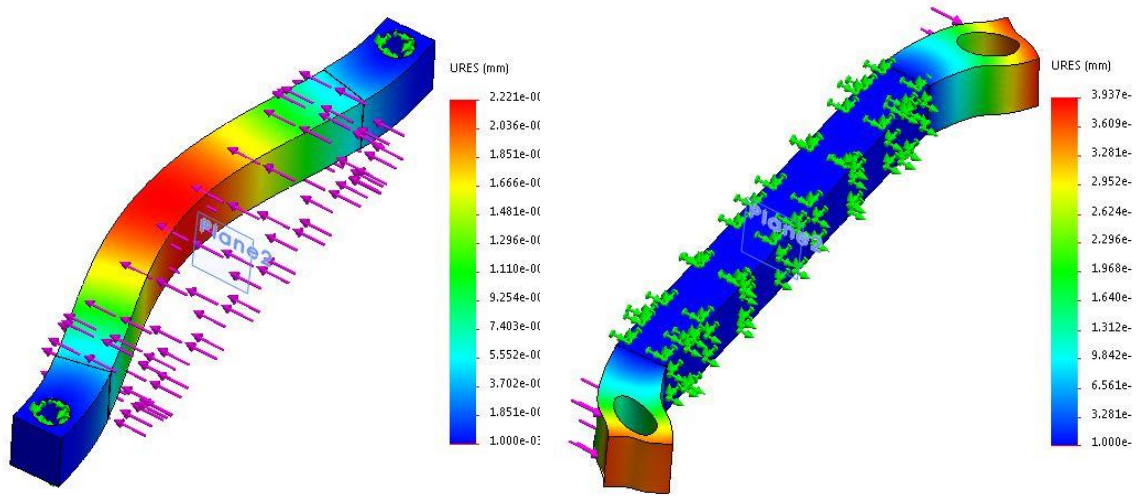

(a) (b)

Figure 6-34: An FE analysis on the cage bars deflection under the operational condition with the focus on the connection area.

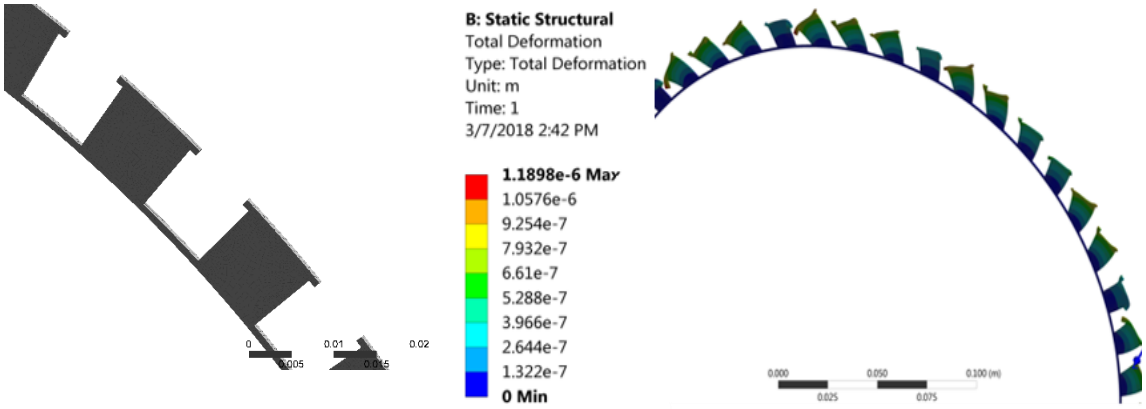

Figure 6-35: Maximum deflection in laminations tip area.

For the outer rotor of the multi-stage HSMGG, a Halbach design is considered, wherein there are no laminations between the magnets to hold them, but instead a back iron to which the magnets are glued. This magnetic configuration increases the magnetic performance of the system, but the assembly is challenging. Figure 6-36 shows the deflection analysis of the outer rotor of the first stage. The maximum deflections are calculated in the eight (8) positions that the supporting rods are passing. Maximum radial and tangential deflection do not exceed 0.04mm.

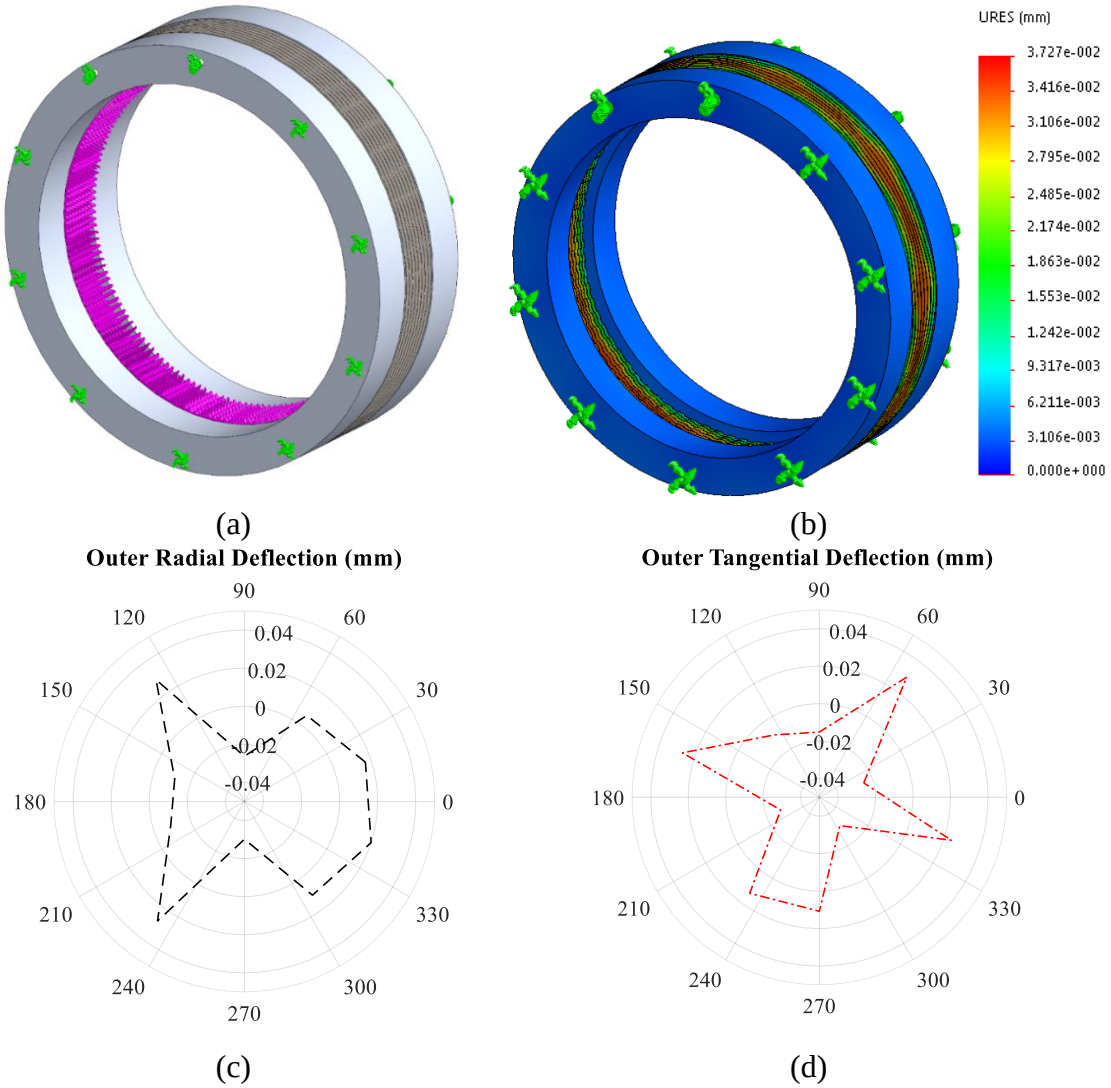

Figure 6-36: Deflection analysis of the outer rotor of the first stage of the multi-stage HSMGG.

6.2.3 Loss Calculations

6.2.3.1 Edge Effect

Magnets arrangement in a magnetic gearbox aims to focus maximum rate of magnetic field in the active region. The Halbach design is a breakthrough in this context, but still a small percentage of the flux leaks in radial and axial directions. Figure 6-38, Figure 6-39, and Figure 6-40 show the magnetic field density along the axial length at

different radial length position corresponding to inner rotor (Part A), cage rotor (Part B) and outer rotor (Part C), for the HSMGG, stage1. Parts A is exposed to the magnetic field of the outer rotor magnets, both inner and outer magnets influence Part B, and Part C is exposed by inner rotor magnetic field. Middle radial position of each part is considered for calculating the field in each part. Figure 6-37 shows the selected radial locations on the inner, cage and outer rotors.

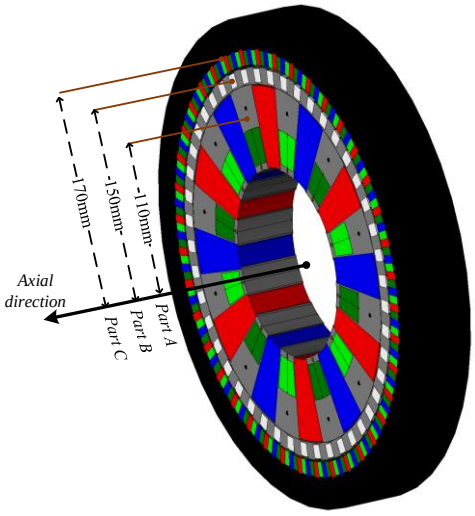

Figure 6-37: Selected radial locations on the inner, cage and outer rotors (Provided by H. Baninajar, PhD student, PSU).

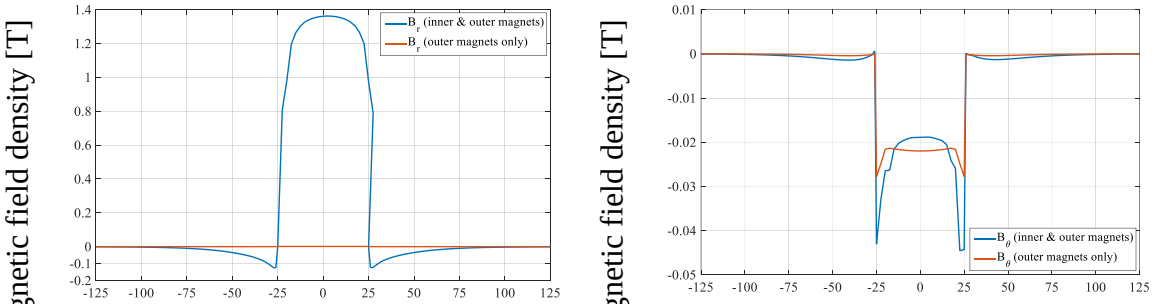

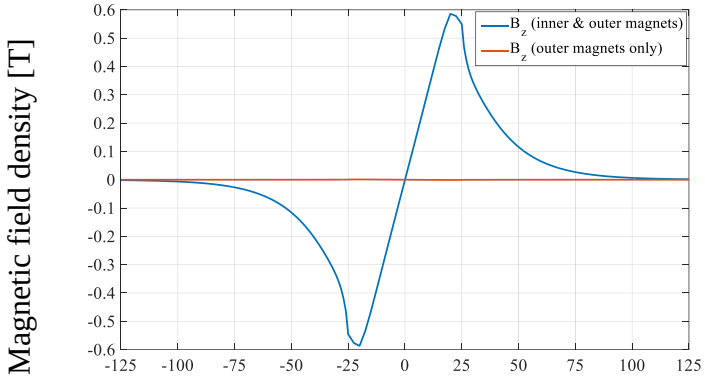

(c)

Figure 6-38: Magnetic field density along the axial length at different radial length position corresponding to inner rotor (Part A) (Data provided by H. Baninajar, PhD student, PSU).

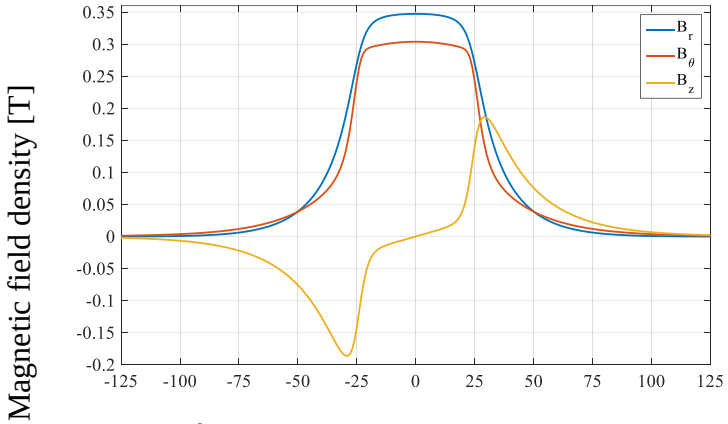

Figure 6-39: Magnetic field density along the axial length at different radial length position corresponding to cage rotor (Part B) (Data provided by H. Baninajar, PhD student, PSU).

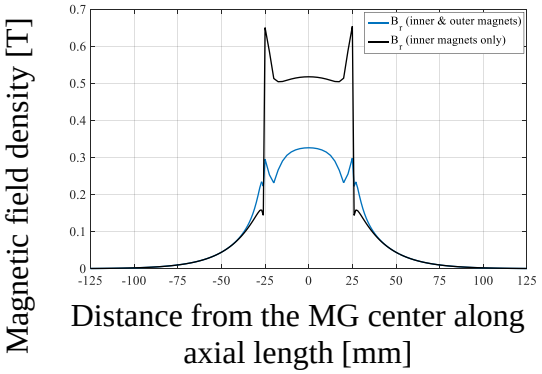

(a)

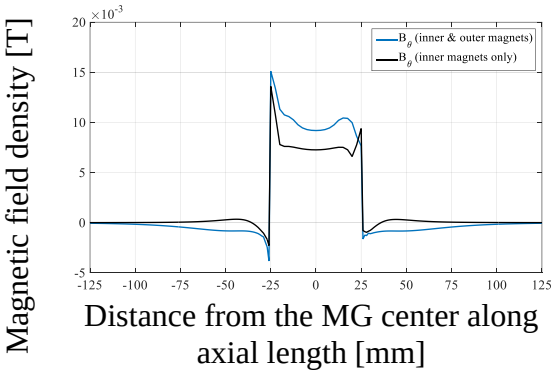

(b)

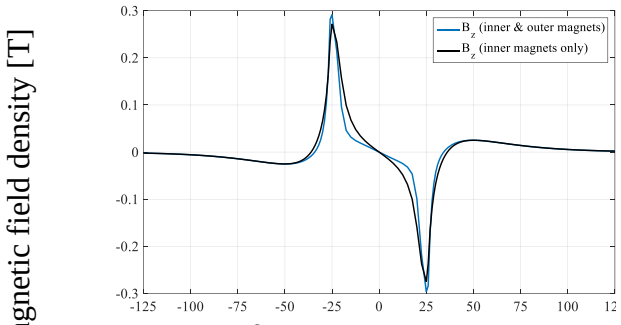

(c)

Figure 6-40: Magnetic field density along the axial length at different radial length position corresponding to outer rotor (Part C) (Figure provided by H. Baninajar, PhD student, PSU).

Magnetic field passing through conductive endplates with relative rotational speed results in eddy current losses, which not only decrease the performance, but also produce thermal stresses and an increase in temperature. According to magnetic field density results in Figure 6-38, it seems that almost zero magnetic field due to outer rotor magnets affect inner rotor (Part A) within off-active region, so if the structures in part A rotate at the same speed as inner rotor, negligible Eddy current is expected due to changing magnetic field. As in Figure 6-39, since the cage and the supporting structures in part B are fixed, so it sees the magnetic field due to both inner and outer magnets; so, any structure along the axial length within part B should be non-conductive.

While the outer magnets presence changes the magnetic field density within the active region, it has a minor effect on magnetic field in off-active region, since the inner rotor magnets are stronger and more dominant. So, a changing magnetic field density applies on the structures located in the same radial position as part C, as in Figure 6-40.

While the exact loss value is not a result of this study, it is recommended to use a non-conductive material.

6.2.3.2 Material Selection and Sealing

In-active-region support components are responsible for carrying the torque and loads in the system and need to be stiff and strong enough to avoid undesired deflections. On the other hand, according to the magnetic flux density results in the "Edge Effect" section, it is recommended to avoid using conductive materials such as Aluminum and Stainless Steel in the active region. This is also true for the 25-30mm away from active region in axial direction, especially for the cage and outer rotor area, which experience high rate of magnetic flux leakage. So, a material study is presented in TABLE 6-4 to select the most appropriate options. Accordingly, Delrin is a fine choice for structures that carry low rate of loads, as the tensile strength of it is low, but it is a cheap and easily manufacturable option. Axial spacing rings designed for cage rotors of HSMGG stage1 and 2 are both made of Delrin. On the other hand, some structures, including cage bars carry higher loads than Delrin strength, so Garolite (G10) is selected for most of the parts in direct contact with active region, as G10 is almost as strong as Aluminum and fairly cheap, plus it is a common material for national vendors. Although, the only problem with G10 is that it is not a good option for machining, as it is tough to tap and wears through tools. So, using Garolite requires modifications in the system, to crating threads in these parts. Cage bars (HSMGG stage 1 and 2), cage endplates (HSMGG stage1) and outer rotor rings (HSMGG stage 1 and 2) are made of Garolite G10.

TABLE 6-4: Material selection table for in-active-region support components.

Material	Aluminum 6061	Delrin	Delrin (GF)	Garolite	Carbon Fiber	UHMW PE
Cost	$$$	$$	$$$$	$$	$$$$	$
Machinability	Easy	Easy	Medium	Tough	Tough	Easy
Tensile Strength	35,000 psi	9,000 psi	8,700 psi	32,000 psi	40,000 psi	5,000 psi
Notes				1. Tough to tap 2. Wears through tools 3. Water Jet Recommended 4. Must control dust	1. Tough to drill 2. Tough to tap 3. Wears through tools 4. Water Jet Recommended	

Active region is the area in which most of the magnetic flux is focused. Main components in this region comprise permanent magnets, laminations, and support rods/ bars. Rare-earth permanent magnets in the three designs are NdFeB, and the laminations are M6. Components outside of the active region are mainly Aluminum 6061, or 7075, as Aluminum provides high strength to the part. Between the two types of the selected Aluminum, 6061 is of lower stiffness, easier to machine and cheaper than 7075. For the cage rotor endplates that carry the high torque, Aluminum 7075 is recommended, as in MSMG stage1. Input and output shafts are carrying both the torque resulted by magnetic interactions as well as the weight of all components. Moreover, they are not allowed to deflect much, as their deflection directly affect the air gap size. So, it is strongly recommended to make them out of Alloy Steels. Stainless Steel 303, 4041, and1018 are respectively used for the input and output shafts of the LMG, MSMG and HSMGG. Stainless steel alloy was selected for all other additional assembly components, such as

nuts and bolts, key stocks, retaining rings and bearing, I order to provide the highest stability in the system. TABLE 6-5 shows the properties of all the materials used in the three designs. Note that the prices in TABLE 6-5 are based on McMaster-Carr listings.

TABLE 6-5: Material properties [137] [138].

	Properties				
Material	Density (Kg/m3)	Tensile Strength (MPa)	Modulus of Elasticity (GPa)	Water absorption (%)	Price ($) (6” x 6” x 1/4”)
Al 6061	2700	310	68.9	-	11.97
Al 7075	2810	450	71.7	-	23.85
Steel 303	8000	620	193	-	60.04
Steel 4140	7850	655	210	-	-
Steel 1018	7870	370	205	-	23.77
NdFeb	7600	75	150	-	-
Garolite (G10)	1900	220	18	0.15	20.30
Delrin	1420	40.7	2.9	0.25	9.43

Hermetically Sealed Magnetic Gear Generator (HSMGG) is designed to pull off the submarine test. This magnetic gear generator is for a Marine Hydro Kinetic Generator. Cage rotor of the first stage and outer rotor of the second stage are the boundaries of the sealing. Outer rotor magnets of the first stage will also be coated with waterproof material to make sure magnets and laminations will not be damaged. The first step to seal the designated area is to make sure all the sealing parts are fully connected and no gap is in the design. For this purpose, sealing components for the cage rotor of the stage1 and outer rotor of the stage2 are designed to separate the two regions. A list of components in contact with water are listed in TABLE 6-6. The second attempt to complete the sealing is to cover the magnets, laminated components and Garolite/ Delrin components with a thin layer of waterproof glue, called moist metal grip [118].

TABLE 6-6: List of components in contact with water.

Component Name	Stage Number
Cage rotor lamination	Stage 1
Cage rotor bars	Stage 1
Cage rotor support rings	Stage 1
Cage rotor endplates	Stage 1
Cage rotor Sealing	Stage 1
Outer rotor rings	Stage 2
Outer rotor endplates	Stage 2
Outer rotor back iron (laminated)	Stage 2
Stator ground-plate	Stator
Stator tube housing	Stator

6.2.3.3 Losses

For the loss analysis of the multi-stage HSMGG, the eddy current losses are calculated using a finite element method for 40RPM rotational velocity of the low-speed/ high-torque shaft, in the first stage. Losses are calculated in the active region component and divided into nine different regions, including inner rods (lower and upper), inner magnets (small and large), inner laminations, cage laminations, outer magnets (small and large), and outer back iron. TABLE 6-7 shows the eddy current losses in different sections of the active region. The volumetric eddy current losses are also illustrated in Figure 6-38. In the design of the multi-stage HSMGG, the material selection is optimized to avoid losses, specifically eddy current losses. As was shown in the MSMG loss analysis, in the active region, main losses were generated in the cage rods which are of steel material, but in the multi-stage HSMGG design, the steel rods are substituted with Garolite bars to avoid eddy current losses. This can be seen in Figure 6-41, where the cage losses are much lower

than the inner and outer losses. To avoid the edge effects, a minimum of 40mm axial space between the active region and the rotating conductive/magnetic materials is preserved.

TABLE 6-7: Eddy Current Losses for 40 RPM Velocity on Low speed Shaft.

	In-rod -lower	In-rod -upper	Inner small MG	Inner large MG	inner lamination	cage lamination	Outer Small MG	Outer Large MG	Outer Back Iron
Loss (W)	9.26×10^{-12}	3.99×10^{-7}	0.001	2.879	0.072	5.738	3.615	3.270	1.596
Volume (m^3)	1.07×10^{-5}	1.07×10^{-5}	0.001	0.001	0.001	0.354	0.001	0.001	0.001
Vol. Loss (W/m^3)	8.6789×10^{-7}	3.75×10^{-2}	0.405	2665.989	93.82	16.211	11763.432	9793.841	1104.124
Volumetric Loss (W/L)	0.001	37.472	405.426	2665988.919	93819.941	16210.811	11763432.07	9793840.918	1104124.1

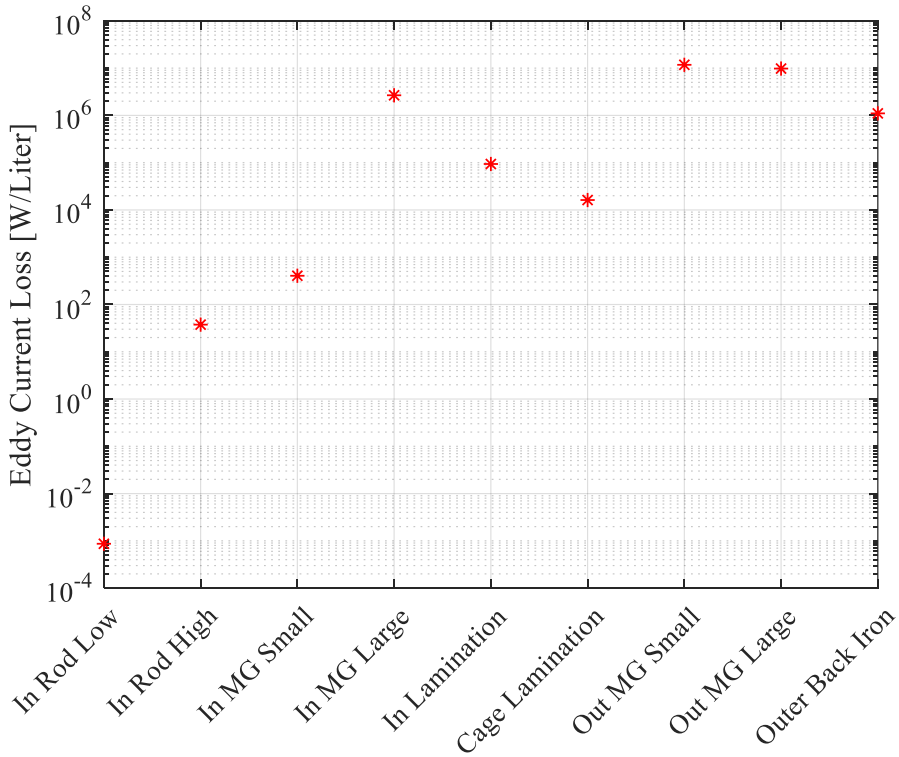

Figure 6-41: Volumetric Eddy Current Losses for 40 RPM Velocity on Low speed Shaft.

6.2.4 Thermal Analysis

For the thermal analysis of the multi-stage HSMGG (stage1), the conduction method is used as it was shown in the previous analysis for the laminated design (LMG) that for the systems with similar conditions, the results of the thermal analysis using the conduction method and coupled method (conduction-convection method) are fairly close, and due to the shorter run- time and smaller used memory, the conduction method is used for the analysis of this system. The following conditions are conducted in this analysis:

- Free convection is considered on all exterior surfaces.
- Conduction approach is used for the air gaps.
- Symmetry condition is considered in axial (Z) direction.
- Parts are supported on one end and the other end would have the same boundary conditions due to the symmetry in Z direction.
- Deformation is shown on the symmetry plane, while Stress is shown on the support side.
- Outside temperature is 297.15 [K].

Figure 6-42 shows the temperature distribution in the active region in this model. The outer rotor has the highest rate of the temperature unlike the laminated design in which the cage rotor had the highest rate of temperature, and this is compatible with the distribution of losses in the system. The overall temperature is increased between 5.5 [K] to 7.5 [K] which is in a very normal and acceptable range. This is a great breakthrough in the design and manufacturing of the magnetic gears. The thermal analysis results for different rotors are shown in Figure 6-43, 6-44, and 6-45. For the inner rotor, magnets have higher temperature compared to the laminations. For the cage rotor, the temperature is

distributed evenly all around the cage laminations. For the outer rotor, the inner race which is the magnet's position has the highest temperature. The thermal deformation of the components under the thermal effects is shown in Figure 6-46, based on which high deformation of the cage tips is considerable.

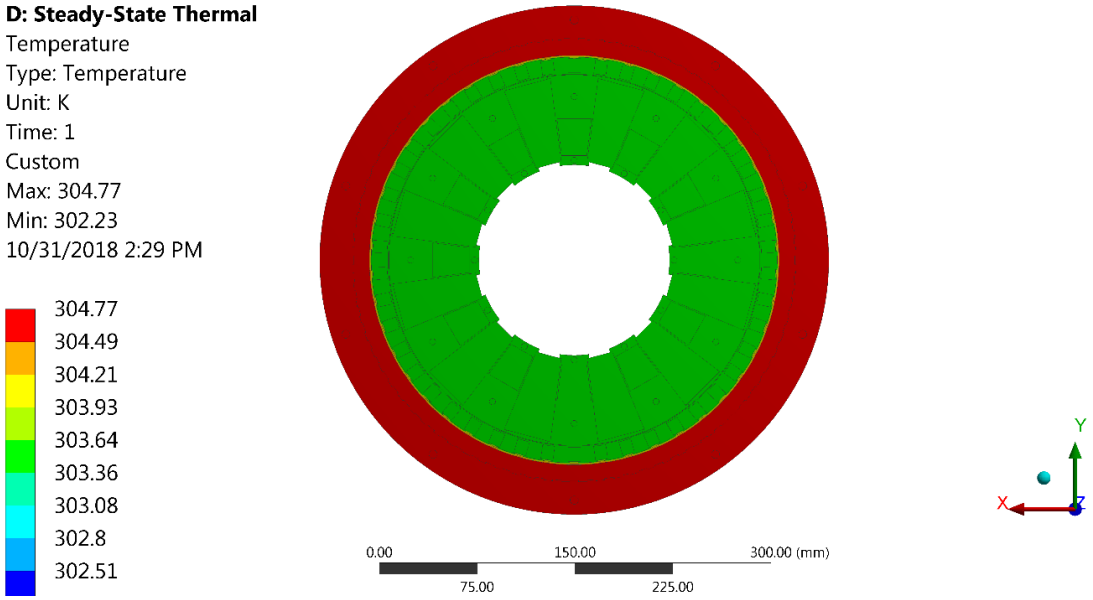

Figure 6-42: Temperature contour for magnetic gearbox components for the rotational velocity of 40 rpm on the low speed shaft.

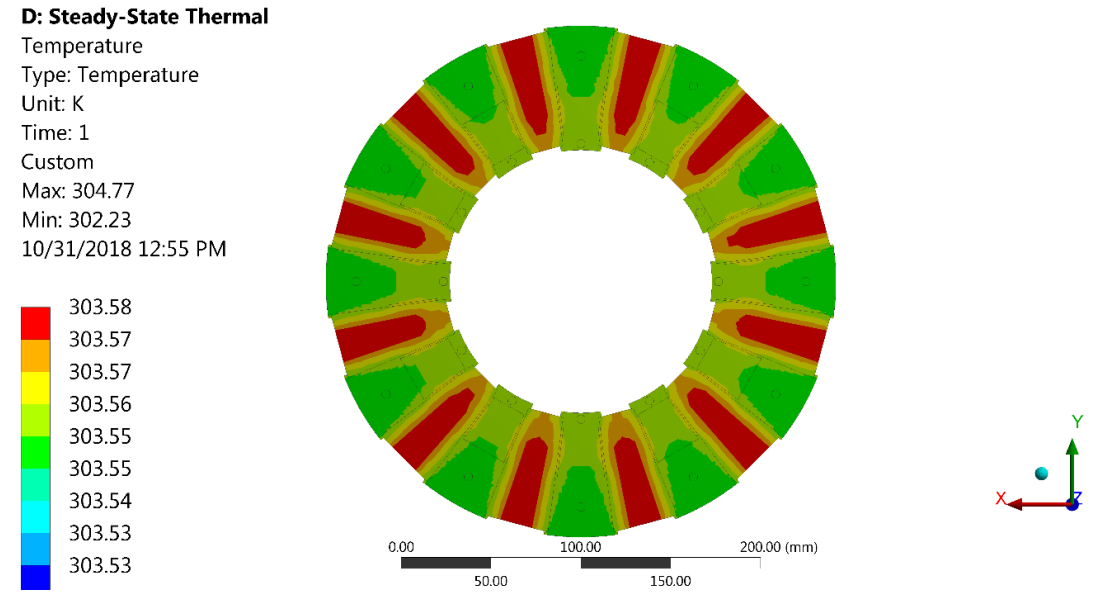

Figure 6-43: Inner rotor temperature contour for the rotational velocity of 40 rpm on the low speed shaft.

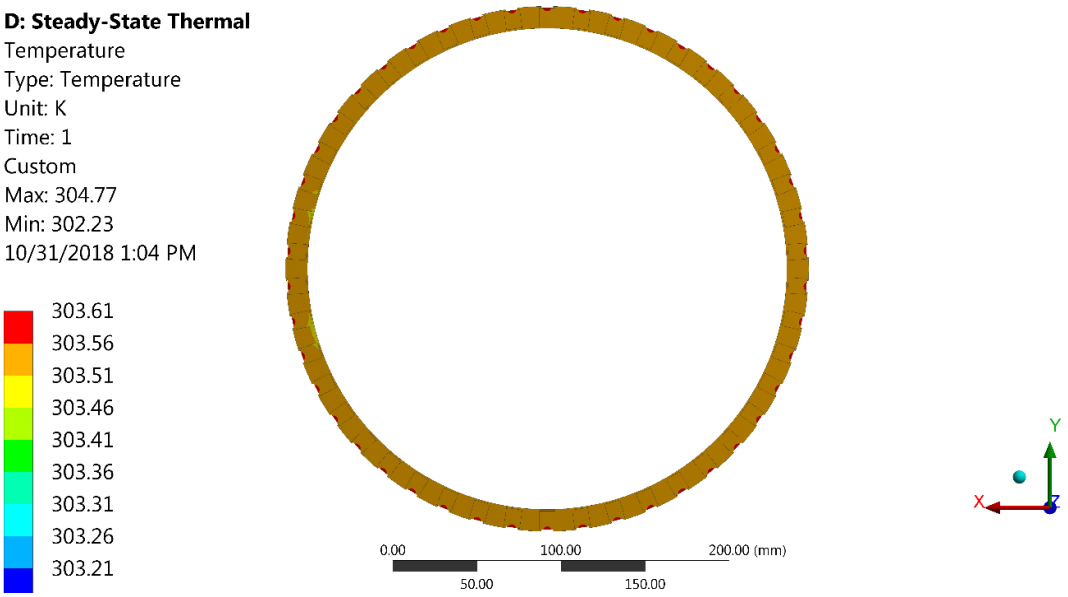

Figure 6-44: Cage rotor temperature contour for the rotational velocity of 40 rpm on the low speed shaft.

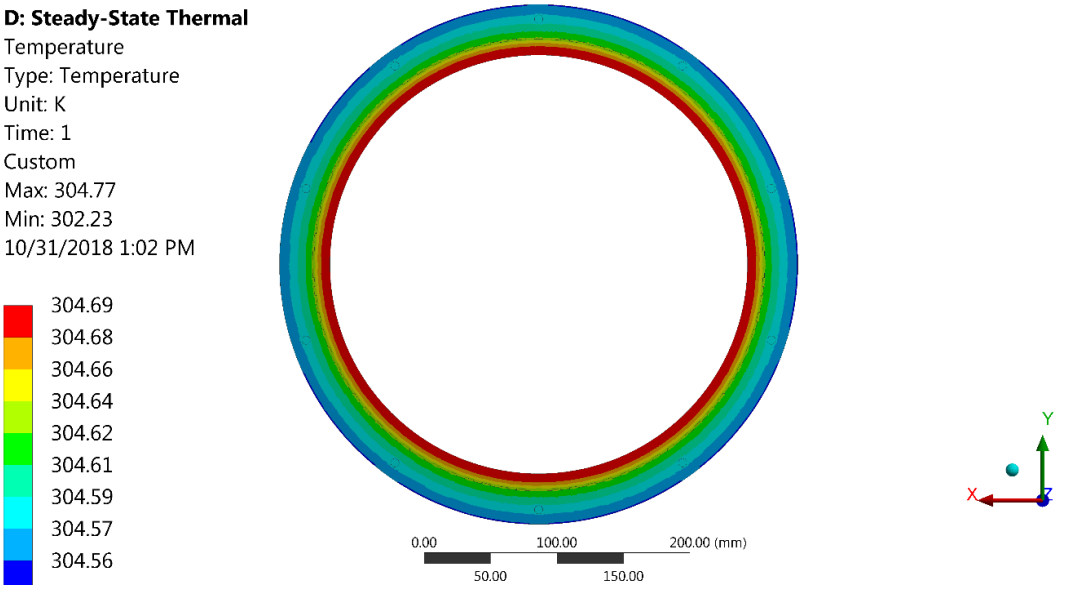

Figure 6-45: Outer rotor temperature contour for the rotational velocity of 40 rpm on the low speed shaft.

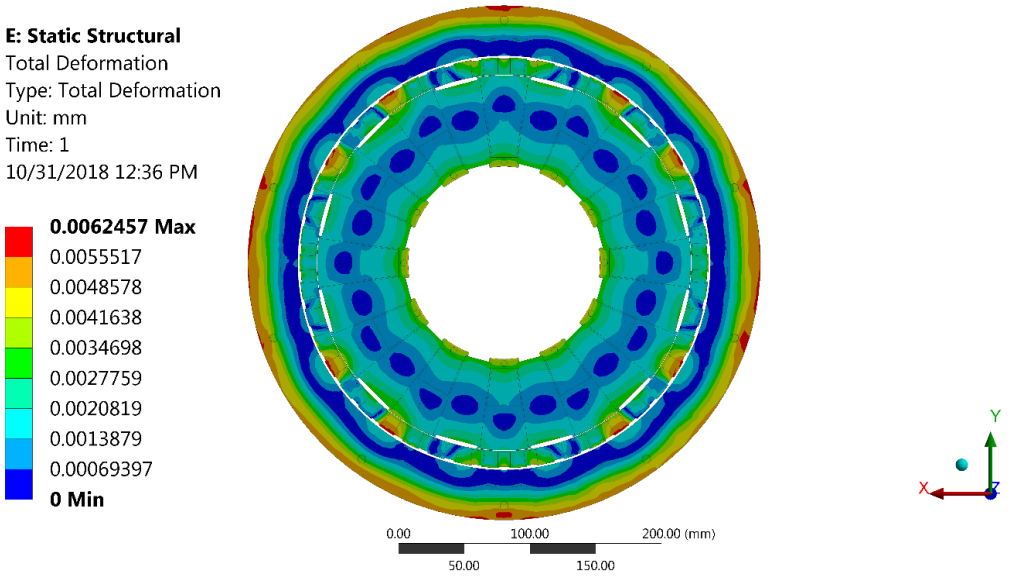

Figure 6-46: Thermally caused deformation of the first stage of MHK subscale design for the rotational velocity of 40 rpm on the low speed shaft.

6.2.5 Final Design

Major specifications and changes of the multi-stage HSMGG design in comparison with the previous design including the MSMG are as follows:

- Inner and outer rotor magnetic configuration is changed to Halbach design in which the magnets have three different orientations. This will increase the magnetic performance of the system.
- The laminations are totally removed from the inner rotor of the second stage and outer rotor of both stages. This will result in larger magnets in smaller area and higher performance.
- Cage rotor steel rods are substituted with Garolite square bars between the adjacent poles. This will considerably decrease the eddy current losses in the system.

- Cage rotor design is changed to single inner bridge design, which provides higher peak torque compared to the double bridge.
- All magnets, are glued to the supporting structure to provide the support against magnetic forces, in addition to the noise cancellation.

Figure 6-47 shows the final configuration of the active region in the multi-stage HSMGG. The assembly of inner, cage and outer rotors, separate from the full assembly, are shown in Figure 6-48. A 3D model of this system is shown in Figure 6-49. In this design, the stator is connected to the output/ high-speed shaft of the MG. The system is designed so that the area inside the cage rotor of the first stage, the whole second stage and the stator be sealed. A full assembly of the second stage installed in the no-load test is shown in Figure 6-50(a). The assembly of the second stage and the stator is also shown in Figure 6-50(b). A static test has been conducted on the second stage and the results are shown in Figure 6-51. The peak torque was initially calculated as 24 N.m through a 3D-FEA analysis, and the measured peak torque is 23.8 N.m. which shows a good agreement between the concept design and the prototype.

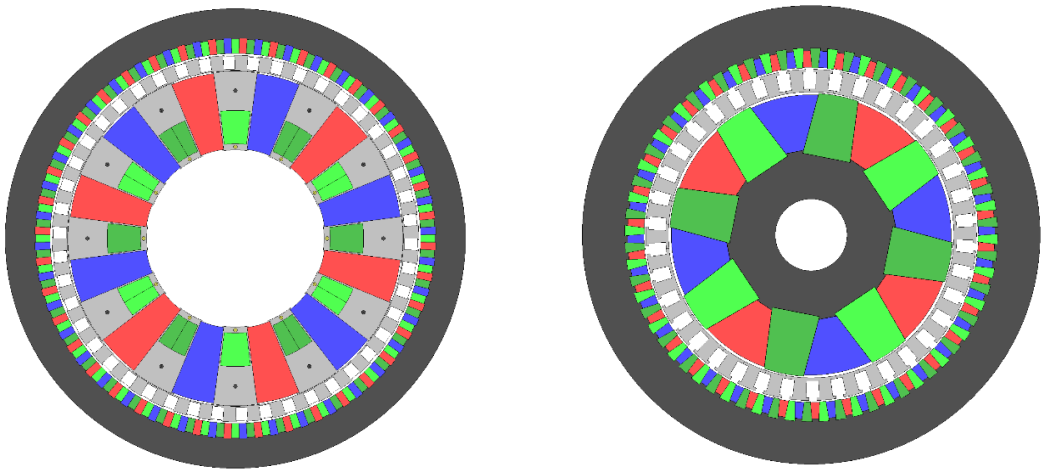

(a) (b)

Figure 6-47: Final magnetic topology of the multi-stage HSMGG (a) stage1 and (b) stage2.

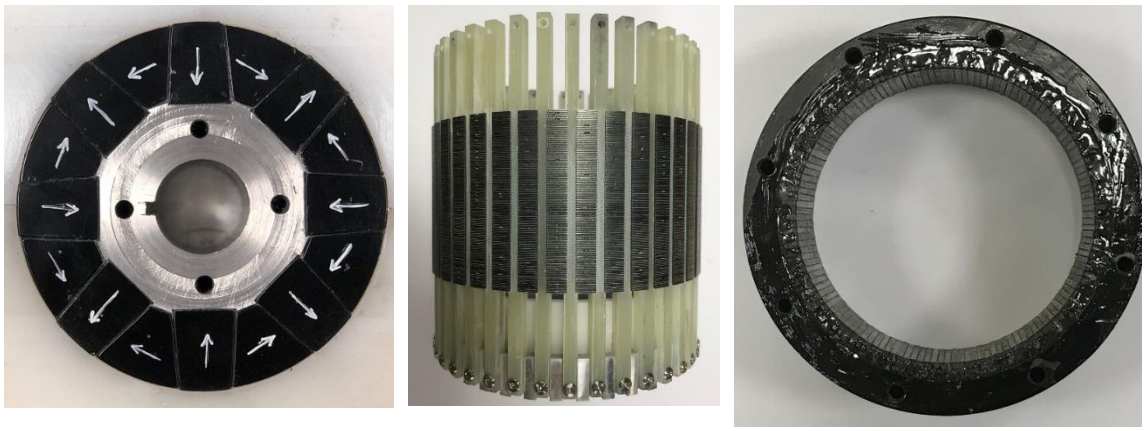

(a) (b) (c)

Figure 6-48: Assembly of the inner, cage and outer rotors, separate from the full assembly (stage 2) [139].

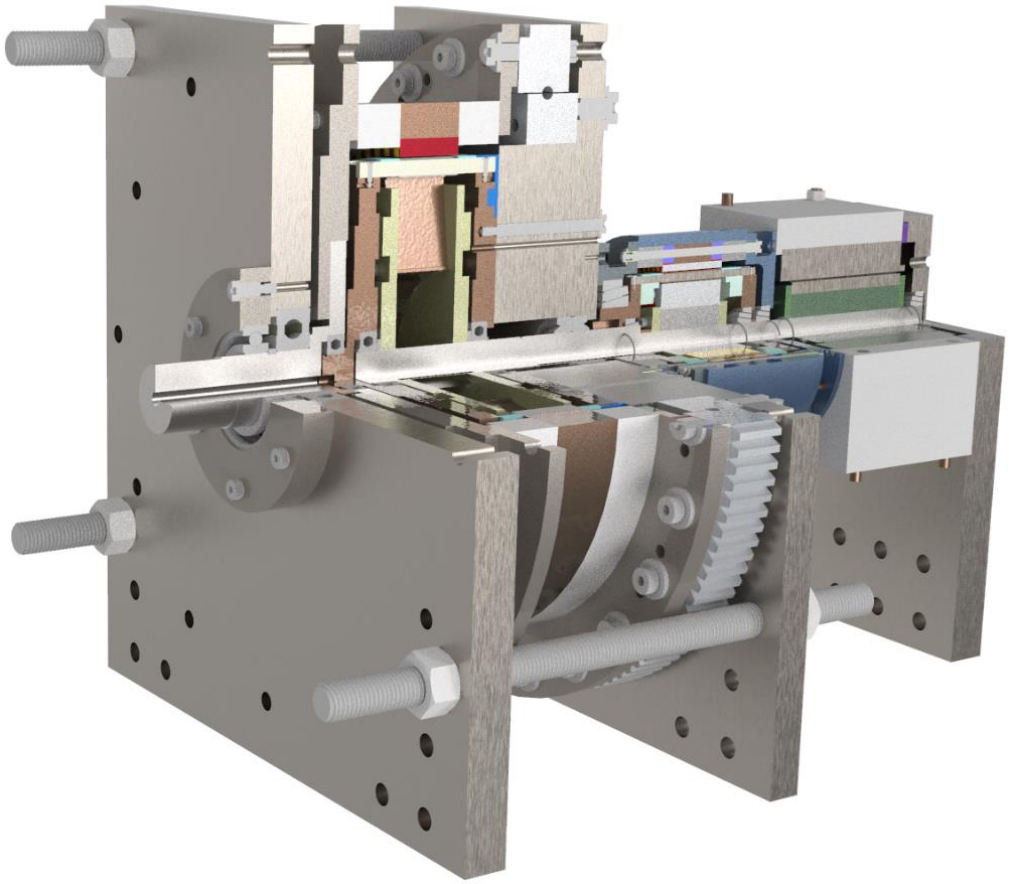

Figure 6-49: 90-degree cutaway view of the final assembly of the (a) MSMG, and (b) HSMGG designs.

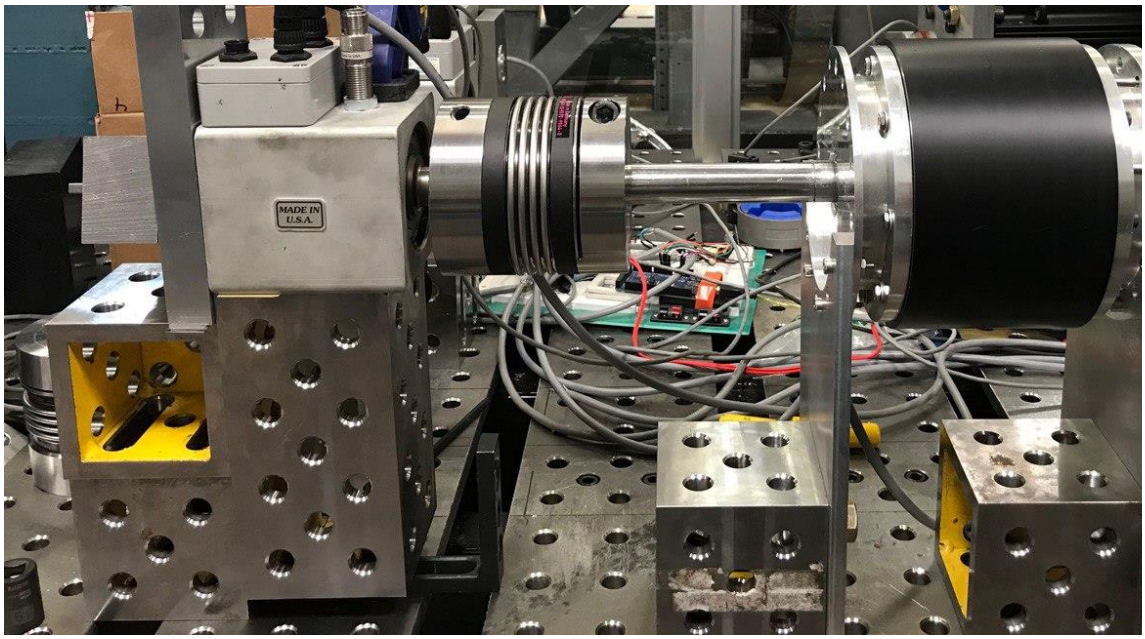

(a)

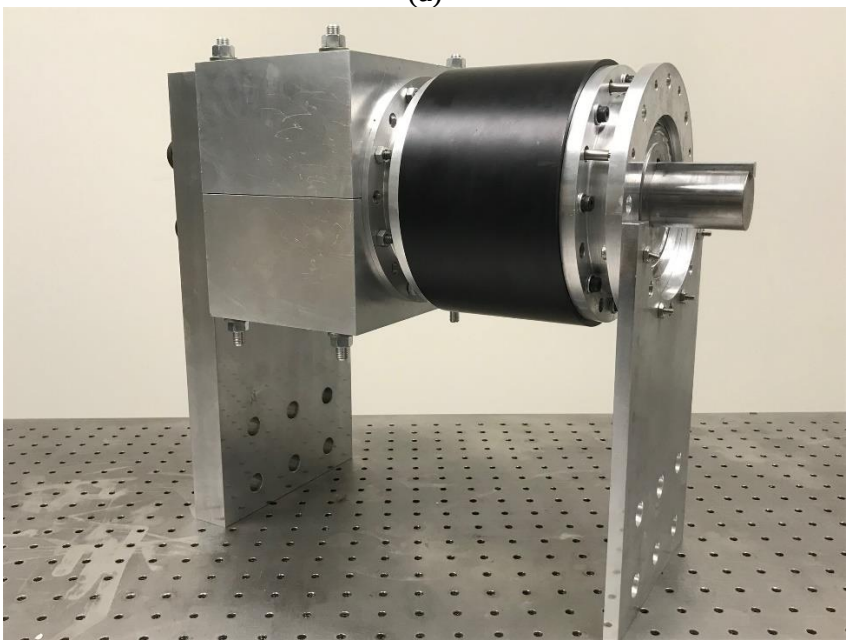

(b)

Figure 6-50: (a) Full assembly of the stage 2 of the multi-stage HSMGG design, and (b) stage 2 connected to the stator.

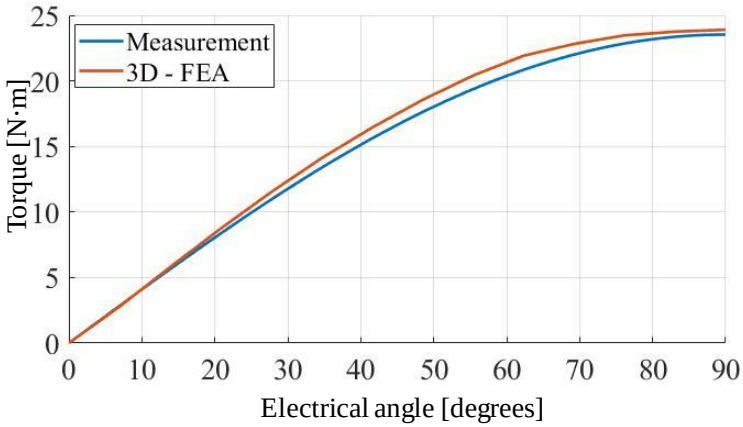

Figure 6-51: 3-D FEA vs Experimental inner rotor pole-slip plot over 90 degrees electrical angle

6.3 LAMINATION STUDY

Modulating pieces in an MG are recommended to be made of laminated stacks united with a fine layer of bonding agent, oven cured and fused together [140]. Despite the advantages of laminations on the magnetic performance and efficiency of the system, they have shown a much lower mechanical stiffness properties compared to the solid counterparts. Knowing that the extremely small air gap between the rotating layers of an MG is the leading factor of the mechanical design of the system, higher stiffness is always demanded, which demands the performance of a detailed deflection analysis on the laminations and the bonding agent factor in the total stiffness of the stack. The test setup introduced in the Figure 4-7 was assembled to investigate the effect of the bonding agent of laminated stacks in an MG on radial stiffness of the system. Figure 6-52 shows the experimental results of the magnetic flux density data acquisition and compares it with the computed data using a 3D finite element analysis in JMAG software. The results show a promising agreement between the 3D model and the experimental setup.

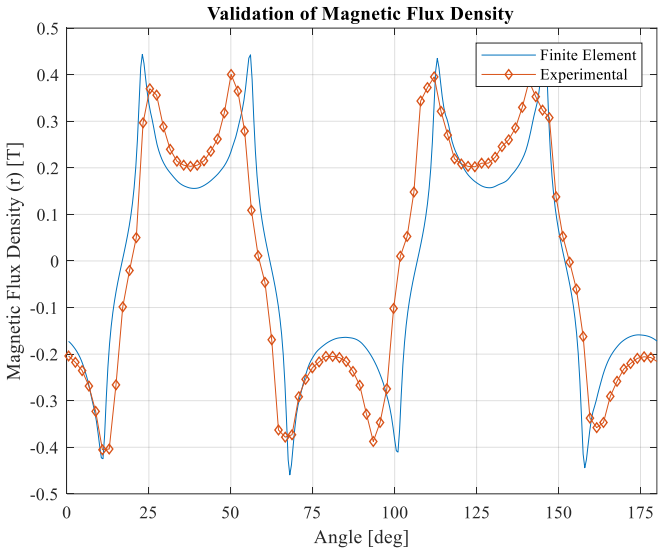

Figure 6-52: Validation of the magnetic flux density of the test setup with the 3D model in JMAG.

In order to investigate the stiffness of the lamination stack in the MG application, displacement of the laminated stack in the test setup is recorded. In these sets of measurement three devices are used including the TESA height gauge which provides 40 data points, laser measurement sensor that provides 250 data points, and the CMM with 60 points in each round of measurement. Based on the observed data, the laser measurement system and TESA height gauge show greater repeatability and agreement while the CMM is more susceptible to operator induced inconsistency. Experimental Deflection data for the position with highest rate of magnetic forces are shown in Figure 6-53. maximum deflection of the lamination is in the range of 0.155 mm to 0.165 mm. An outlier can be seen in all four measurements in the axial position of 25 mm which is due to a manufacturing-related anomaly.

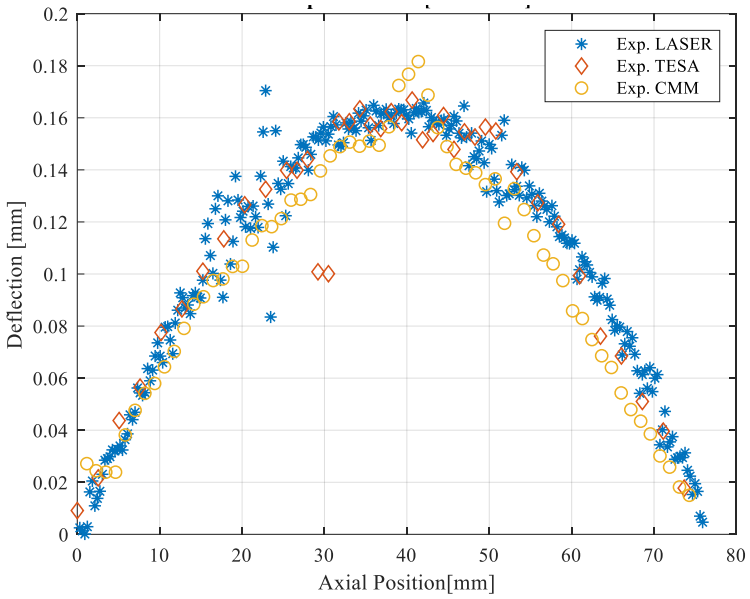

Figure 6-53: Experimental results of the deflection of the laminated stack in the small test setup.

3D magnetic simulation generated in JMAG is used to calculate the forces applied to the components in the active region. Figure 6-54 shows the force values applied to cage laminations at the position with highest rate of forces. Magnetic loads applied to each layer of lamination are reported as single quantities. 160 layers are stacked in the test case. As evident, except a few layers at the two ends, the forces in all three directions is similar for all the laminations, which implies that the magnetic field is uniform along the axial length of the stack. The four layers on each end of the laminated stack carry higher loads compared to the middle ones. For the radial direction, positive sign refers to the outward force and negative sign refers to the inward force. For the tangential direction, positive sign refers to the CCW orientation of the force, while the negative sign stands for the CW orientation. For the axial forces, positive sign stands for the forces in +Z direction and the negative sign refers to the forces in -Z direction.

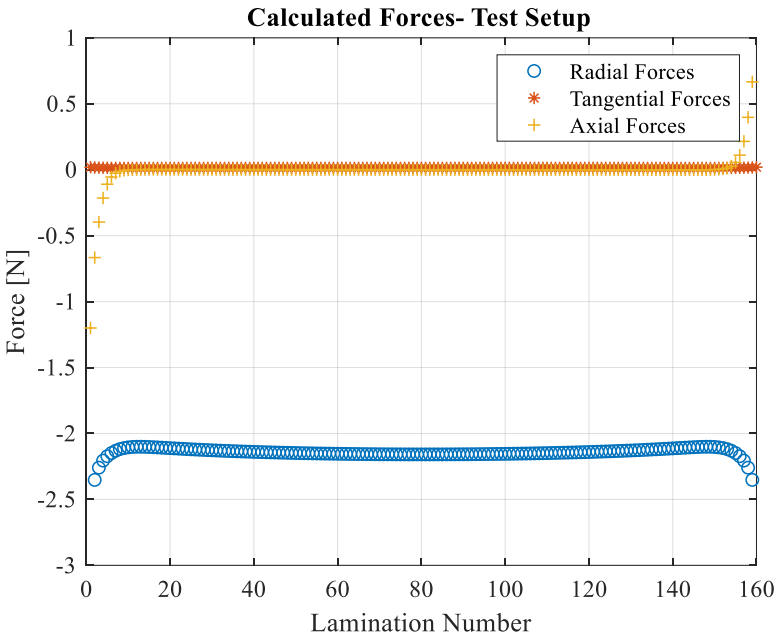

Figure 6-54: Forces applied to the lamination layers in the test setup at the maximum-radial force position.

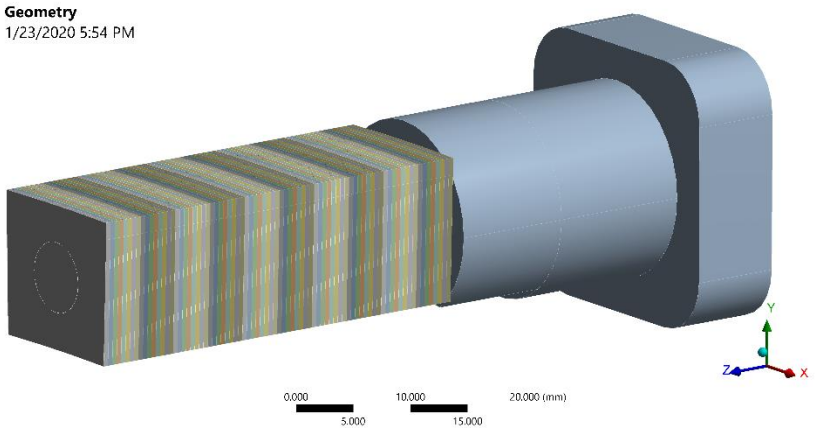

Figure 6-55: 3D FE model of the test setup.

In order to investigate the stiffness of the laminated stack and the strength of the inter-layer bonding, deflection analysis of the test setup is performed. In this study only half of the system, axially, is modeled in ANSYS software to decrease the load of calculations, shown in Figure 6-55. Symmetry condition is then applied to the system on

the midplane. No separation contact type is applied between the rod and the aluminum support. The contact between the rod and the laminations is a combination of no separation on the top part and the frictionless on the bottom part. The glue agent (bonding) between the laminations is defined with the bonded contact type, but the stiffness of this bonding is manually changed to find the closest fit to the experimental results. In this type of modeling, the bonding works like a spring and the bonding factor is the spring stiffness. In this set of simulations, lamination forces are applied as surface force on each layer. The rod forces are also applied to the section inside the active region.

Figure 6-56 shows the deflection analysis of the laminated stack in the test setup. For a better illustration of the experimental results, the range of experimental data points are shown with an orange band. Looking into the results, it turns out that the lamination bonding agent is neither too strong to be considered as a fully rigid contact, nor too weak to be approximated with free-sliding contact (no contact). Contact stiffness factors of the range [1e-4, 1.5e-4] (unitless) result in deflection values in agreement with the experimental results, considering the minimum 0.01 mm of tolerances for measurement devices. This range is closer to the no-contact zone rather than solid contact zone, which implies that the bonding agent between the lamination layers does not provide much stiffness for the stack against bending forces and deflection. Closeness ratio of the experimental stiffness to each zone (no-contact zone vs solid-contact zone) is 3 to 1.

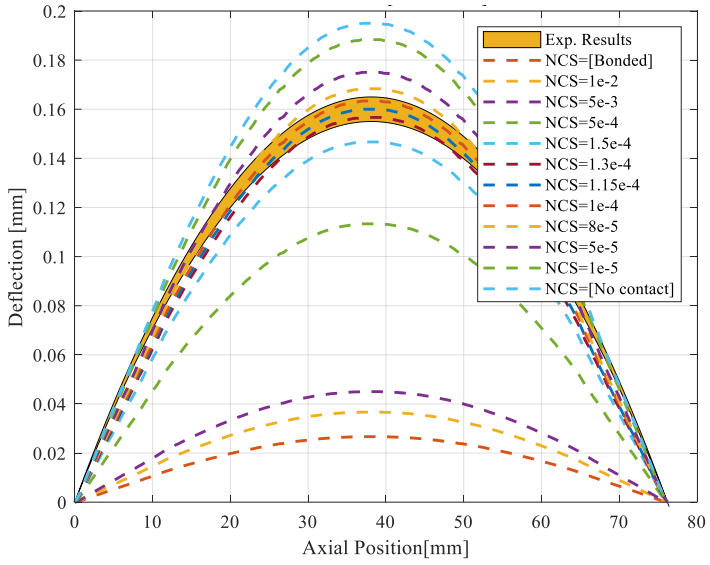

Figure 6-56: Comparison of the FE results of deflection analysis with experimental results.

6.4 ASSEMBLY

1. Inner Assembly (MSMG-stage1)

The assembly process for inner rotor of the MSMG design is axial approach. In this approach, lamination stacks are installed first, then magnets are inserted one at a time and after finishing a row, a support ring is located and next rows follows the same procedure. This process is shown in Figure 6-57. The force analysis of the magnet in the assembly process is shown in Figure 6-58. It is obvious that the highest forces are tangential forces, which means magnets tend to attach to the nearest lamination stack. So, a guide for magnets is required to prevent undesired contact between magnets and laminations. Figure 6-59 shows the designed magnet guide for the inner rotor assembly, and the assembly procedure.

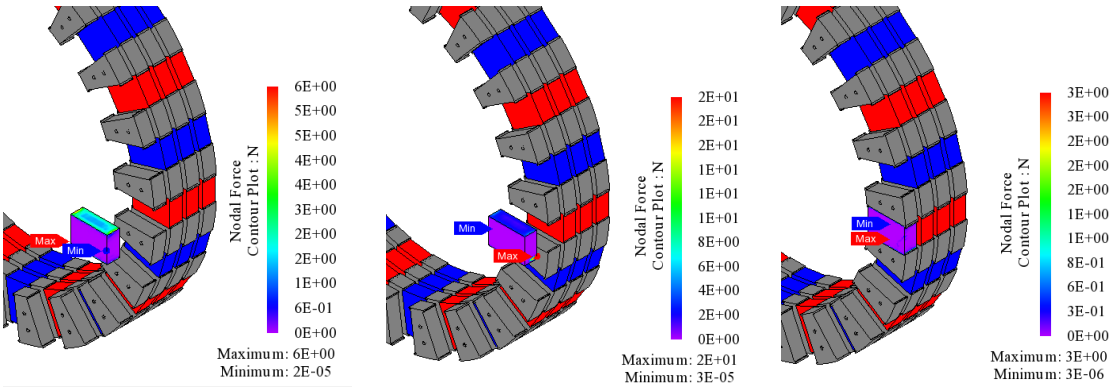

Figure 6-57: Axial assembly of the inner rotor in MSMG design.

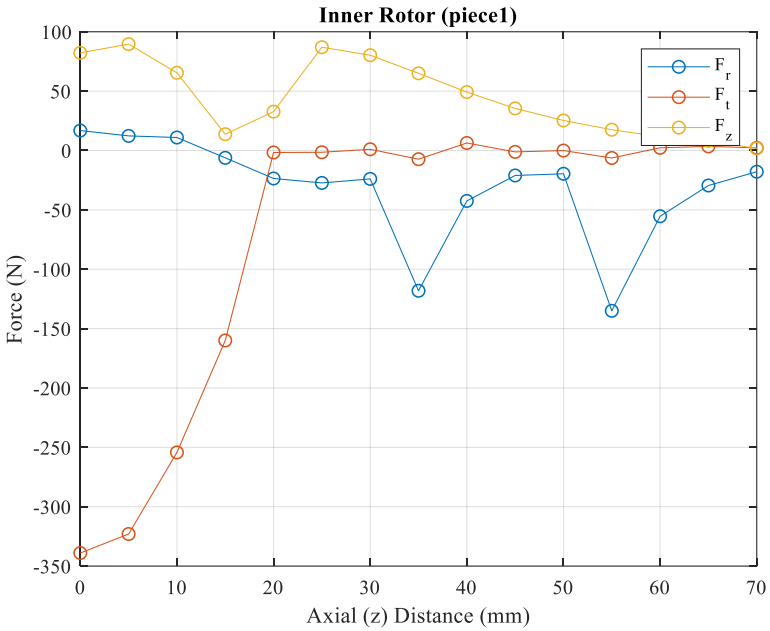

Figure 6-58: Force analysis of the inner magnets in the assembly process.

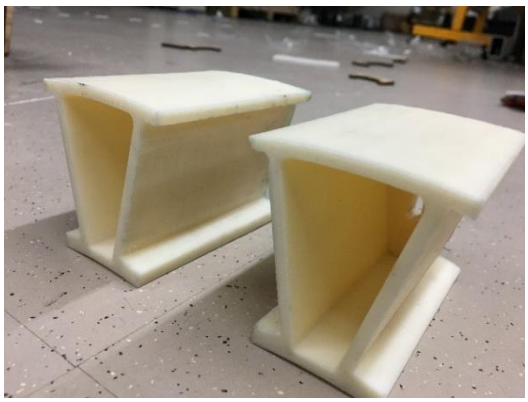

(a)

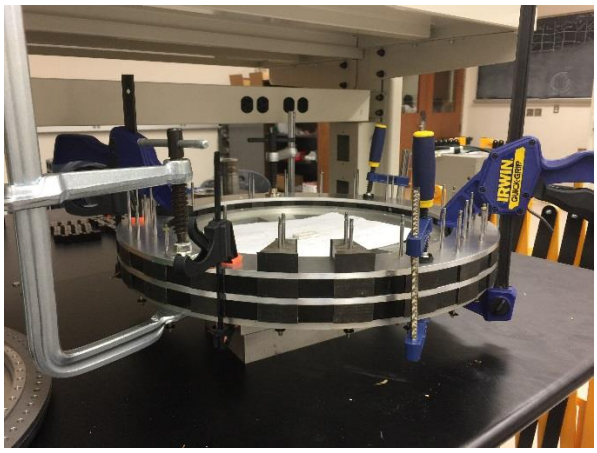
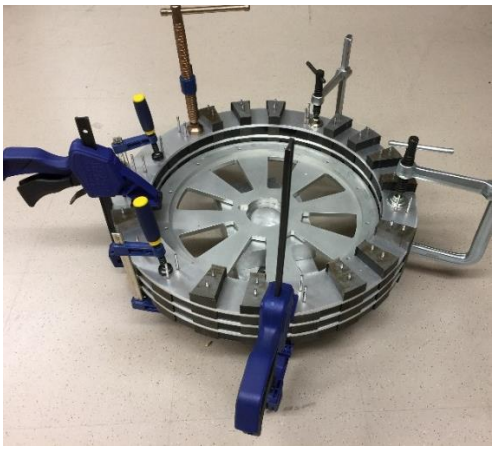

(b)

Figure 6-59: (a) inner rotor assembly guides and (b) inner rotor assembly process for MSMG design.

2. Cage Assembly (MSMG-stage1)

The approach for the cage rotor assembly in MSMG is radial approach. Schematic representation of the assembly process of cage laminations is shown in Figure 6-60. Force analysis of the lamination stack during assembly process is presented in Figure 6-61. As shown, axial and tangential forces are negligible during assembly, while radial forces are remarkable. In order to secure the lamination stack against radial forces during assembly until the point that supporting rods are inserted and the stack is fixed, wooden supports and thin-layer shims are used. Cage endplates are fixed in position by wooden slide pieces, shown in Figure 6-62(a). Cage lamination stacks inserts radially, using non-magnetic thin profile shims, shown in Figure 6-62(b), as a separation between inner and cage rotor component in the active region. In the radial approach, non-magnetic pieces are initially fixed in the correct place using rods and laser-cut wooden spacers. Inserting laminate stacks is the next step, followed by ejecting the shims one by one, after fixing the laminations into position.

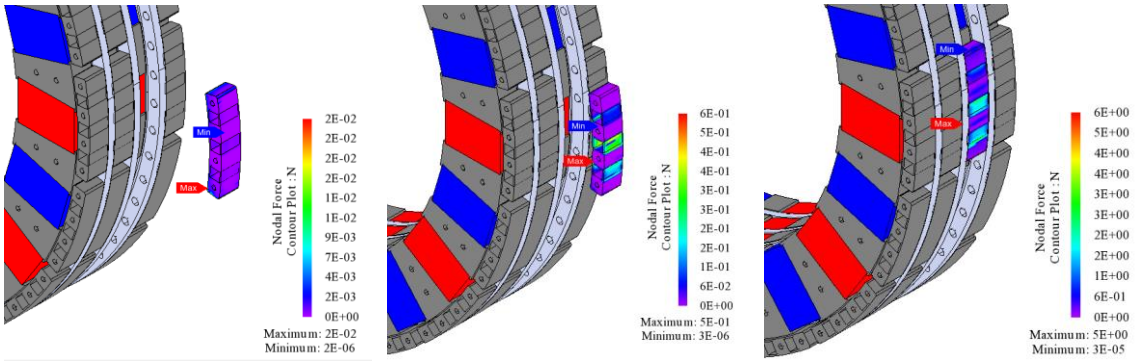

Figure 6-60: Radial assembly of the cage rotor in MSMG stage1 design.

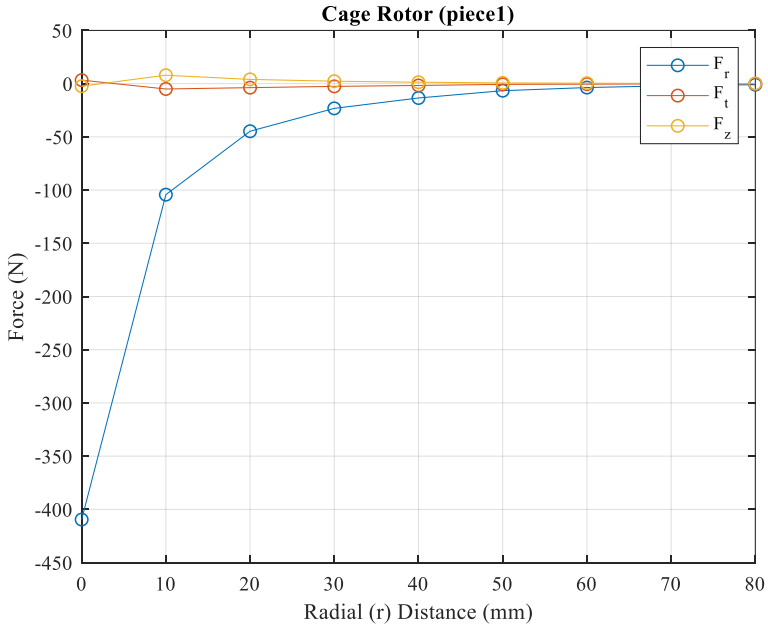

Figure 6-61: Force analysis of the cage magnets in the assembly process.

(a) (b)

Figure 6-62: Cage rotor assembly process, (a) using wooden slide pieces and (b) inserting laminate stacks in presence of multiple shims.

3. Outer Assembly (MSMG-stage1)

The outer rotor is the most challenging to assemble since the number of magnetic components is the highest and it experiences the highest amount of magnetic forces affecting the rotor. To come up with the most robust design for lamination stacks, a thorough study on various topologies was conducted. Two main goals are to be pursued in these designs, including (1) keeping the outer rotor rods away from inner race of the laminations to minimize the negative impacts on the magnetic performance and (2) increasing the stiffness of the laminations to avoid deflections into the air gap between the rotors. Outer rotor laminations are designed so that a set of temporary outer rods are involved to hold the laminations in the correct position without having any permanent rods inserted. With this design, radial approach is conducted as shown in Figure 6-63. Axial, radial and tangential forces that a lamination stack of outer rotor experience during assembly, for MSMG stage1 design, is shown in Figure 6-64. Accordingly, highest forces are radial, but small tangential forces are also applied to the stack. An assembly supporting structure, shown in Figure 6-65, is designed to hold the outer temporary rods in a fixed and unbent shape to complete the assembly process. Then, all four stacks of a single set of laminations are assembled together. Note that assembly structure is designed to be able to be disassembled and reassembled, multiple times.

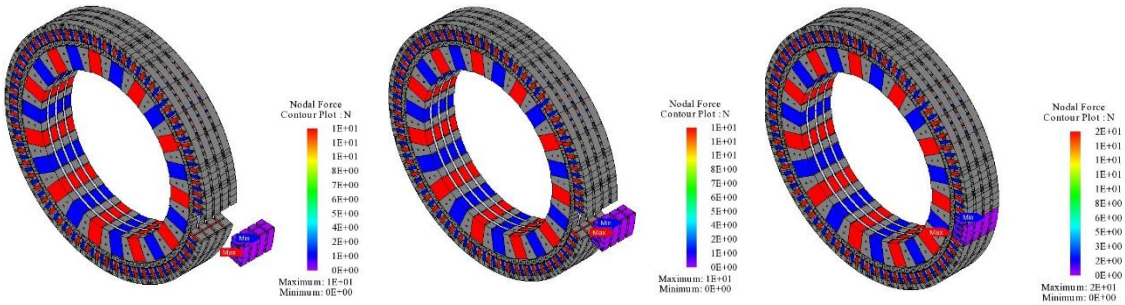

Figure 6-63: Radial assembly of the outer rotor in MSMG stage1 design.

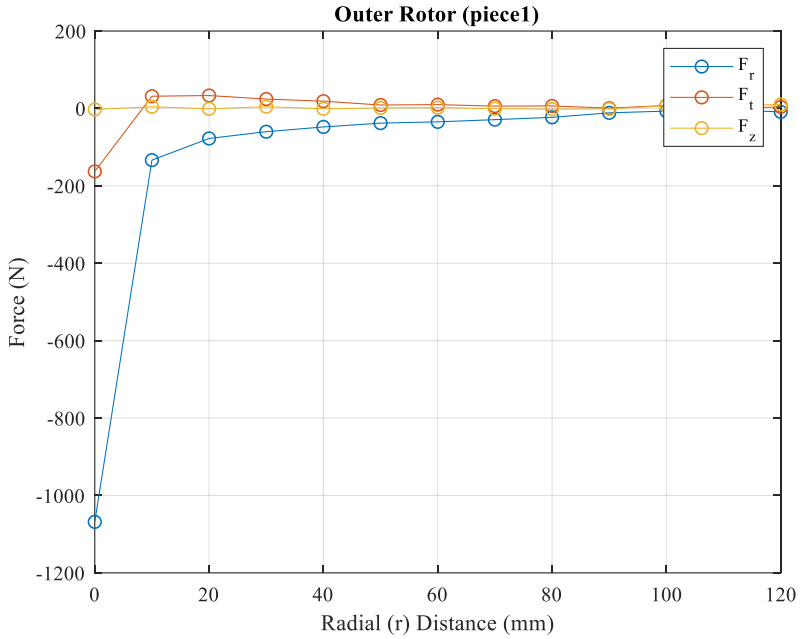

Figure 6-64: Force analysis of the outer magnets in the assembly process.

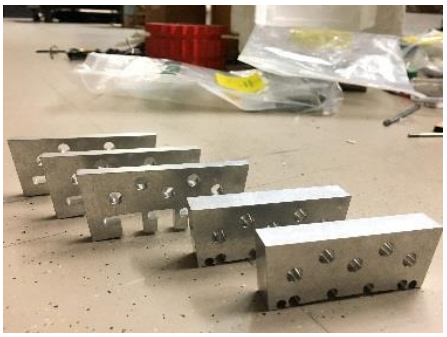

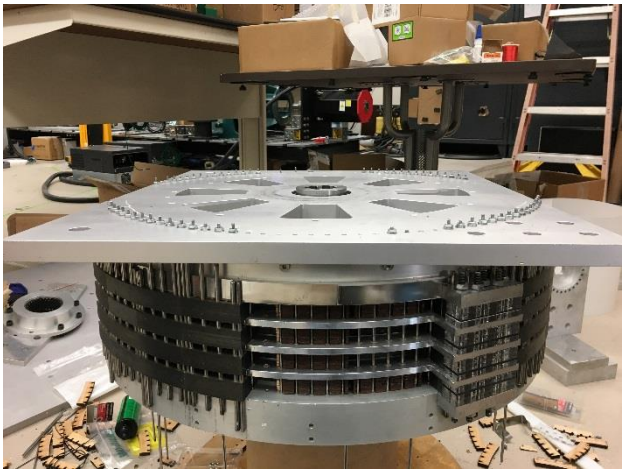

Figure 6-65: Outer rotor assembly support structure, (a) disassembled, (b) assembled, and (c) involved in assembly process.

4. MSMG-stage2

Taking advantage of the experience of assembling the MSMG-stage1, assembly process for the second stage is arranged. For this purpose, the inner rotor is assembled axially, using magnet guides (Figure 6-66), and the cage rotor is assembled radially, using sliding wooden pieces and thin-layered shims (Figure 6-67). The outer rotor assembly is radial, but the process is different. In this process, outer air gap is filled with thin-layered shims, and the stacks are inserted radially. Once the stacks are all inserted and secured on one end, shims are taken out and substituted with thin rods passing through the second endplate. After securing laminations on both ends, thin rods are taken out (Figure 6-68).

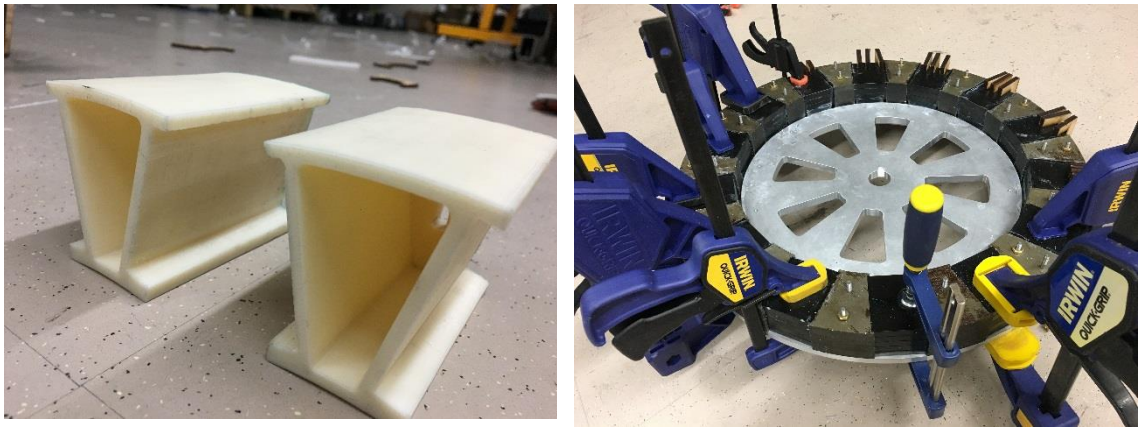

Figure 6-66: Inner rotor assembly process, Second stage of the MSMG design.

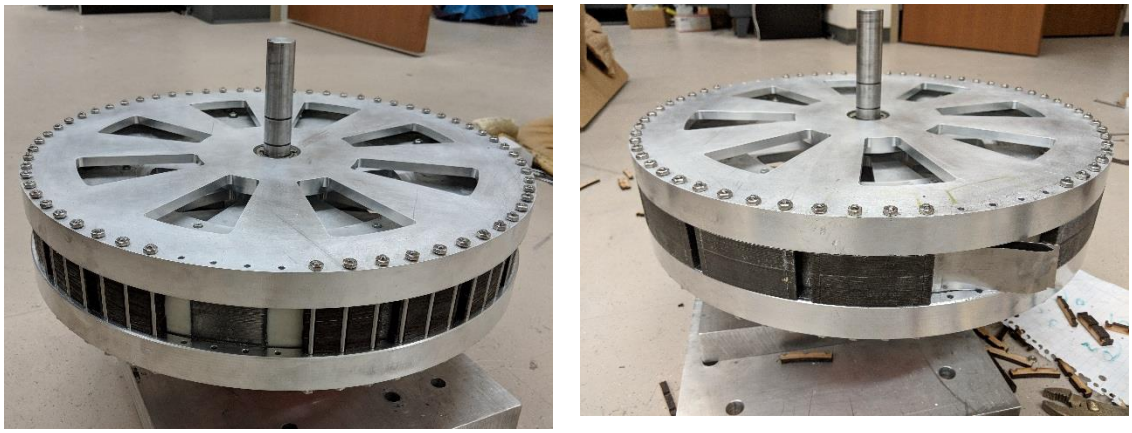

Figure 6-67: Cage rotor assembly process, Second stage of the MSMG design.

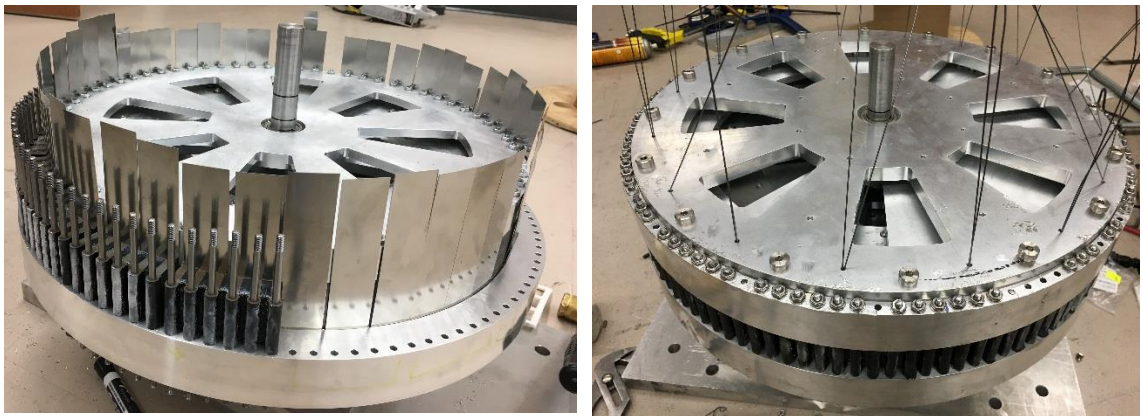

Figure 6-68: Outer rotor assembly process, Second stage of the MSMG design.

5. HSMGG

For this design, inner rotor magnets are inserted one by one, axially (for stage1) and radially (for stage2). The main difference in the assembly process is for the cage and outer rotors. For this design, cage and outer rotors are assembled separately, as shown in Figure 6-69, and support structures, including external rods and circular plates guide the assembled parts into the correct position. Figure 6-70 shows the process for cage and outer rotors, both stage 1 and 2. Figure 6-71 also shows the actual process of assembly for second stage that is in progress.

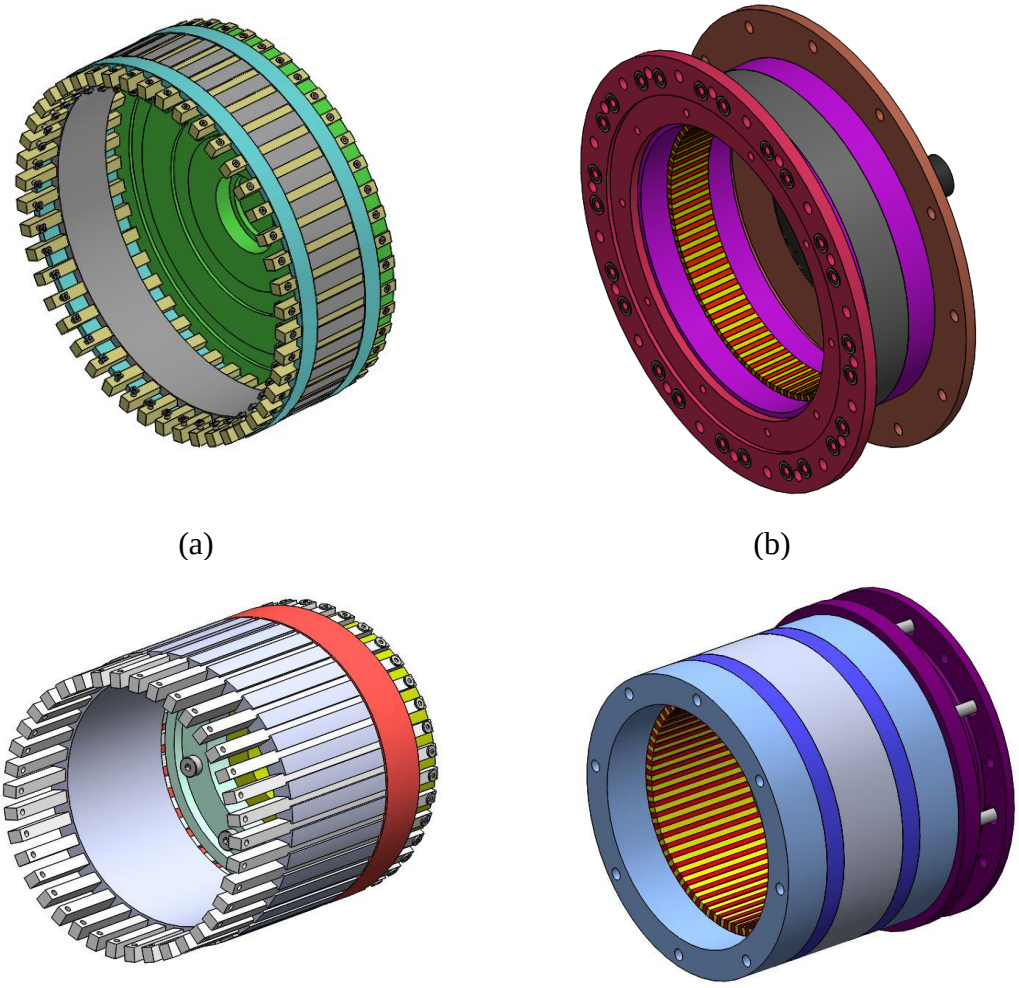

(a) (b)

(c) (d)

Figure 6-69: HSMGG partial assembled parts (a) stage1 cage rotor, (b) stage1 outer rotor, (c) stage2 cage rotor, and (d) stage2 outer rotor.

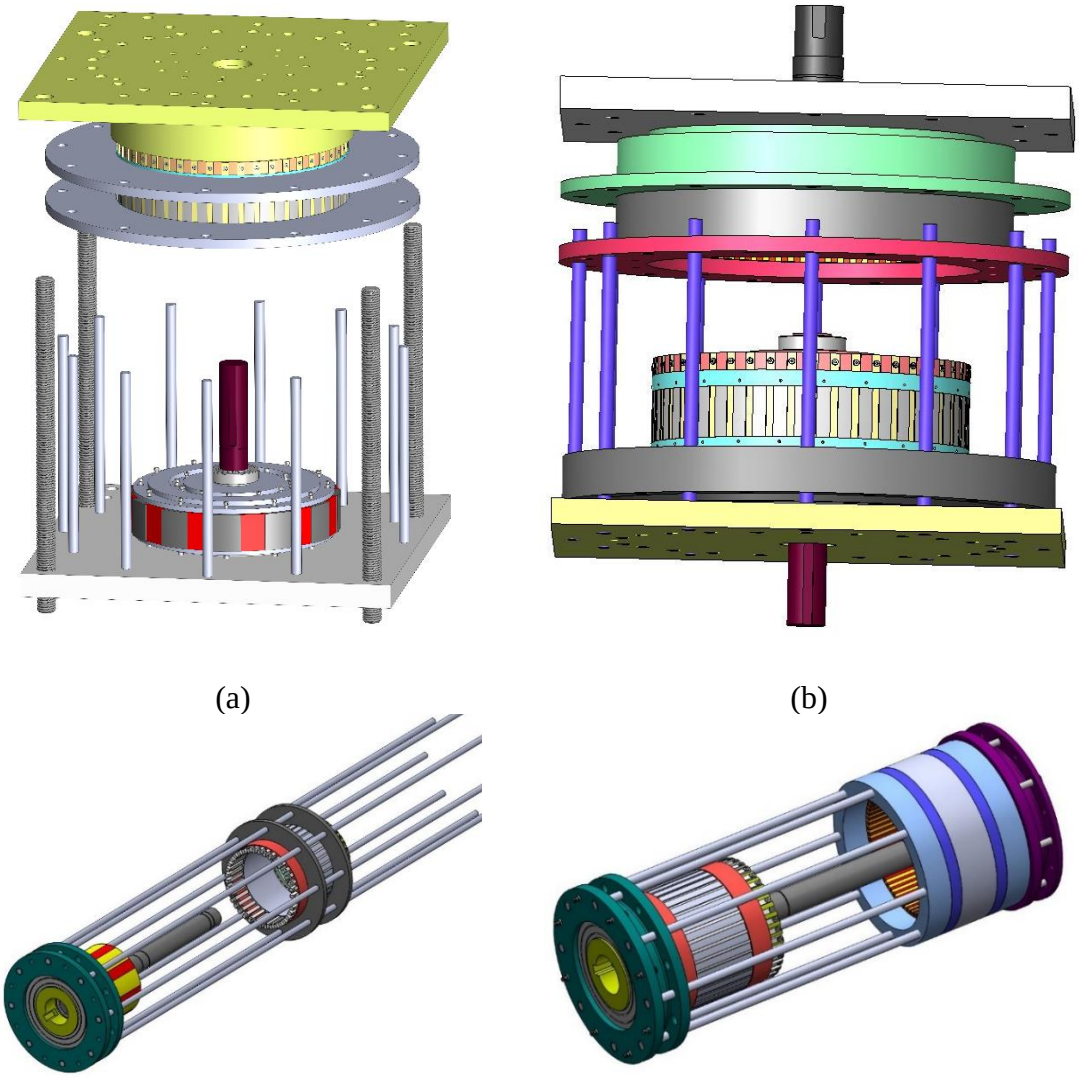

(a) (b)

(c) (d)

Figure 6-70: HSMGG assembly process (a) stage1 cage rotor, (b) stage1 outer rotor, (c) stage2 cage rotor, and (d) stage2 outer rotor.

(a)

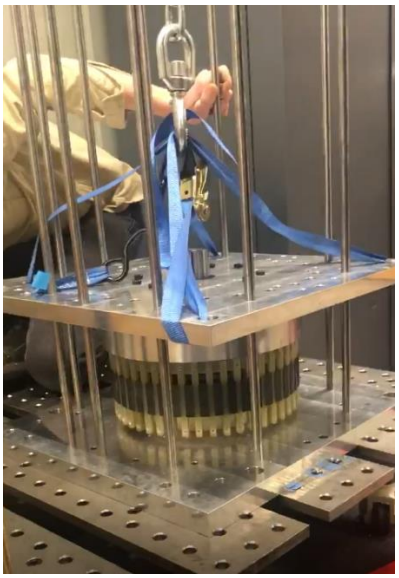

(b)

(c)

(d)

(e)

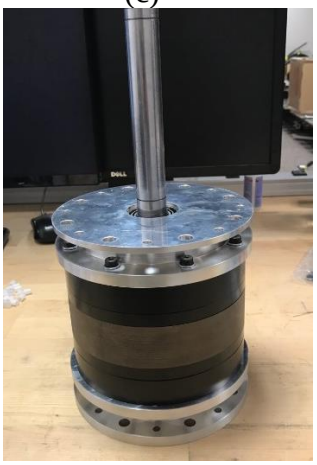

(f)

Figure 6-71: Actual process of the assembly for HSMGG design that is in progress, (a), (b) and (c) assembly of the stage 1 and (d), (e) and (f) assembly of the stage 2.

CHAPTER 7: CONCLUSION

Magnetic gears (MG) are introduced as an alternative for the mechanical gearboxes due to the inherent non-contact torque transmission capability. This is of higher importance in applications with difficult and costly accessibility for the frequent maintenance or replacement of transmission components, such as wind turbines, offshore turbines, marine hydrokinetic applications, etc. Despite the promising contactless feature of the MG's, this technology is still moving up the technology readiness level from ideas, concepts and small-scale prototypes, but not at industrialized versions yet. The main directions of investigations for scaling-up the MG's are divided into three main categories, i. e. magnetic configuration, structural design and mechanical challenges. In this thesis, two multi-stage scaled-up MG's are designed, analyzed and manufactured, i. e. the multi-stage magnetic gearbox (MSMG) and the hermetically sealed magnetically geared generator (HSMGG), with the purpose of investigating the various mechanical failure modes and design issues, whether in the preprocessing and analysis stage, in the manufacturing and assembly phase, or in the post-production and testing stage.

Structural analysis of the MG components is particularly focused on the supporting components of the active-region parts and the laminated stacks. While the magnetic forces in tangential direction are responsible for the torque transmission, very large radial forces are generated in the system which result in the bending of the parts in the active region. Laminated stacks in the MG's provide notable magnetic advantages compared to the solid steel counterparts, but this advantage comes with a cost, which is much lower stiffness due to the glue bonding agents between the lamination layers. An important contribution of this thesis is the evaluation of the effect of bonding agents on the total stiffness of the laminated

stacks under the bending forces, and the effective way to numerically simulate and model the laminations to achieve the proper characteristics. This analysis goes further to the partial modeling of the laminations and suggestions for the full-setup modeling.

Second area of investigation throughout this thesis is dedicated to the thermal analysis of the MG's. Historically, the lumped capacitance method was employed to investigate the thermal behavior of the MG's, but it is introduced as an imprecise approach for modelling due to the very considerable simplifications, assumptions and neglected details, especially geometric features. Later, the conduction method is used to thermally model the MG's, in which the air between the components is treated as a solid part with thermal specifications of the stationary air. In this thesis, the high-precision convection-conduction method is used to thermally investigate a sub-scale magnetic gear design, validate the results and compare them with the conduction method. It turned out that for the enclosed systems like the sub-scale laminated magnetic gear (LMG), the error of the conduction method is not very considerable compared to the convection-conduction method. This conclusion would not apply for systems with inlet and outlet airflow. For such systems, the coupled (convection-conduction) method can yield more reliable results.

The resulting contributions of this thesis in the mechanical design of the MG's can be categorized into three sections. First, the design of the laminated stack, for which different models are investigated based on the positioning of the connecting bridges, both magnetically and mechanically. Second, the effect of the loss analysis, edge effects and the thermal analysis are used to further investigate the material selection in the active region and introducing the boundary of the region in which using the conductive materials are not suggested. Third, the assembly-informed design of the MG's is emphasized. Scaled-up

designs come with several undeniable mechanical and manufacturing challenges which all affect the design of the system and the appropriate assembly approach. The limitations for the manufacturing of the laminations in large scales, the manufacturing tolerances, the poor machinability of some non-conductive materials such as Garolite (G10), the strong magnetic forces to dealing with during assembly considering the minimal air gap between the rotors (usually between 0.5mm and 1mm for these designs) are a few examples of the mechanical and manufacturing challenges that were addressed in the design of these MG's.

An initial assessment of the cost of the manufacturing of the two proposed systems identified magnets, laminated rotor stacks, purchased components, and machined components as the primary categories. Magnetic gears require magnets by definition, and they have accounted for <10% of the material costs on the prototypes produced. The magnetic material required increases with the torque rating and the cost per mass has fluctuated in recent years based on increased demand and intermittently tight control of the supply from China. A larger portion (40-50%) of the cost is linked to the manufacturing of laminated cores, which are currently manufactured through a laser-cutting operation, where the cost depends on the length of the lasering path. For the mass production of laminations, a stamping operation is suggested, in which tooling is manufactured based on the configuration of one lamination, and the actual parts will be made using this tool and a press. This will reduce the manufacturing cost of the laminations dramatically, while maintaining suitable tolerances. Machined parts consist of endplates, shafts and rods, account for 30-50% of the total material costs for the prototypes, depending on the design. The machined parts however were typically produced in quantities of one or two, and larger production runs would result in lower costs based on economies of scale. These savings

were estimated using automated quoting from Xometry (an online manufacturing network) for of the production of key parts in quantities of 5, 10, and 20, which respectively reduced the manufacturing cost per part by 60%, 72%, and 80%. So improvements/efficiencies in the lamination and machining processes would reduce the cost of manufacturing multistage magnetic gearboxes. That said, magnetic gearboxes still struggle to compete with traditional gearboxes, except in applications where the routine maintenance of traditional gearboxes is impossible due to remoteness or inaccessibility.

Suggestions for the structural design and the full assembly modeling in magnetic gears are provided in this study through conducting analysis in five areas of mechanical investigation:

- Structural analysis of the laminations provides a framework for better understanding of the behavior of the laminated stacks under bending forces. The results suggest that the analytical solution over-predict their stiffness, but numerical simulations can be done that match the experimental results.
- Forces during assembly must be considered during the mechanical design of the components as they may be significantly higher than the forces observed during operation.
- Changes in axial field cannot be ignored for higher rotational speeds, where they will cause significant losses through induced eddy currents.
- Loss analysis suggests changes in magnetic configuration, material selection and structural design.
- Thermal analysis detects susceptible structures to excessive temperature rise and thermal deformation.

There are many aspects in which the magnetic gearing technology can be developed. On the thermal analysis aspect, investigating the internal cooling system to provide a forced convection for the MG seems functional. On the mechanical design aspect, modular multi-stage magnetic gearboxes with the capability of changing the gear ratio are an interesting area of research to expand the applications of the MG's.

REFERENCES

[1] "Gear-wheel," US288134A, Nov. 06, 1883.

[2] "Types of Gears | KHK Gears." https://khkgears.net/new/gear_knowledge/introduction_to_gears/types_of_gears.html (accessed Feb. 06, 2020).

[3] P. Lynwander, *Gear Drive Systems: Design and Application*. CRC Press, 2019.

[4] "2019 Economic Impact Analysis of Clean Energy Development in North Carolina," *NC Sustainable Energy Association*, May 14, 2019. https://energync.org/2019-economic-impact-analysis-of-clean-energy-development-in-north-carolina/ (accessed Feb. 13, 2020).

[5] Y. Feng, Y. Qiu, C. J. Crabtree, H. Long, and P. J. Tavner, "Monitoring wind turbine gearboxes," *Wind Energy*, vol. 16, no. 5, pp. 728–740, 2013, doi: 10.1002/we.1521.

[6] M. Nie and L. Wang, "Review of Condition Monitoring and Fault Diagnosis Technologies for Wind Turbine Gearbox," *Procedia CIRP*, vol. 11, pp. 287–290, Jan. 2013, doi: 10.1016/j.procir.2013.07.018.

[7] J. P. Salameh, S. Cauet, E. Etien, A. Sakout, and L. Rambault, "Gearbox condition monitoring in wind turbines: A review," *Mech. Syst. Signal Process.*, vol. 111, pp. 251–264, Oct. 2018, doi: 10.1016/j.ymssp.2018.03.052.

[8] B. Hahn, M. Durstewitz, and K. Rohrig, "Reliability of Wind Turbines," p. 4.

[9] J. Carroll, A. McDonald, and D. McMillan, "Failure rate, repair time and unscheduled O&M cost analysis of offshore wind turbines," *Wind Energy*, vol. 19, no. 6, pp. 1107–1119, 2016, doi: 10.1002/we.1887.

[10] R. Errichello, "How to analyze gear failures," *Pract. Fail. Anal.*, p. 9.

[11] R. Errichello, "How to analyze gear failures," *Pract. Fail. Anal.*, vol. 2, no. 6, pp. 8–16, Dec. 2002, doi: 10.1007/BF02715492.

[12] O. Asi, "Fatigue failure of a helical gear in a gearbox," *Eng. Fail. Anal.*, vol. 13, no. 7, pp. 1116–1125, Oct. 2006, doi: 10.1016/j.engfailanal.2005.07.020.

[13] "Tooth Flank Fracture - Basic Principles and Calculation Model for a Sub-Surface-Initiated Fatigue Failure Mode of Case-Hardened Gears : Gear Technology August 2015." https://www.geartechnology.com/articles/0815/Tooth_Flank_Fracture_-_Basic_Principles_and_Calculation_Model_for_a_Sub-Surface-Initiated_Fatigue_Failure_Mode_of_Case-Hardened_Gears/ (accessed Apr. 23, 2019).

[14] "Differential Failure Analysis," *West Coast Differentials*. https://www.differentials.com/technical-help-2/failure-analysis/ (accessed Apr. 23, 2019).

[15] “Gearbox lubrication: What are the best methods?” https://www.motioncontroltips.com/gearbox-lubrication-best-methods/ (accessed Apr. 23, 2019).

[16] W. Musial and S. Butterfield, “Improving Wind Turbine Gearbox Reliability: Preprint,” p. 13.

[17] B. McGilton, R. Crozier, A. McDonald, and M. Mueller, “Review of magnetic gear technologies and their applications in marine energy,” *IET Renew. Power Gener.*, vol. 12, no. 2, pp. 174–181, Nov. 2017, doi: 10.1049/iet-rpg.2017.0210.

[18] H. Baninajar, J. Z. Bird, S. Modaresahmadi, and W. Williams, “Electromagnetic and Mechanical Design of a Hermetically Sealed Magnetic Gear for a Marine Hydrokinetic Generator,” in *2018 IEEE Energy Conversion Congress and Exposition (ECCE)*, Sep. 2018, pp. 4987–4993, doi: 10.1109/ECCE.2018.8557386.

[19] T. J. E. Miller, “Brushless permanent-magnet and reluctance motor drives,” Jan. 1989, Accessed: Apr. 22, 2019. [Online]. Available: https://www.osti.gov/biblio/6911525.

[20] J. J. Scheidler, V. M. Asnani, and T. F. Tallerico, “NASA’s Magnetic Gearing Research for Electrified Aircraft Propulsion,” in *2018 AIAA/IEEE Electric Aircraft Technologies Symposium (EATS)*, Jul. 2018, pp. 1–12.

[21] C. G. Armstrong, “Power-transmitting device,” US687292A, Nov. 26, 1901.

[22] A. H. Neuland, “Apparatus for transmitting power,” US1171351A, Feb. 08, 1916.

[23] H. M. Stoller, “Magnetic gearing,” US1337732A, Apr. 20, 1920.

[24] H. T. Faus, “Magnet gearing,” US2243555A, May 27, 1941.

[25] H. T. Faus, “Magnetic transmission,” US2371511A, Mar. 13, 1945.

[26] J. T. B. Martin, “Magnetic transmission,” US3378710A, Apr. 16, 1968.

[27] H. P. Schlaeppi, “Magnetic gears,” US3382386A, May 07, 1968.

[28] D. E. Hesmondhalgh and D. Tipping, “A multielement magnetic gear,” *IEE Proc. B - Electr. Power Appl.*, vol. 127, no. 3, pp. 129–138, May 1980, doi: 10.1049/ip-b.1980.0017.

[29] K. Tsurumoto and S. Kikuchi, “A new magnetic gear using permanent magnet,” *IEEE Trans. Magn.*, vol. 23, no. 5, pp. 3622–3624, Sep. 1987, doi: 10.1109/TMAG.1987.1065208.

[30] K. Ikuta, S. Makita, and S. Arimoto, “Non-contact magnetic gear for micro transmission mechanism,” in *[1991] Proceedings. IEEE Micro Electro Mechanical Systems*, Jan. 1991, pp. 125–130, doi: 10.1109/MEMSYS.1991.114782.

[31] S. Kikuchi and K. Tsurumoto, “Design and characteristics of a new magnetic worm gear using permanent magnet,” *IEEE Trans. Magn.*, vol. 29, no. 6, pp. 2923–2925, Nov. 1993, doi: 10.1109/20.280916.

[32] S. Kikuchi and K. Tsurumoto, “Trial construction of a new magnetic skew gear using permanent magnet,” *IEEE Trans. Magn.*, vol. 30, no. 6, pp. 4767–4769, Nov. 1994, doi: 10.1109/20.334216.

[33] R. E. Clark, D. S. Smith, P. H. Mellor, and D. Howe, “Design optimisation of moving-magnet actuators for reciprocating electro-mechanical systems,” *IEEE Trans. Magn.*, vol. 31, no. 6, pp. 3746–3748, Nov. 1995, doi: 10.1109/20.489758.

[34] Jiabin Wang, G. W. Jewell, and D. Howe, “A general framework for the analysis and design of tubular linear permanent magnet machines,” *IEEE Trans. Magn.*, vol. 35, no. 3, pp. 1986–2000, May 1999, doi: 10.1109/20.764898.

[35] F. T. Joergensen, T. O. Andersen, and P. O. Rasmussen, “The cycloid permanent magnetic gear,” in *Conference Record of the 2006 IEEE Industry Applications Conference Forty-First IAS Annual Meeting*, Oct. 2006, vol. 1, pp. 373–378, doi: 10.1109/IAS.2006.256549.

[36] K. Atallah and D. Howe, “A novel high-performance magnetic gear,” *IEEE Trans. Magn.*, vol. 37, no. 4, pp. 2844–2846, Jul. 2001, doi: 10.1109/20.951324.

[37] K. Atallah, J. Wang, and D. Howe, “A high-performance linear magnetic gear,” *J. Appl. Phys.*, vol. 97, no. 10, p. 10N516, May 2005, doi: 10.1063/1.1853900.

[38] S. Mezani, K. Atallah, and D. Howe, “A high-performance axial-field magnetic gear,” *J. Appl. Phys.*, vol. 99, no. 8, p. 08R303, Apr. 2006, doi: 10.1063/1.2158966.

[39] S. Kikuchi and K. Tsurumoto, “Design and characteristics of a new magnetic worm gear using permanent magnet,” *IEEE Trans. Magn.*, vol. 29, no. 6, pp. 2923–2925, Nov. 1993, doi: 10.1109/20.280916.

[40] Y. Wang, M. Filippini, N. Bianchi, and P. Alotto, “A Review on Magnetic Gears: Topologies, Computational Models, and Design Aspects,” *IEEE Trans. Ind. Appl.*, vol. 55, no. 5, pp. 4557–4566, Sep. 2019, doi: 10.1109/TIA.2019.2916765.

[41] K. Li and J. Z. Bird, “A Review of the Volumetric Torque Density of Rotary Magnetic Gear Designs,” in *2018 XIII International Conference on Electrical Machines (ICEM)*, Sep. 2018, pp. 2016–2022, doi: 10.1109/ICELMACH.2018.8507059.

[42] P. M. Tlali, R.-J. Wang, and S. Gerber, “Magnetic gear technologies: A review,” in *2014 International Conference on Electrical Machines (ICEM)*, Sep. 2014, pp. 544–550, doi: 10.1109/ICELMACH.2014.6960233.

[43] J. Wang, K. Atallah, and W. Wang, “Analysis of a Magnetic Screw for High Force Density Linear Electromagnetic Actuators,” *IEEE Trans. Magn.*, vol. 47, no. 10, pp. 4477–4480, Oct. 2011, doi: 10.1109/TMAG.2011.2157464.

[44] M. C. Gardner, M. Johnson, and H. A. Toliyat, “Comparison of Surface Permanent Magnet Coaxial and Cycloidal Radial Flux Magnetic Gears,” *2018 IEEE Energy Convers. Congr. Expo. ECCE*, pp. 5005–5012, 2018, doi: 10.1109/ecce.2018.8558234.

[45] B. Ackermann, “Magnetic drive arrangement,” US5994809A, Nov. 30, 1999.

[46] O. S. Chirilă, D. Stoia, M. Cernat, and K. Hamayer, "High-performance magnetic gears topologies," in *2010 12th International Conference on Optimization of Electrical and Electronic Equipment*, May 2010, pp. 1091–1096, doi: 10.1109/OPTIM.2010.5510496.

[47] H. Y. Wong, J. Z. Bird, S. Modaresahmadi, and W. Williams, "Comparative Analysis of a Coaxial Magnetic Gear With a Flux Concentration Rotor and Consequent Pole Rotor Typology," *IEEE Trans. Magn.*, vol. 54, no. 11, pp. 1–5, Nov. 2018, doi: 10.1109/TMAG.2018.2854864.

[48] D. H. Wong, S. Modaresahmadi, J. Z. Bird, and W. Williams, "Comparative Analysis of a Coaxial Magnetic Gearbox with a Flux Concentration Halbach Rotor and Consequent Pole Rotor Typology.," in *2018 IEEE International Magnetics Conference (INTERMAG)*, Apr. 2018, pp. 1–2, doi: 10.1109/INTMAG.2018.8508433.

[49] "Magnetic gear," *Wikipedia*. Dec. 24, 2019, Accessed: Feb. 08, 2020. [Online]. Available: https://en.wikipedia.org/w/index.php?title=Magnetic_gear&oldid=932223339.

[50] D. Som *et al.*, "Analysis and Testing of a Coaxial Magnetic Gearbox With Flux Concentration Halbach Rotors," *IEEE Trans. Magn.*, vol. 53, no. 11, pp. 1–6, Nov. 2017, doi: 10.1109/TMAG.2017.2715799.

[51] W. Li and K.-T. Chau, "Analytical Field Calculation for Linear Tubular Magnetic Gears Using Equivalent Anisotropic Magnetic Permeability," *Prog. Electromagn. Res.*, vol. 127, pp. 155–171, 2012, doi: 10.2528/PIER12030301.

[52] "Modeling Magnetic Gears in COMSOL Multiphysics," *COMSOL Multiphysics*. https://www.comsol.com/blogs/modeling-magnetic-gears-in-comsol-multiphysics/ (accessed Feb. 08, 2020).

[53] M.-C. Tsai and L.-H. Ku, "3-D Printing-Based Design of Axial Flux Magnetic Gear for High Torque Density," *IEEE Trans. Magn.*, vol. 51, no. 11, pp. 1–4, Nov. 2015, doi: 10.1109/TMAG.2015.2435817.

[54] X. Yin, P.-D. Pfister, and Y. Fang, "A Novel Magnetic Gear: Toward a Higher Torque Density," *IEEE Trans. Magn.*, vol. 51, no. 11, pp. 1–4, Nov. 2015, doi: 10.1109/TMAG.2015.2436058.

[55] D. Zhu, F. Yang, Y. Du, F. Xiao, and Z. Ling, "An Axial-Field Flux-Modulated Magnetic Gear," *IEEE Trans. Appl. Supercond.*, vol. 26, no. 4, pp. 1–5, Jun. 2016, doi: 10.1109/TASC.2016.2541302.

[56] Y. Liu, S. L. Ho, and W. N. Fu, "A Novel Magnetic Gear With Intersecting Axes," *IEEE Trans. Magn.*, vol. 50, no. 11, pp. 1–4, Nov. 2014, doi: 10.1109/TMAG.2014.2325608.

[57] S. Peng, W. N. Fu, and S. L. Ho, "A Novel Triple-Permanent-Magnet-Excited Hybrid-Flux Magnetic Gear and Its Design Method Using 3-D Finite Element Method," *IEEE Trans. Magn.*, vol. 50, no. 11, pp. 1–4, Nov. 2014, doi: 10.1109/TMAG.2014.2327068.

[58] W. Bomela, J. Z. Bird, and V. M. Acharya, “The Performance of a Transverse Flux Magnetic Gear,” *IEEE Trans. Magn.*, vol. 50, no. 1, pp. 1–4, Jan. 2014, doi: 10.1109/TMAG.2013.2277431.

[59] X. Li, K.-T. Chau, M. Cheng, and W. Hua, “Comparison of Magnetic-Geared Permanent-Magnet Machines,” *Prog. Electromagn. Res.*, vol. 133, pp. 177–198, 2013, doi: 10.2528/PIER12080808.

[60] K. Li, “An Investigation into the Torque Capabilities of High Gear Ratio Magnetic Gearboxes,” Ph.D., The University of North Carolina at Charlotte, United States -- North Carolina, 2018.

[61] D. Som *et al.*, “Analysis and Testing of a Coaxial Magnetic Gearbox With Flux Concentration Halbach Rotors,” *IEEE Trans. Magn.*, vol. 53, no. 11, pp. 1–6, Nov. 2017, doi: 10.1109/TMAG.2017.2715799.

[62] K. Li, J. Wright, S. Modaresahmadi, D. Som, W. Williams, and J. Z. Bird, “Designing the first stage of a series connected multistage coaxial magnetic gearbox for a wind turbine demonstrator,” in *2017 IEEE Energy Conversion Congress and Exposition (ECCE)*, Oct. 2017, pp. 1247–1254, doi: 10.1109/ECCE.2017.8095932.

[63] M. B. Kouhshahi, J. Z. Bird, V. Acharya, K. Li, M. Calvin, and W. Williams, “An axial flux-focusing magnetically geared motor,” in *2017 IEEE Energy Conversion Congress and Exposition (ECCE)*, Oct. 2017, pp. 307–313, doi: 10.1109/ECCE.2017.8095797.

[64] C.-S. Gim, E.-J. Park, S.-Y. Jung, and Y.-J. Kim, “Torque Characteristic Analysis of Coaxial Magnetic Gear According to Fillet Parameter of Pole Piece,” in *2018 21st International Conference on Electrical Machines and Systems (ICEMS)*, Oct. 2018, pp. 2557–2560, doi: 10.23919/ICEMS.2018.8549422.

[65] L. Jing and Z. Huang, “The Effect of Number of Pole Pairs on Torque Ripple of Magnetic Gear,” *Prog. Electromagn. Res.*, vol. 86, pp. 115–123, 2019, doi: 10.2528/PIERM19082702.

[66] Y.-C. Wu, W.-T. Tseng, and Y.-T. Chen, “Torque Ripple Suppression in an External-Meshed Magnetic Gear Train,” *Adv. Mech. Eng.*, vol. 5, p. 178909, Jan. 2013, doi: 10.1155/2013/178909.

[67] S. Modaresahmadi, W. Williams, K. Li, J. Wright, and J. Bird, “Mechanical analysis of a multistage magnetic gearbox,” in *International. Mechanical Engineering Congress & Expo*, 2017.

[68] S. Modaresahmadi, C. Nichols, and W. Williams, “Mechanical Design of Magnetic Gearboxes Optimized for Assembly,” presented at the ASME 2018 International Mechanical Engineering Congress and Exposition, Jan. 2019, doi: 10.1115/IMECE2018-86878.

[69] K. Li, S. Modaresahmadi, W. B. Williams, J. D. Wright, D. Som, and J. Z. Bird, “Designing and Experimentally Testing a Magnetic Gearbox for a Wind Turbine Demonstrator,” *IEEE Trans. Ind. Appl.*, vol. 55, no. 4, pp. 3522–3533, Jul. 2019, doi: 10.1109/TIA.2019.2905838.

[70] “Eddy Current Loss - an overview | ScienceDirect Topics.” https://www.sciencedirect.com/topics/engineering/eddy-current-loss (accessed Feb. 10, 2020).

[71] M. Fukuoka, K. Nakamura, and O. Ichinokura, “Loss analysis and performance improvement of trial SPM type magnetic gear,” in *2013 15th European Conference on Power Electronics and Applications (EPE)*, Sep. 2013, pp. 1–8, doi: 10.1109/EPE.2013.6634388.

[72] S. Modaresahmadi, J. Khalesi, J. Kadel, and W. Williams, “Thermal Analysis of a Subscale Flux Focusing Magnetic Gearbox,” presented at the ASME 2018 International Mechanical Engineering Congress and Exposition, Jan. 2019, doi: 10.1115/IMECE2018-86876.

[73] K. Li, S. Modaresahmadi, W. Williams, J. Wright, J. Bird, and D. Som, “Designing and Experimentally Testing a Magnetic Gearbox for a Wind Turbine Demonstrator,” *IEEE Trans. Ind. Appl.*, pp. 1–1, 2019, doi: 10.1109/TIA.2019.2905838.

[74] D. E. Hesmondhalgh and D. Tipping, “A multielement magnetic gear,” *IEE Proc. B - Electr. Power Appl.*, vol. 127, no. 3, pp. 129–138, May 1980, doi: 10.1049/ip-b.1980.0017.

[75] J. F. Charpentier and G. Lemarquand, “Mechanical behavior of axially magnetized permanent-magnet gears,” *IEEE Trans. Magn.*, vol. 37, no. 3, pp. 1110–1117, May 2001, doi: 10.1109/20.920485.

[76] R. Zanis, A. Borisavljevic, J. W. Jansen, and E. A. Lomonova, “Iron loss investigation of miniaturized magnetic gears having solid cores,” in *2014 17th International Conference on Electrical Machines and Systems (ICEMS)*, Oct. 2014, pp. 3078–3082, doi: 10.1109/ICEMS.2014.7014023.

[77] K. K. Uppalapati and J. Z. Bird, “An Iterative Magnetomechanical Deflection Model for a Magnetic Gear,” *IEEE Trans. Magn.*, vol. 50, no. 2, pp. 245–248, Feb. 2014, doi: 10.1109/TMAG.2013.2283018.

[78] D. Z. Abdelhamid and A. M. Knight, “The Effect of Modulating Ring Design on Magnetic Gear Torque,” *IEEE Trans. Magn.*, vol. 53, no. 11, pp. 1–4, Nov. 2017, doi: 10.1109/TMAG.2017.2716920.

[79] J. Lee, D. Kim, Y. Kim, and S. Jung, “Study on topology of magnetic gear considering shape of pole piece,” in *2017 20th International Conference on Electrical Machines and Systems (ICEMS)*, Aug. 2017, pp. 1–4, doi: 10.1109/ICEMS.2017.8056489.

[80] Y. Zhang, M. Cheng, and P. Pillay, “Magnetic Characteristics and Excess Eddy Current Losses,” in *2009 IEEE Industry Applications Society Annual Meeting*, Oct. 2009, pp. 1–5, doi: 10.1109/IAS.2009.5324814.

[81] B. Yang, “Development of thermal models for permanent-magnet traction motors,” Royal Institute of Technology, Stockholm, Sweden, Tech. Rep., 2009.

[82] J.-H. Jang, H.-C. Chiu, W.-M. Yan, M. C. Tsai, and P.-Y. Wang, “Numerical study on electromagnetics and thermal cooling of a switched reluctance motor,” *Case Stud. Therm. Eng.*, vol. 6, pp. 16–27, Sep. 2015, doi: 10.1016/j.csite.2015.05.001.

[83] A. H. Bonnett, “Operating temperature considerations and performance characteristics for IEEE 841 motors,” in *Record of Conference Papers. Industry Applications Society Forty-Seventh Annual Conference. 2000 Petroleum and Chemical Industry Technical Conference (Cat. No.00CH37112)*, Sep. 2000, pp. 77–89, doi: 10.1109/PCICON.2000.882764.

[84] C.-C. Chang, Y.-F. Kuo, J.-C. Wang, and S.-L. Chen, “Air cooling for a large-scale motor,” *Appl. Therm. Eng.*, vol. 30, no. 11, pp. 1360–1368, Aug. 2010, doi: 10.1016/j.applthermaleng.2010.02.023.

[85] K. N. Srinivas and R. Arumugam, “Thermal characterization through finite element analysis of the switched reluctance motor,” in *Proceedings of IEEE Region 10 International Conference on Electrical and Electronic Technology. TENCON 2001 (Cat. No.01CH37239)*, Aug. 2001, vol. 2, pp. 819–823 vol.2, doi: 10.1109/TENCON.2001.949707.

[86] H. Li, “Cooling of a permanent magnet electric motor with a centrifugal impeller,” *Int. J. Heat Mass Transf.*, vol. 53, no. 4, pp. 797–810, Jan. 2010, doi: 10.1016/j.ijheatmasstransfer.2009.09.022.

[87] X. Hao and X. Zhu, “Forced Responses of the Parametric Vibration System for the Electromechanical Integrated Magnetic Gear,” *Shock and Vibration*, 2015. https://www.hindawi.com/journals/sv/2015/572937/abs/ (accessed Apr. 23, 2019).

[88] S. Modaresahmadi, K. Li, W. B. Williams, and J. Z. Bird, “Vibration Analysis of the First Stage of a Multi-stage Coaxial Magnetic Gearbox,” in *SoutheastCon 2018*, Apr. 2018, pp. 1–8, doi: 10.1109/SECON.2018.8478981.

[89] P. Elies and G. Lemarquand, “Analytical study of radial stability of permanent-magnet synchronous couplings,” *IEEE Trans. Magn.*, vol. 35, no. 4, pp. 2133–2136, Jul. 1999, doi: 10.1109/20.774183.

[90] T. H. Fay and L. Mead, “A magnet spring model,” *Int. J. Math. Educ. Sci. Technol.*, vol. 37, no. 3, pp. 321–329, Apr. 2006, doi: 10.1080/00207390500503103.

[91] R. G. Montague, C. M. Bingham, and K. Atallah, “Magnetic gear dynamics for servo control,” in *Melecon 2010 - 2010 15th IEEE Mediterranean Electrotechnical Conference*, Apr. 2010, pp. 1192–1197, doi: 10.1109/MELCON.2010.5475900.

[92] L. Xu and X. Zhu, “Natural Frequencies and Vibrating Modes for a Magnetic Planetary Gear Drive,” *Shock and Vibration*, 2012. https://www.hindawi.com/journals/sv/2012/614134/abs/ (accessed Apr. 23, 2019).

[93] X. Hao and X. Zhu, “Nonlinear forced vibration of electromechanical integrated magnetic gear system,” in *2015 IEEE International Conference on Mechatronics and Automation (ICMA)*, Aug. 2015, pp. 612–617, doi: 10.1109/ICMA.2015.7237555.

[94] M. Fukuoka, K. Nakamura, and O. Ichinokura, “Dynamic Analysis of Planetary-Type Magnetic Gear Based on Reluctance Network Analysis,” *IEEE Trans. Magn.*, vol. 47, no. 10, pp. 2414–2417, Oct. 2011, doi: 10.1109/TMAG.2011.2157100.

[95] J. Lee and J. Chang, “Analysis of the Vibration Characteristics of Coaxial Magnetic Gear,” *IEEE Trans. Magn.*, vol. 53, no. 6, pp. 1–4, Jun. 2017, doi: 10.1109/TMAG.2017.2665660.

[96] K. Li, S. Modaresahmadi, W. B. Williams, J. Z. Bird, J. D. Wright, and D. Barnett, “Electromagnetic Analysis and Experimental Testing of a Flux Focusing Wind Turbine Magnetic Gearbox,” *IEEE Trans. Energy Convers.*, vol. 34, no. 3, pp. 1512–1521, Sep. 2019, doi: 10.1109/TEC.2019.2911966.

[97] H. Baninajar, J. Z. Bird, S. Modaresahmadi, and W. Williams, “Electromagnetic and Mechanical Design of a Hermetically Sealed Magnetic Gear for a Marine Hydrokinetic Generator,” in *2018 IEEE Energy Conversion Congress and Exposition (ECCE)*, Sep. 2018, pp. 4987–4993, doi: 10.1109/ECCE.2018.8557386.

[98] M. B. Kouhshahi *et al.*, “An Axial Flux Focusing Magnetically Geared Generator for Low Input Speed Applications,” *IEEE Trans. Ind. Appl.*, vol. 56, no. 1, pp. 138–147, Jan. 2020, doi: 10.1109/TIA.2019.2946120.

[99] “Laser Cut Laminations for Motors and Generators.” http://www.polarislaserlaminations.com/laser-cut-laminations.html (accessed Feb. 10, 2020).

[100] “EML2322L-Tolerances.pdf.” Accessed: Feb. 10, 2020. [Online]. Available: https://mae.ufl.edu/designlab/Lab%20Assignments/EML2322L-Tolerances.pdf.

[101] K. Atallah, S. D. Calverley, and D. Howe, “Design, analysis and realisation of a high-performance magnetic gear,” *IEE Proc. - Electr. Power Appl.*, vol. 151, no. 2, pp. 135–143, Mar. 2004, doi: 10.1049/ip-epa:20040224.

[102] “Normal Stress, Bending Stress, & Shear Stress » StruCalc™.” http://www.strucalc.com/normal-stress-bending-stress-shear-stress/ (accessed Apr. 08, 2019).

[103] “Engr Help.” http://abe-research.illinois.edu/faculty/dickc/Engineering/shearflowa.htm (accessed Feb. 11, 2020).

[104] I. Press, *MACHINERY’S HANDBOOK FOR MACHINE SHOP AND DRAFTING-ROOM. FIFTH EDITION.*, 5th Edition edition. Industrial Press, 1917.

[105] B. Mevel and J. L. Guyader, “Routes To Chaos In Ball Bearings,” *J. Sound Vib.*, vol. 162, no. 3, pp. 471–487, Apr. 1993, doi: 10.1006/jsvi.1993.1134.

[106] S. M. Ahmadi, M. R. Ghazavi, and M. Sheikhzad, “Dynamic Analysis of a Rotor Supported on Ball Bearings with Waviness and Centralizing Springs and Squeeze Film Dampers,” *Int. J. Eng. - Trans. C Asp.*, vol. 28, no. 9, pp. 1351–1358, Sep. 2015.

[107] W. Thomson, *Theory of Vibration with Applications*. CRC Press, 2018.

[108] D. M. Mathiasen and N. T. Olesen, “Manufacturing, Modelling and Control of a High Speed Permanent Magnet Synchronous Machine including a Thermal Analysis - Project Library, Aalborg University,” Jun. 03, 2014. https://projekter.aau.dk/projekter/en/studentthesis/manufacturing-modelling-and-control-of-a-high-speed-permanent-magnet-synchronous-machine-including-a-thermal-analysis(d203bcf7-f5a9-4eac-a4a6-7b974d8ad11c).html (accessed Oct. 03, 2018).

[109] L. Popova, J. Nerg, and J. Pyrhonen, “Combined Electromagnetic and thermal design platform for totally enclosed induction machines,” in *8th IEEE Symposium on Diagnostics for Electrical Machines, Power Electronics & Drives*, Bologna, Italy, Sep. 2011, pp. 153–158, doi: 10.1109/DEMPED.2011.6063617.

[110] T. Zickler, “Dynamic Behavior of Laminated Magnets With Solid Tension Bars,” *IEEE Trans. Appl. Supercond.*, vol. 28, no. 3, pp. 1–6, Apr. 2018.

[111] J. Khalesi, S. Modaresahmadi, and G. Atefi, “SEM Gamma Prime Observation in a Thermal and Stress Analysis of a First-stage Rene’ 80H gas Turbine Blade: Numerical and Experimental Investigation,” *Iran. J. Sci. Technol. Trans. Mech. Eng.*, Jul. 2018, doi: 10.1007/s40997-018-0235-0.

[112] “Home - Neorem magnets.” http://www.neorem.fi/ (accessed Oct. 03, 2018).

[113] “Aluminium Alloy 6061 - Composition, Properties, Temper and Applications of 6061 Aluminium,” *AZoM.com*, Mar. 24, 2006. https://www.azom.com/article.aspx?ArticleID=3328 (accessed Oct. 03, 2018).

[114] S. W. Churchill and H. H. S. Chu, “Correlating equations for laminar and turbulent free convection from a vertical plate,” *Int. J. Heat Mass Transf.*, vol. 18, no. 11, pp. 1323–1329, Nov. 1975, doi: 10.1016/0017-9310(75)90243-4.

[115] S. Modaresahmadi, J. Khalesi, J. Kadel, and W. Williams, “Thermal Analysis of a Subscale Flux Focusing Magnetic Gearbox,” presented at the ASME 2018 International Mechanical Engineering Congress and Exposition, Nov. 2018, p. V08AT10A047-V08AT10A047, doi: 10.1115/IMECE2018-86876.

[116] J. (ORCID:0000000246484026) Bird and W. Williams, “Advanced High Torque Density Magnetically Geared Generator,” University of North Carolina at Charlotte, DOE-UNCC-06801, Jun. 2018. doi: 10.2172/1494152.

[117] K. Li, S. Modaresahmadi, W. Williams, and J. Z. Bird, “Electromagnetic analysis of a wind turbine magnetic gearbox,” *J. Eng.*, vol. 2019, no. 17, pp. 4101–4105, 2019, doi: 10.1049/joe.2018.8006.

[118] “Moist Metal Grip: Corrosion Resistant Waterproof Paint For Metal & Steel,” *Superior Coating Solutions*. https://superiorcoatingsolutions.com/moist-metal-grip-liquid-reinforcement-coating/ (accessed Apr. 25, 2019).

[119] M. Desvaux, B. Multon, H. Ben Ahmed, and S. Sire, “Supporting the Laminated Ferromagnetic Pole Pieces in a Magnetic Gear: A Structure Behaviour Analysis from a Multibody Model,” in *Multibody Mechatronic Systems*, 2018, pp. 85–94.

[120] N. Fernando and S. Saha, “Torsional Shear Stress Minimization Techniques and Implications on Electromagnetic Performance of Flux-Modulated Double Rotors,” *IEEE Trans. Energy Convers.*, vol. 33, no. 1, pp. 49–58, Mar. 2018, doi: 10.1109/TEC.2017.2727960.

[121] H. Shin and J. Chang, “Comparison of Radial Force at Modulating Pieces in Coaxial Magnetic Gear and Magnetic Geared Machine,” *IEEE Trans. Magn.*, vol. 54, no. 3, pp. 1–4, Mar. 2018, doi: 10.1109/TMAG.2017.2768552.

[122] A. S. McDonald, M. A. Mueller, and H. Polinder, “Structural mass in direct-drive permanent magnet electrical generators,” *IET Renew. Power Gener.*, vol. 2, no. 1, pp. 3–15, Mar. 2008.

[123] A. Zavvos, A. S. McDonald, and M. Mueller, “Structural optimisation tools for iron cored permanent magnet generators for large direct drive wind turbines,” pp. 35–35, Jan. 2011, doi: 10.1049/cp.2011.0231.

[124] N. Garg, N. D. Chakladar, B. G. Prusty, C. Song, and A. W. Phillips, “Modelling of laminated composite plates with weakly bonded interfaces using scaled boundary finite element method,” *Int. J. Mech. Sci.*, vol. 170, p. 105349, Mar. 2020, doi: 10.1016/j.ijmecsci.2019.105349.

[125] “Non-Oriented Electrical Steel | Products | Cogent Power.” https://cogent-power.com/products/non-oriented-electrical-steel (accessed Jan. 27, 2020).

[126] “ASM Material Data Sheet.” http://asm.matweb.com/search/SpecificMaterial.asp?bassnum=MA6061T6 (accessed Jan. 27, 2020).

[127] “Tool Steel Classifications,” *AZoM.com*, Jul. 06, 2012. https://www.azom.com/article.aspx?ArticleID=6138 (accessed Jan. 27, 2020).

[128] K. Li, K. K. Uppalapati, J. Wright, J. Kadel, J. Bird, and W. Willimas, “Investigating the Performance of a Fully Laminated Flux-Focusing Magnetic Gearbox,” *Prog. Electromagn. Res.*, vol. 87, pp. 51–62, 2018, doi: 10.2528/PIERC18062509.

[129] “Handbook of Computational Fluid Mechanics - Google Books.” https://books.google.com/books?hl=en&lr=&id=HjWlOe7FcBQC&oi=fnd&pg=PP2&dq=Peyret,+R.,+1996.+Handbook+of+Computational+Fluid+Mechanics.+Academic+Press+Limited,+USA&ots=MwGzHuU29b&sig=JsId3yUbw8HpeuRIRESROcmXwS4#v=onepage&q&f=false (accessed Sep. 09, 2019).

[130] S. Modaresahmadi, C. Nichols, and W. Williams, “Mechanical Design of Magnetic Gearboxes Optimized for Assembly,” presented at the ASME 2018 International Mechanical Engineering Congress and Exposition, Nov. 2018, p. V06AT08A012-V06AT08A012, doi: 10.1115/IMECE2018-86878.

[131] K. Li, “An Investigation into the Torque Capabilities of High Gear Ratio Magnetic Gearboxes,” Ph.D., The University of North Carolina at Charlotte, United States -- North Carolina, 2018.

[132] M. Jafari, H. Afshin, B. Farhanieh, and A. Sojoudi, “Numerical investigation of geometric parameter effects on the aerodynamic performance of a Bladeless fan,” *Alex. Eng. J.*, vol. 55, no. 1, pp. 223–233, Mar. 2016, doi: 10.1016/j.aej.2015.11.001.

[133] K. N. Srinivas and R. Arumugam, “Thermal characterization through finite element analysis of the switched reluctance motor,” in *Proceedings of IEEE Region 10 International Conference on Electrical and Electronic Technology. TENCON 2001 (Cat. No.01CH37239)*, Aug. 2001, vol. 2, pp. 819–823 vol.2, doi: 10.1109/TENCON.2001.949707.

[134] S. Modaresahmadi, J. Khalesi, K. Li, J. Z. Bird, and W. B. Williams, “Convective heat transfer analysis of a laminated flux focusing magnetic gearbox,” *Therm. Sci. Eng. Prog.*, vol. 18, p. 100552, Aug. 2020, doi: 10.1016/j.tsep.2020.100552.

[135] B. S. Yilbas, A. F. M. Arif, and B. J. Abdul Aleem, “Laser welding of low carbon steel and thermal stress analysis,” *Opt. Laser Technol.*, vol. 42, no. 5, pp. 760–768, Jul. 2010, doi: 10.1016/j.optlastec.2009.11.024.

[136] K. Li, K. K. Uppalapati, J. Wright, J. Kadel, J. Bird, and W. Willimas, “Investigating the Performance of a Fully Laminated Flux-Focusing Magnetic Gearbox,” *Prog. Electromagn. Res.*, vol. 87, pp. 51–62, 2018, doi: 10.2528/PIERC18062509.

[137] G. International, “6061 Aluminum Alloy - Properties,” p. 1.

[138] G. International, “7075 Aluminum Alloy - Properties,” p. 1.

[139] H. Baninajar, J. Z. Bird, S. Modaresahmadi, and W. Williams, “Electromagnetic Design and Assembly Analysis of a Halbach Rotor Magnetic Gear for a Marine Hydrokinetic Application,” in *2019 IEEE Energy Conversion Congress and Exposition (ECCE)*, Sep. 2019, pp. 732–739, doi: 10.1109/ECCE.2019.8911901.

[140] “Bonding.” http://www.polarislaserlaminations.com/bonding.html (accessed Jan. 27, 2020).

Appendix: